



This is a repository copy of *Advances in dual-three-phase permanent magnet synchronous machines and control techniques*.

White Rose Research Online URL for this paper:  
<https://eprints.whiterose.ac.uk/180427/>

Version: Published Version

---

**Article:**

Zhu, Z. [orcid.org/0000-0001-7175-3307](https://orcid.org/0000-0001-7175-3307), Wang, S., Shao, B. et al. (3 more authors) (2021) *Advances in dual-three-phase permanent magnet synchronous machines and control techniques*. *Energies*, 14 (22). 7508.

<https://doi.org/10.3390/en14227508>

---

**Reuse**

This article is distributed under the terms of the Creative Commons Attribution (CC BY) licence. This licence allows you to distribute, remix, tweak, and build upon the work, even commercially, as long as you credit the authors for the original work. More information and the full terms of the licence here:  
<https://creativecommons.org/licenses/>

**Takedown**



If you consider content in White Rose Research Online to be in breach of UK law, please notify us by emailing [eprints@whiterose.ac.uk](mailto:eprints@whiterose.ac.uk) including the URL of the record and the reason for the withdrawal request.



[eprints@whiterose.ac.uk](mailto:eprints@whiterose.ac.uk)  
<https://eprints.whiterose.ac.uk/>

Review

# Advances in Dual-Three-Phase Permanent Magnet Synchronous Machines and Control Techniques

Ziqiang Zhu <sup>\*</sup> , Shensheng Wang, Bo Shao, Luocheng Yan , Peilin Xu and Yuan Ren

Department of Electronic and Electrical Engineering, University of Sheffield, Mappin Street, Sheffield S1 3JD, UK; swang104@sheffield.ac.uk (S.W.); bshao1@sheffield.ac.uk (B.S.); lyan17@sheffield.ac.uk (L.Y.); xupeilinnuaa@gmail.com (P.X.); yuanren2020@gmail.com (Y.R.)

\* Correspondence: z.q.zhu@sheffield.ac.uk

**Abstract:** Multiphase electrical machines are advantageous for many industrial applications that require a high power rating, smooth torque, power/torque sharing capability, and fault-tolerant capability, compared with conventional single three-phase electrical machines. Consequently, a significant number of studies of multiphase machines has been published in recent years. This paper presents an overview of the recent advances in multiphase permanent magnet synchronous machines (PMSMs) and drive control techniques, with a focus on dual-three-phase PMSMs. It includes an extensive overview of the machine topologies, as well as their modelling methods, pulse-width-modulation techniques, field-oriented control, direct torque control, model predictive control, sensorless control, and fault-tolerant control, together with the newest control strategies for suppressing current harmonics and torque ripples, as well as carrier phase shift techniques, all with worked examples.

**Keywords:** direct torque control; dual-three-phase; fault-tolerant control; field oriented control; model predictive control; multiphase; multi-three-phase; permanent magnet; permanent magnet synchronous machines; pulse-width-modulation; sensorless control; synchronous machine



**Citation:** Zhu, Z.; Wang, S.; Shao, B.; Yan, L.; Xu, P.; Ren, Y. Advances in Dual-Three-Phase Permanent Magnet Synchronous Machines and Control Techniques. *Energies* **2021**, *14*, 7508. <https://doi.org/10.3390/en14227508>

Academic Editor: Yacine Amara

Received: 18 October 2021

Accepted: 5 November 2021

Published: 10 November 2021

**Publisher's Note:** MDPI stays neutral with regard to jurisdictional claims in published maps and institutional affiliations.



**Copyright:** © 2021 by the authors. Licensee MDPI, Basel, Switzerland. This article is an open access article distributed under the terms and conditions of the Creative Commons Attribution (CC BY) license (<https://creativecommons.org/licenses/by/4.0/>).

## 1. Introduction

Compared with conventional single-three-phase electrical machines, multiphase electrical machines are advantageous for many industrial applications that require high power rating, smooth torque, power/torque sharing capability, and fault-tolerant capability. In recent decades, there has been a significant and increasing number of published technical and review papers that discuss the topologies, modelling methods, control strategies, pulse-width-modulation (PWM) techniques, and applications of multiphase electrical machines [1–9].

Among these existing reviews, winding layouts, space harmonic cancellation, and equivalent circuits of multiphase induction machines (IMs) are discussed in [1]. The modelling and field-oriented control (vector control) of multi-three-phase (MTP) IMs are reviewed and compared with those of their single-three-phase counterparts in [2]. The PWM techniques and direct torque control (DTC) of dual-three-phase (DTP) IMs are studied in [3]. Additionally, the control strategies of five-phase and asymmetric six-phase IMs, and fault tolerant control strategies are reviewed in [4,5]. The use of multiphase machines in variable-speed applications and automotive traction applications are introduced in [6] and [9], respectively. The research in [7] presents multilevel inverters and corresponding PWM techniques as well as the exploitation of additional degrees of freedom. The review of model predictive control (MPC) in multiphase machine systems is covered in [8] and [9]. However, the existing reviews mainly focus on the development of multiphase IMs without a comprehensive coverage of multiphase permanent magnet (PM) machines. This paper presents an overview of multiphase PM synchronous machines (PMSMs) and drive control techniques.

The early application of multiphase machines was in the field of ship propulsion, which is still its main application area: five-phase PM machines [10,11], six-phase PM machines [12], and 15 phase machines [13] are successfully applied in ship propulsion. The increased emphasis on environmental protection has accelerated the development of greener modes of electrified transportation, and has led to the rise of renewable energy industries. The advantages of multiphase machines attract researchers to utilize them in electric and hybrid electric vehicles (EVs), e.g., on-board battery chargers for EVs with three-phase machines [14], five-phase machines [15], six-phase machines [16,17], and nine-phase machines [18]. Besides, they are also considered preferable solutions for wind power generation systems due to the power sharing capability [19], modularity [20], additional degrees of freedom [21], and fault-tolerant capability [22,23] provided by their multiphase topologies. Furthermore, electric aircraft have received much attention in the modern commercial and military aerospace industries [24–26], where multiphase machines have exhibited irreplaceable fault tolerance capability compared with conventional three-phase machines in recent years.

The multiphase machines mentioned above can be classified into two kinds, according to the number of phases: MTP (6- [27–32], 9- [33–35], 12- [36], 15- [13], ... phase) machines and other multiphase (4- [37], 5- [38,39], 7- [40,41], 11- [42], ... phase) machines. Since commercial three-phase inverters and many advanced control techniques can be utilized in MTP machines, MTP machines have become more popular in recent years. Considering the recent developments in PM materials, MTP PMSMs are currently especially attractive. The MTP PM machines not only exhibit the merits of multiphase machines but also retain the advantages of PMSMs, such as high torque density, high power density, and high efficiency. In terms of the machine drives, the winding sets can be fed by multiple generic and modular three-phase inverters, the DC links of which can be connected to the same or independent power sources. This means that the drive topologies do not need to be redesigned and the power can be freely exchanged among several isolated systems through multiphase windings.

Multiphase PMSMs are composed of several three-phase winding sets, with a specific displaced angle  $\beta$  between two adjacent sets, as shown in Figure 1.  $A_1$ ,  $B_1$ , and  $C_1$  represent the winding axes of the first three-phase set;  $A_2$ ,  $B_2$ , and  $C_2$  represent the winding axes of the second three-phase set;  $i_{A1}$ ,  $i_{B1}$ , and  $i_{C1}$  are the three-phase currents of the first set; and  $i_{A2}$ ,  $i_{B2}$ , and  $i_{C2}$  are the three-phase currents of the second set. The value  $V_{dc}$  represents the DC-link voltage. The displaced angle  $\beta$  can be flexibly designed according to the machine slot/pole number combinations to achieve different resultant electromagnetic performances. Generally, for DTP PMSMs, 0 and 30 degs. are the most common angle displacements between the two sets of three-phase windings [27,28]. The 0 deg. type features more freedom in winding layouts, while the 30 deg. type provides higher torque density, reduced stator magnetomotive force (MMF) harmonics, lower torque ripples under healthy conditions, and lower unbalanced magnetic force (UMF) under faulty conditions [27]. Compared with the most general three-phase machines, it is worth noting that the MTP machine system provides the advantages of reduced torque ripple, increased torque density, increased efficiency, fault-tolerant capability, reduction of DC-link capacitors, and more control freedom.

This paper attempts to provide an up-to-date review of MTP PMSM systems, with a focus on DTP PMSMs, as tabulated in Table 1. Several important topics are grouped and introduced with reference to the existing body of research. It should be noted that while the major topics of MTP PMSM systems in the existing review work are covered, this paper provides a comprehensive overview of machine topologies, modelling methods, PWM techniques, field oriented control, direct torque control, model predictive control, sensorless control, and fault-tolerant control, together with the newest control strategies for suppressing current harmonics and torque ripples, as well as carrier phase shift techniques. Worked examples, which were developed at the University of Sheffield, are presented in each section, whenever possible, to support the discussions.

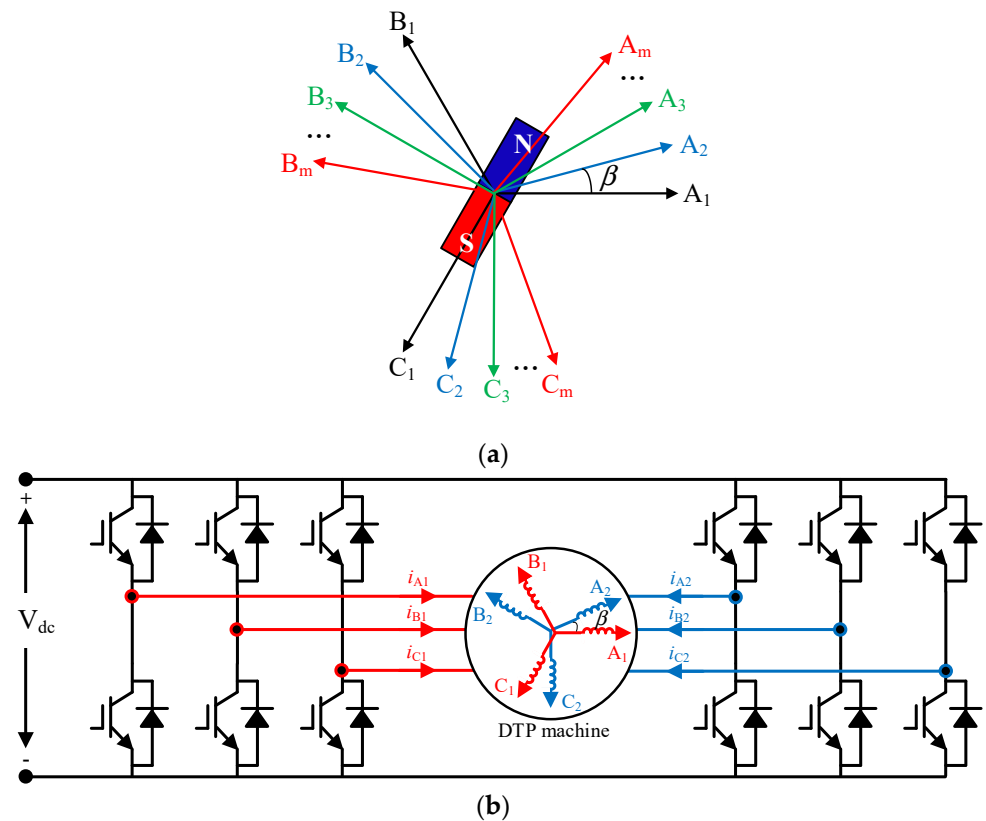


Figure 1. Winding axes of MTP PMSMs. (a) MTP; (b) DTP machine and inverters.

Table 1. Topics and relevant references.

Topics	References	Typical Papers
Design of multi-three-phase PM machine	[27–53]	Barcaro, et al., 2010, [27], University of Padova, Italy Abdel-Khalik, et al., 2015, [29], Alexandria University, Egypt Chen, et al., 2014, [33], University of Sheffield, UK Xu, et al., 2018, [46], University of Sheffield, UK Li, et al., 2020, [50], University of Sheffield, UK
Modelling of multi-three-phase PM machine	[54–67]	Karttunen, et al., 2012, [54], Lappeenranta University of Technology, Finland Hu, et al., 2017, [58], University of Sheffield, UK Zhao, et al., 1995, [62], University of Wisconsin-Madison, USA Zabaleta, et al., 2017, [63], Liverpool John Moores University, UK Che, et al., 2014, [73], Liverpool John Moores University, UK
Vector control	[54–58,68–84]	Karttunen, et al., 2017, [70], Lappeenranta University of Technology, Finland Yan, et al., 2021, [81], University of Sheffield, UK
Direct torque control	[85–100]	Bojoi, et al., 2005, [85], Power Electronics Innovation Center at Politecnico di Torino, Italy Ren, et al., 2015, [87], University of Sheffield, UK Shao, et al., 2021, [91], University of Sheffield, UK
Model predictive control	[101–117]	Barrero, et al., 2009, [101], University of Seville, Spain Duran, et al., 2011, [103], University of Malaga, Spain Luo, et al., 2019, [113], City University of Hong Kong, HK, China
PWM techniques	[118–141]	Marouani, et al., 2008, [129], Ecole Militaire Polytechnique, Algeria Suhel, et al., 2008, [130], Sarvajanic College of Engineering and Technology, India Yazdani, et al., 2009, [138], Fairchild Semiconductor, USA Zhou, et al., 2016, [139], Harbin Institute of Technology, China
Sensorless control	[142–161]	Almarhoon, et al., 2017, [159], University of Sheffield, UK Almarhoon, et al., 2017, [160], University of Sheffield, UK Liu, et al., 2021, [161], University of Sheffield, UK

Table 1. Cont.

Topics	References	Typical Papers
Fault tolerant control	[162–190]	Barcaro, et al., 2011, [162], University of Seville, Spain Cheng, et al., 2016, [170], Southeast University, China Wang, et al., 2003, [176], University of Sheffield, UK Hu, et al., 2021, [185], University of Sheffield, UK
Carrier phase-shift techniques	[191–201]	Miyama, et al., 2018, [193], Mitsubishi Electric Corporation, Japan Han, et al., 2019, [194], Huazhong University of Science and Technology, China Zhang, et al., 2020, [196], Harbin Institute of Technology, China

### 2. Various MTP and DTP PMSM Topologies

There are many machine topologies for MTP PMSMs. Various surface-mounted and interior PM rotor topologies can be employed [53] and will not be described here, since for MTP PMSMs, the major difference is in the stator winding configurations, which are associated with slot/pole number combinations. In this section, the focus will be on DTP PMSMs according to:

- Slot/pole number combinations;
- Angle displacement between two sets of three-phase windings;
- Coil pitch of windings.

Since there are two sets of three-phase windings in DTP PMSMs, the slot number should be a multiple of six to install the windings. For DTP PMSMs with slot number  $N_s$  ( $N_s = 6k$ ,  $k$  is an integer number) and pole number  $2p$  ( $p$  is the number of pole pairs), various angle displacements between two sets of three-phase windings and coil pitches can be chosen, according to the coil electromotive force (EMF) phasor diagram.

It should be noted that the angle displacements are analyzed based on the unit machine of each machine (the greatest common divisor ( $N_s, 2p$ ) = 1). For a unit machine, the feasible angle displacements can be  $0^\circ$  or  $360^\circ / N_s$  ( $60^\circ / k$ ), where  $k$  is an integer. Besides  $0^\circ$  and  $60^\circ / k$ , if  $k$  is even,  $30^\circ$  is another feasible angle displacement. Thus, the feasible angle displacements in DTP PMSMs considering different slot/pole number combinations are shown in Table 2. For example, the feasible angle displacements in a 24-slot/20-pole PMSM are  $0^\circ$  and  $30^\circ$ , the same as those in a 12-slot/10-pole PMSM. In Table 2, the cells of the machines that share the same unit machine are marked with the same background color, and the relationship between the background colors and the corresponding unit machines are also shown beneath Table 2.

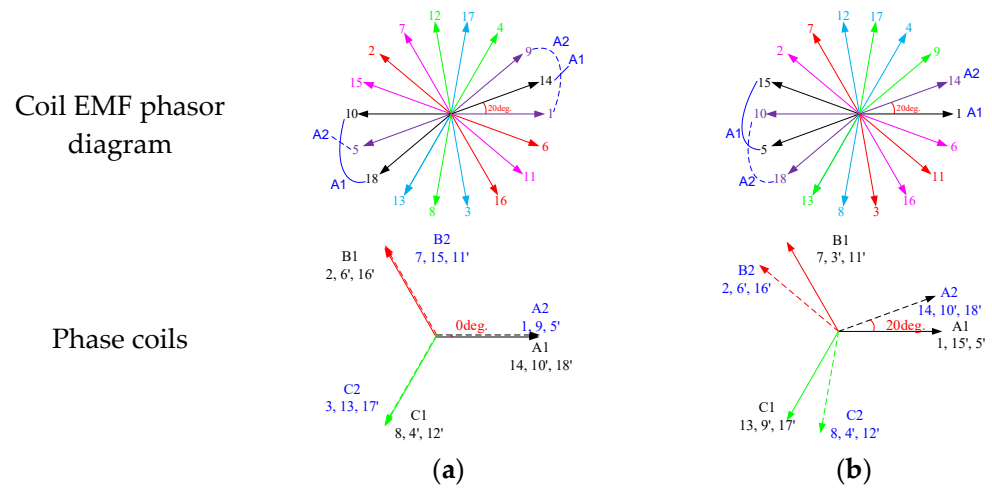
Table 2. Feasible angle displacements ( $\beta$ ) of DTP PMSMs with different slot/pole number combinations.

$N_s$	$2p$		2	4	6	8	10	12	14	16	18	20	22	24	26	28	30	
6	0	0	**	0	0	**	0	0	**	0	0	**	0	0	**	0	0	**
12	0/30	0	**	0	0/30	**	0/30	0	**	0/30	0	**	0/30	0/30	**	0/30	0	**
18	0/20	0/20	0	0/20	0/20	0	0/20	0/20	**	0/20	0/20	**	0/20	0/20	0	0/20	0/20	0
24	0/15	0/30	**	0	0/15/30	**	0/15	0	**	0/30	0/15/30	**	0/15	0/30	**	0/15	0/30	**
30	0/12	0/12	**	0/12	0	**	0/12	0/12	**	0	0/12	**	0/12	**	0/12	0/12	**	**
36	0/10	0/20	0/30	0/20	0/10/30	0	0/10	0/20	**	0/20	0/10/30	**	0/10/30	0	0/10	0/20	0/30	
Note	6-slot/2-pole		6-slot/4-pole		6-slot/8-pole		6-slot/10-pole		6-slot/14-pole		12-slot/10-pole		12-slot/14-pole					
	12-slot/2-pole		18-slot/2-pole		18-slot/4-pole		18-slot/8-pole		18-slot/10-pole		18-slot/14-pole							

\* Unfeasible slot/pole combinations for DTP PMSMs.

It is well known that a winding factor ( $K_w$ ) is the product of the distribution factor ( $K_d$ ) and pitch factor ( $K_p$ ). For all DTP PMSMs, the winding factor is computed based on its unit machine. For a unit DTP PMSM, the distribution factor is determined by its slot/pole number combination and angle displacement, and the coil pitch factor can be calculated by its slot/pole number combination and coil pitch number.

With a specific slot/pole number combination and angle displacement, the distribution factor in DTP PMSMs can be obtained. Since the symmetrical characteristics of the coil EMF phasor diagrams are different when  $k$  is odd or even, the calculation of distribution factors should take “ $k$  is odd” and “ $k$  is even” into consideration, respectively. When  $k$  is odd, take an 18-slot/14-pole PMSM as an example, the coil EMF phasor diagrams with  $0^\circ$  and  $20^\circ$  angle displacements are shown in Figure 2a,b, respectively.

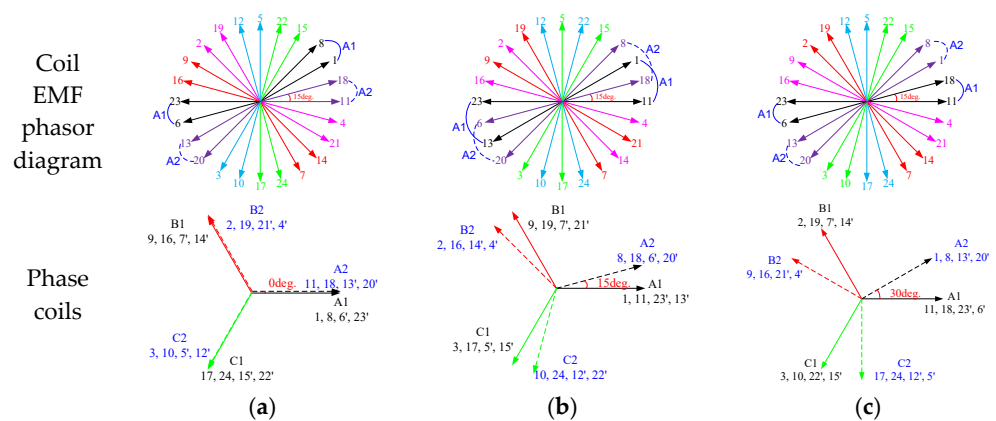


**Figure 2.** EMF phasor diagrams of 18 slot/14 pole DTP PMSMs with different angle displacements. Numerical number represents the number of coil. (a)  $\beta = 0^\circ$ ; (b)  $\beta = 20^\circ$ .

It can be seen in Figure 2 that the relative layouts of the EMF phasors used in one three-phase winding set are identical for these two angle displacements. Thus, the distribution factors of the 18 slot/14 pole PMSM with  $0^\circ$  and  $20^\circ$  angle displacements are both 0.945, according to the coil EMF phasor diagram. Similarly, it can be further deduced that when  $k$  is odd, the angle displacement between two sets of three-phase windings does not affect the distribution factor. Furthermore, if  $k$  is odd, the distribution factor can be calculated as

$$K_d = \frac{\sin\left(\frac{\pi}{6}\right)}{k \sin\left(\frac{\pi}{6k}\right)} = \frac{\sin\left(\frac{\pi}{6}\right)}{\frac{N_s}{6} \sin\left(\frac{\pi}{N_s}\right)}, k \text{ is odd.} \quad (1)$$

When  $k$  is even, the angle displacement can be  $0^\circ$ ,  $60^\circ/k$  and  $30^\circ$ . For example, in a 24 slot/14 pole PMSM,  $0^\circ$ ,  $15^\circ$ , and  $30^\circ$  displacements are feasible. The EMF phasor diagrams of the machine with these angle displacements are shown in Figure 3.



**Figure 3.** EMF phasor diagrams of 24 slot/14 pole DTP PMSMs with different angle displacements. (a)  $\beta = 0^\circ$ ; (b)  $\beta = 15^\circ$ ; (c)  $\beta = 30^\circ$ .

Comparing the coil EMF phasor diagrams in Figures 2 and 3, it can be observed that the layouts of the coil EMF phasors utilized in one winding set in a 24 slot/14 pole DTP PMSM are very different with different angle displacements. According to Figure 3, the distribution factors of the machine with  $0^\circ$ ,  $15^\circ$ , and  $30^\circ$  angle displacements can be computed as 0.958, 0.966, and 0.991, respectively. Based on the analyses above, it could be inferred that for the  $N_s$ -slot ( $N_s = 6k$ ,  $k$  is even) DTP PMSMs with  $\beta = 0^\circ$ ,  $\beta = 60^\circ/k$  and  $\beta = 30^\circ$ , the numbers of EMF phasors used in the distribution factor calculation are  $k$ ,  $k/2$ , and  $k/2$ , respectively, and the angles between the phasors are  $60^\circ/k$ ,  $120^\circ/k$ , and  $60^\circ/k$ , respectively. Overall, the distribution factor calculation in this condition can be summarized as

$$K_d = \begin{cases} \frac{\sin(\frac{\pi}{6})}{k \sin(\frac{\pi}{6k})} = \frac{6 \sin(\frac{\pi}{6})}{N_s \sin(\frac{\pi}{N_s})}, \beta = 0^\circ \\ \frac{\sin(\frac{\pi}{6})}{\frac{k}{2} \sin(\frac{\pi}{3k})} = \frac{12 \sin(\frac{\pi}{6})}{N_s \sin(\frac{2\pi}{N_s})}, \beta = \frac{60^\circ}{k}, k \text{ is even.} \\ \frac{\sin(\frac{\pi}{12})}{\frac{k}{2} \sin(\frac{\pi}{6k})} = \frac{12 \sin(\frac{\pi}{12})}{N_s \sin(\frac{\pi}{N_s})}, \beta = 30^\circ \end{cases} \quad (2)$$

From Equation (2), it can be deduced that for the 24 slot/14 pole DTP PMSM, when  $k$  is even,  $K_d(\beta = 0^\circ) = \cos(\pi/6k) \times K_d(\beta = 60^\circ/k) = \cos(\pi/12) \times K_d(\beta = 30^\circ)$ . Thus,  $K_d(\beta = 30^\circ)$  is higher than  $K_d(\beta = 0^\circ)$  by about 3.53%. In DTP PMSMs with a  $30^\circ$  angle displacement, the superiority in distribution factors over the counterparts with  $0^\circ$  angle displacement contributes to higher fundamental EMF and larger output torque. In accordance with Equations (1) and (2), the distribution factors of DTP PMSMs with different slot/pole number combinations considering different angle displacements are provided in Table 3.

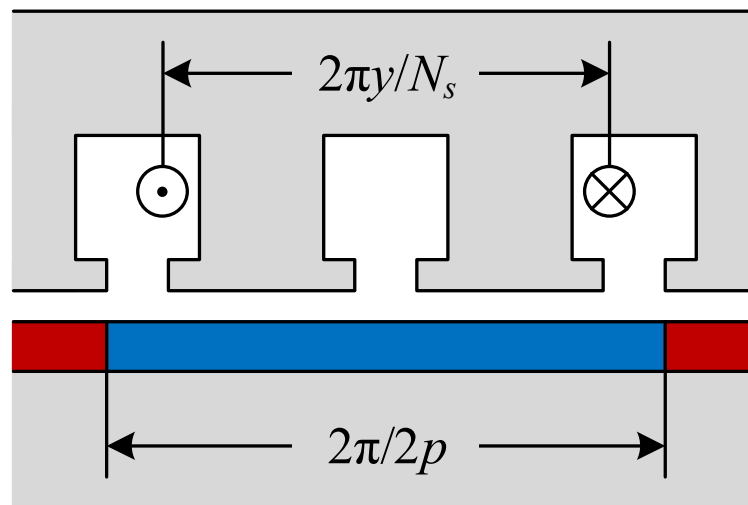
**Table 3.** Distribution factors ( $K_d$ ) of DTP PMSMs with different slot numbers considering different angle displacements.

$N_s$	Angle Displacement, $\beta$ ( $^\circ$ )	Distribution Factor, $K_d$
6	0	1
12	0	0.966
	30	1
18	0/20	0.960
	0	0.958
24	15	0.968
	30	0.991
	0/12	0.957
36	0	0.956
	10	0.960
	30	0.990

In DTP PMSMs, the calculation of the pitch factor is the same as that in single-three-phase PMSMs. It is well known that a pitch factor can be calculated by the angle difference between the pole-pitch and coil-pitch, which can be determined by the slot/pole number combination and the coil pitch number,  $y$ . The diagram of the pole-pitch and coil-pitch in PMSMs is shown in Figure 4. Accordingly, the pitch factor for the  $v$ -th harmonic is

$$K_{p-v} = \cos\left(v \frac{\frac{2\pi}{2p} - \frac{2\pi y}{N_s}}{2}\right) = \cos\left(v \frac{N_s - 2py}{2N_s p} \pi\right), \quad (3)$$

where  $y$  is the coil pitch in terms of the number of slot pitches.



**Figure 4.** Diagram of pole–pitch and coil–pitch in PMSMs.

Since the working harmonic is the  $p$ -th harmonic in  $N_s$ -slot/ $2p$ -pole DTP PMSMs, the pitch factor of the working harmonic is

$$K_p = \cos\left(p \frac{N_s - 2py}{2N_s p} \pi\right) = \cos\left(\frac{N_s - 2py}{2N_s} \pi\right). \tag{4}$$

With Equation (4), the pitch factors of DTP PM machines with different slot/pole number combinations considering coil pitch numbers varying from 1 to 4 are shown in Table 4. In Table 4, the high pitch factors ( $>0.866$ ) are marked with a pink background color. It should be mentioned that some values are 0 in Table 4, because the feasibility of DTP winding configurations are not considered in the calculation. It is necessary to double-check whether the slot/pole and coil pitch number combinations are feasible before utilizing them.

**Table 4.** Pitch factors ( $K_p$ ) of DTP PMSMs with different slot/pole number combinations and coil pitch number.

		$y = 1$														
$N_s$	$2p$	2	4	6	8	10	12	14	16	18	20	22	24	26	28	30
6		0.500	0.866	1.000	0.866	0.500	0.000	0.500	0.866	1.000	0.866	0.500	0.000	0.500	0.866	1.000
12		0.259	0.500	0.707	0.866	0.966	1.000	0.966	0.866	0.707	0.500	0.259	0.000	0.259	0.500	0.707
18		0.174	0.342	0.500	0.643	0.766	0.866	0.940	0.985	1.000	0.985	0.940	0.866	0.766	0.643	0.500
24		0.131	0.259	0.383	0.500	0.609	0.707	0.793	0.866	0.924	0.966	0.991	1.000	0.991	0.966	0.924
30		0.105	0.208	0.309	0.407	0.500	0.588	0.669	0.743	0.809	0.866	0.914	0.951	0.978	0.995	1.000
36		0.087	0.174	0.259	0.342	0.423	0.500	0.574	0.643	0.707	0.766	0.819	0.866	0.906	0.940	0.966
		$y = 2$														
$N_s$	$2p$	2	4	6	8	10	12	14	16	18	20	22	24	26	28	30
6		0.866	0.866	0.000	0.866	0.866	0.000	0.866	0.866	0.000	0.866	0.866	0.000	0.866	0.866	0.000
12		0.500	0.866	1.000	0.866	0.500	0.000	0.500	0.866	1.000	0.866	0.500	0.000	0.500	0.866	1.000
18		0.342	0.643	0.866	0.985	0.985	0.866	0.643	0.342	0.000	0.342	0.643	0.866	0.985	0.985	0.866
24		0.259	0.500	0.707	0.866	0.966	1.000	0.966	0.866	0.707	0.500	0.259	0.000	0.259	0.500	0.707
30		0.208	0.407	0.588	0.743	0.866	0.951	0.995	0.995	0.951	0.866	0.743	0.588	0.407	0.208	0.000
36		0.174	0.342	0.500	0.643	0.766	0.866	0.940	0.985	1.000	0.985	0.940	0.866	0.766	0.643	0.500



Table 4. Cont.

		y = 3														
$N_s$	2p	2	4	6	8	10	12	14	16	18	20	22	24	26	28	30
6		1.000	0.000	1.000	0.000	1.000	0.000	1.000	0.000	1.000	0.000	1.000	0.000	1.000	0.000	1.000
12		0.707	1.000	0.707	0.000	0.707	1.000	0.707	0.000	0.707	1.000	0.707	0.000	0.707	1.000	0.707
18		0.500	0.866	1.000	0.866	0.500	0.000	0.500	0.866	1.000	0.866	0.500	0.000	0.500	0.866	1.000
24		0.383	0.707	0.924	1.000	0.924	0.707	0.383	0.000	0.383	0.707	0.924	1.000	0.924	0.707	0.383
30		0.309	0.588	0.809	0.951	1.000	0.951	0.809	0.588	0.309	0.000	0.309	0.588	0.809	0.951	1.000
36		0.259	0.500	0.707	0.866	0.966	1.000	0.966	0.866	0.707	0.500	0.259	0.000	0.259	0.500	0.707

		y = 4														
$N_s$	2p	2	4	6	8	10	12	14	16	18	20	22	24	26	28	30
6		0.866	0.866	0.000	0.866	0.866	0.000	0.866	0.866	0.000	0.866	0.866	0.000	0.866	0.866	0.000
12		0.866	0.866	0.000	0.866	0.866	0.000	0.866	0.866	0.000	0.866	0.866	0.000	0.866	0.866	0.000
18		0.643	0.985	0.866	0.342	0.342	0.866	0.985	0.643	0.000	0.643	0.985	0.866	0.342	0.342	0.866
24		0.500	0.866	1.000	0.866	0.500	0.000	0.500	0.866	1.000	0.866	0.500	0.000	0.500	0.866	1.000
30		0.407	0.743	0.951	0.995	0.866	0.588	0.208	0.208	0.588	0.866	0.995	0.951	0.743	0.407	0.000
36		0.342	0.643	0.866	0.985	0.985	0.866	0.643	0.342	0.000	0.342	0.643	0.866	0.985	0.985	0.866


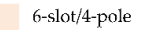
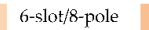
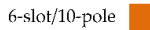
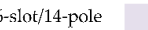
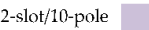
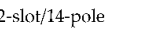
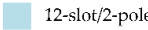
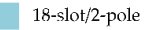
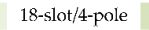
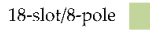
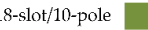
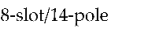
	1.	High pitch factors (>0.866)														
Note	2.	Pitch factor = 0 suggests unfeasible winding configuration.														
	3.	The feasibility of the specific slot/pole and pitch number combination is determined in Tables 2 and 4.														

In addition to the calculated results shown in Table 4, the pitch factors in some slot/pole number combinations can be further improved with other coil pitch numbers. For example, in a 12 slot/2 pole PMSM, the pitch factor is 1 with  $y = 6$ . Overall, the pitch factors ( $K_p$ ) of DTP PM machines with different slot/pole number combinations and optimized coil pitch numbers are summarized in Table 5.

Table 5. Pitch factors ( $K_p$ ) of DTP PMSMs with different slot/pole number combinations and optimized coil pitch numbers.

$N_s$	2p	2	4	6	8	10	12	14	16	18	20	22	24	26	28	30
6		1.000	0.866	**	0.866	1.000	**	1.000	0.866	**	0.866	1.000	**	1.000	0.866	**
12		1.000	1.000	**	0.866	0.966	**	0.966	0.866	**	1.000	0.866	**	0.866	1.000	**
18		1.000	0.985	1.000	0.985	0.985	0.866	0.985	0.985	**	0.985	0.985	0.866	0.985	0.985	1.000
24		1.000	1.000	**	1.000	0.966	**	0.966	0.866	**	0.966	0.991	**	0.991	0.966	**
30		1.000	0.995	**	0.995	1.000	**	0.995	0.995	**	0.866	0.995	**	0.978	0.995	**
36		1.000	1.000	1.000	0.985	0.985	1.000	0.966	0.985	**	0.985	0.940	0.866	0.985	0.985	0.966

Note		6-slot/2-pole		6-slot/4-pole		6-slot/8-pole		6-slot/10-pole		6-slot/14-pole		12-slot/10-pole		12-slot/14-pole
		12-slot/2-pole		18-slot/2-pole		18-slot/4-pole		18-slot/8-pole		18-slot/10-pole		18-slot/14-pole		

\*\* Unfeasible slot/pole combinations for DTP PMSMs.

To achieve the pitch factors in Table 5, the corresponding coil pitch numbers are shown in Table 6.

**Table 6.** Optimized coil pitch number of DTP PMSMs with different slot/pole number combinations.

$N_s$	$2p$	2	4	6	8	10	12	14	16	18	20	22	24	26	28	30
6		3	1	**	1	3	**	3	1	**	1	3	**	3	1	**
12		6	3	**	1	1	**	1	1	**	3	4	**	4	3	**
18		9	4	3	2	2	1	4	1	**	1	4	1	2	2	3
24		12	6	**	3	2	**	2	1	**	1	1	**	1	1	**
30		15	7	**	4	3	**	2	2	**	1	4	**	8	1	**
36		18	9	6	4	4	3	3	2	**	2	2	1	4	4	1
Note			1		2		3		4		6		9			

\*\* Unfeasible slot/pole combinations for DTP PMSMs.

In Table 6, the cells using the same coil pitch number are marked with the same background color. However, it should be noted that the coil pitch numbers shown in Table 6 were chosen to enhance the pitch factor only. In practice, it is preferable to use a lower coil pitch number, especially 1, because a lower coil pitch number means a shorter end-winding length. When  $y = 1$ , the tooth coil concentrated windings can be utilized to significantly ease fabrication. Hence, it is necessary to consider coil pitch number thoughtfully in the design of DTP PMSMs. According to the distribution factors and pitch factors calculated above, the winding factors of DTP PMSM with different slot/pole number combinations and different angle displacements are summarized in Table 7.

**Table 7.** Winding factors ( $K_w$ ) of DTP PMSMs with different slot/pole number combinations and different angle displacements.

$N_s$	$2p$	$\beta$ (°)	2	4	6	8	10	12	14	16	18	20	22	24	26	28	30
6		0	1.000	0.866	**	0.866	1.000	**	1.000	0.866	**	0.866	1.000	**	1.000	0.866	**
12		0	0.966	++	**	++	0.933	**	0.933	++	**	++	0.837	**	0.837	++	**
		30	1.000	++	**	++	0.966	**	0.966	++	**	++	0.866	**	0.866	++	**
18		0/20	0.960	0.945		0.945	0.945	++	0.945	0.945	**	0.945	0.945	++	0.945	0.945	++
24		0	0.958	++	**	++	0.925	**	0.925	++	**	++	0.949	**	0.949	++	**
		15	0.966	++	**	++	0.933	**	0.933	++	**	++	0.958	**	0.958	++	**
		30	0.991	++	**	++	0.958	**	0.958	++	**	++	0.983	**	0.983	++	**
30		0/12	0.957	0.951	**	0.951	+	**	0.951	0.951	**	++	0.951	**	0.951	0.951	**
36		0	0.956	++	++	++	0.942	++	0.924	++	**	++	0.898	++	0.867	++	++
		10	0.960	++	++	++	0.945	++	0.927	++	**	++	0.902	++	0.870	++	++
		30	0.990	++	++	++	0.975	++	0.956	++	**	++	0.930	++	0.897	++	++
Note			6-slot/2-pole 12-slot/2-pole	6-slot/4-pole 18-slot/2-pole	6-slot/8-pole 18-slot/4-pole	6-slot/10-pole 18-slot/8-pole	6-slot/14-pole 18-slot/10-pole	12-slot/10-pole 12-slot/14-pole									

\*\* Unfeasible slot/pole combinations for DTP PMSMs. ++Refer to its unit machine.

Compared with [46] where the winding factors only take a  $0^\circ$  angle displacement into consideration, the winding factors shown considered various possible angle displacements. Moreover, the pitch factors can be further improved with the optimized coil pitch numbers (as shown in Tables 4 and 5) in some slot/pole number combinations. Thus, the winding factors can also be increased in these slot/pole number combinations. For instance, the winding factor for a 36 slot/10 pole DTP PMSM with a  $0^\circ$  angle displacement is 0.924 ( $y = 3$ ), while it can be improved to 0.942 with  $y = 4$ .

Based on the analyses above, the topologies of the DTP PMSMs proposed and/or analyzed in existing research are summarized in Table 8. The angle displacements and coil pitch numbers in these machines are also provided in Table 8. The blank cells in Table 8 suggest more feasible topologies in this area.

**Table 8.** Various DTP PMSM topologies in existing research.

$N_s$	$2p$	2	4	6	8	10	12	14	16	18	20	22	24	26	28	30
6				**			**			**			**			**
12			**			$\beta = 0^\circ/30^\circ$ , $y = 1$ , [27] $\beta = 0^\circ/30^\circ$ , $y = 1$ , [29]	**			**			**			**
18				$\beta = 0^\circ/20^\circ$ , $y = 2$ , [31]				$\beta = 0^\circ/20^\circ$ , $y = 1$ , [33]		**						
24		**			$\beta = 0^\circ/30^\circ$ , $y = 2$ , [30] $\beta = 0^\circ/15^\circ/30^\circ$ , $y = 2$ , [46]	**		$\beta = 0^\circ/30^\circ$ , $y = 2$ , [43] $\beta = 30^\circ$ , $y = 1$ , [45]		**		$\beta = 0^\circ/15^\circ/30^\circ$ , $y = 1$ , [47]	**			**
30			**				**			**			**			**
36										**						
Note		6-slot/2-pole	6-slot/4-pole	6-slot/8-pole	6-slot/10-pole	6-slot/14-pole	12-slot/10-pole	12-slot/14-pole	18-slot/2-pole	18-slot/4-pole	18-slot/8-pole	18-slot/10-pole	18-slot/14-pole			

\*\* Unfeasible slot/pole combinations for DTP PMSMs.

### 3. Modelling of MTP PMSMs

The modelling of MTP PMSMs can be divided into two categories: multiple individual three-phase models [54–61] and vector space decomposition (VSD) models [62–67]. The former considers the machine as multiple single-three-phase submachines, and the model is straightforwardly derived from the synchronous *dq*-axis model of the three-phase machine. The VSD model uses a mathematical transformation to separate the variables of different orders into multiple orthogonal subspaces. In this context, it is convenient to formulate the machine model by using a set of decoupled subspaces. The advantages and disadvantages of the two modelling approaches are summarized in Table 9.

**Table 9.** Modelling of MTP PMSMs.

Modelling Methods	Multiple Individual Three-Phase	VSD
Advantages	<ol style="list-style-type: none"> <li>1. Straightforward.</li> <li>2. Modular modeling and control of each three-phase set.</li> </ol>	<ol style="list-style-type: none"> <li>1. Decoupled and simpler models in several subspaces.</li> <li>2. Simpler controller design.</li> <li>3. Easier to regulate the harmonics in control strategy.</li> </ol>
Disadvantages	<ol style="list-style-type: none"> <li>1. Additional coupling among sets.</li> <li>2. Complexity of model and control increases as number of sets increases.</li> </ol>	<ol style="list-style-type: none"> <li>1. Less capable of dealing with the unbalance issues due to asymmetry among the sets.</li> <li>2. More complex to achieve active power/torque sharing.</li> </ol>

#### 3.1. Multiple Individual Three-Phase PMSM Model

Multiphase PMSMs are composed of multiple individual three-phase sets, and thus the model of MTP PMSMs can be considered as the sum of the models of all three-phase machines with extra coupling voltage terms. For each three-phase set, the machine model in a synchronous *dq* frame is conducted. In particular, the two individual three-phase model of a DTP PMSM is shown in Figure 5.

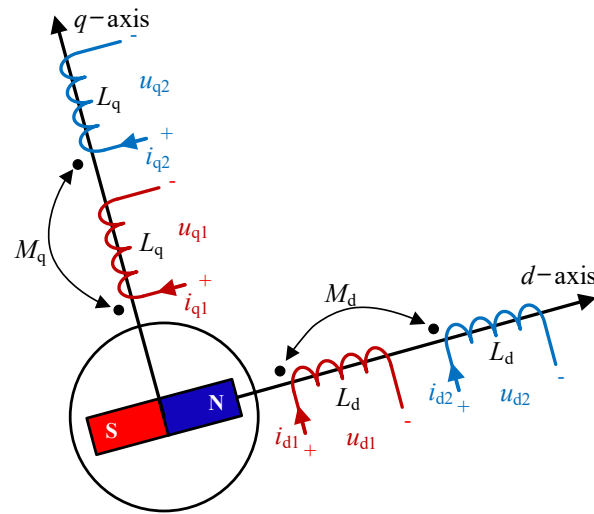


Figure 5. Two individual three-phase models of DTP PMSMs in dq-axis frame.

The corresponding voltage equations are as follows [58]:

$$\begin{bmatrix} u_{d1} \\ u_{q1} \end{bmatrix} = \begin{bmatrix} R_s + L_d s & -\omega_e L_q \\ \omega_e L_d & R_s + L_q s \end{bmatrix} \begin{bmatrix} i_{d1} \\ i_{q1} \end{bmatrix} + \begin{bmatrix} M_d s & -\omega_e M_q \\ \omega_e M_d & M_q s \end{bmatrix} \begin{bmatrix} i_{d2} \\ i_{q2} \end{bmatrix} + \begin{bmatrix} 0 \\ \omega_e \psi_{fd} \end{bmatrix} \quad (5)$$

$$\begin{bmatrix} u_{d2} \\ u_{q2} \end{bmatrix} = \begin{bmatrix} R_s + L_d s & -\omega_e L_q \\ \omega_e L_d & R_s + L_q s \end{bmatrix} \begin{bmatrix} i_{d2} \\ i_{q2} \end{bmatrix} + \begin{bmatrix} M_d s & -\omega_e M_q \\ \omega_e M_d & M_q s \end{bmatrix} \begin{bmatrix} i_{d1} \\ i_{q1} \end{bmatrix} + \begin{bmatrix} 0 \\ \omega_e \psi_{fd} \end{bmatrix} \quad (6)$$

where  $R_s$  is the stator resistance,  $\omega_e$  is the electrical angular speed, and  $\psi_{fd}$  is the PM flux linkage;  $s$  represents the derivative;  $u_{d1}$ ,  $u_{q1}$ ,  $i_{d1}$ , and  $i_{q1}$  represent the dq-axis voltages and currents of the first winding set, and  $u_{d2}$ ,  $u_{q2}$ ,  $i_{d2}$ , and  $i_{q2}$  represent the voltages and currents of the second winding set. The values  $L_d$  and  $L_q$  are the dq-axis inductances. The values  $M_d$  and  $M_q$  are the dq-axis mutual inductances, which denote the magnetized coupling between the two winding sets. The electromagnetic torque in the multiple individual three-phase model can be expressed as

$$T_e = \frac{3}{2} p \left[ \psi_{fd} (i_{q1} + i_{q2}) + (L_d - L_q) (i_{d1} i_{q1} + i_{d2} i_{q2}) + (M_d - M_q) (i_{d1} i_{q2} + i_{d2} i_{q1}) \right] \quad (7)$$

and the inductances are:

$$\begin{aligned} L_d &= M_d + L_\sigma \\ L_q &= M_q + L_\sigma \end{aligned} \quad (8)$$

where  $L_\sigma$  is the leakage inductance.

### 3.2. VSD Machine Model

The vector space decomposition (VSD) approach [62] is prevailing in the modeling of multiphase machines because the complex high-order electromagnetic system can be clearly simplified as two-order subsystems in many decomposed subspaces, which makes it easy to achieve independent current regulation in these decoupled subspaces. The VSD transformation for the DTP machine is given by:

$$\begin{bmatrix} F_\alpha \\ F_\beta \\ F_{z_1} \\ F_{z_2} \end{bmatrix} = \frac{1}{3} \begin{bmatrix} 1 & -1/2 & -1/2 & \sqrt{3}/2 & -\sqrt{3}/2 & 0 \\ 0 & -\sqrt{3}/2 & \sqrt{3}/2 & 1/2 & 1/2 & -1 \\ 1 & -1/2 & -1/2 & -1 & 1/2 & 1/2 \\ 0 & -\sqrt{3}/2 & \sqrt{3}/2 & 0 & \sqrt{3}/2 & -\sqrt{3}/2 \end{bmatrix} \begin{bmatrix} F_{A1} \\ F_{B1} \\ F_{C1} \\ F_{A2} \\ F_{B2} \\ F_{C2} \end{bmatrix} \quad (9)$$

where  $F$  can be the voltage, current, or flux linkage. The voltage and current can be decomposed into the  $\alpha\beta$  and  $z_1 z_2$  subspaces by using (9). The fundamental component and the harmonics with order of  $m = 12n \pm 1$  ( $n = 1, 2, 3, \dots$ ), i.e.,  $m = 11, 13, 23, 25$ , etc., are mapped in the  $\alpha\beta$  subspace and the  $m$ th values are mapped in the  $z_1 z_2$  subspace, where  $m = 6n \pm 1$  ( $n = 1, 3, 5, \dots$ ), i.e.,  $m = 5, 7, 17, 19$ , etc.

(see Figures 6 and 7). After the VSD transformation, the DTP PMSM can be described by the following models:

$$u_{\alpha\beta} = R_s i_{\alpha\beta} + s\psi_{\alpha\beta} \tag{10}$$

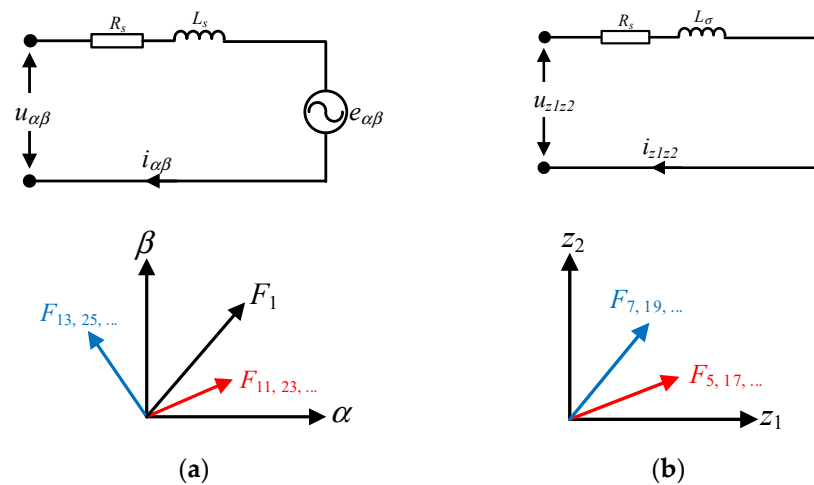
$$\psi_{\alpha\beta} = L_{s\alpha\beta} i_{\alpha\beta} + \psi_f e^{j\theta_e} \tag{11}$$

$$u_{z_1 z_2} = R_s i_{z_1 z_2} + s\psi_{z_1 z_2} \tag{12}$$

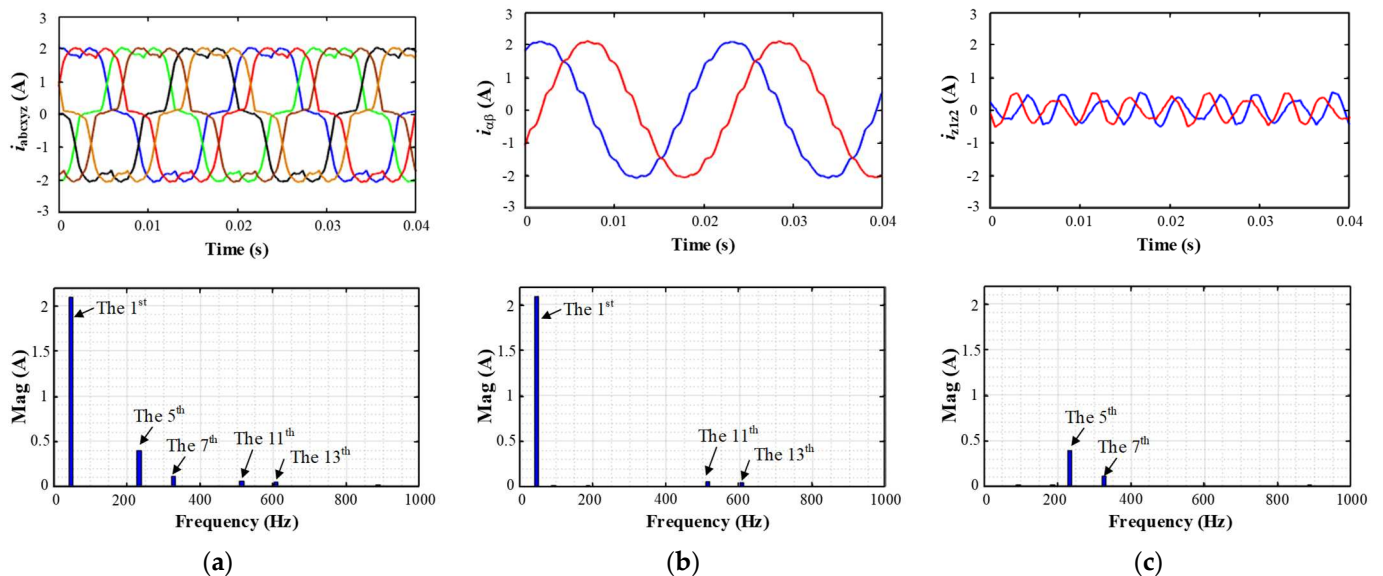
$$\psi_{z_1 z_2} = L_{\sigma} i_{z_1 z_2} \tag{13}$$

$$T_e = 3P(\psi_{\alpha} i_{\beta} - \psi_{\beta} i_{\alpha}) \tag{14}$$

where  $u$ ,  $i$ , and  $\psi$  are the voltage, current, and flux linkage. The value  $\psi_f$  is the PM flux linkage. The value  $\theta_e$  is the electrical rotor angle.



**Figure 6.** Equivalent circuits and definition of axes in VSD model of DTP PMSM. (a)  $\alpha\beta$  subspace. (b)  $z_1 z_2$  subspace.

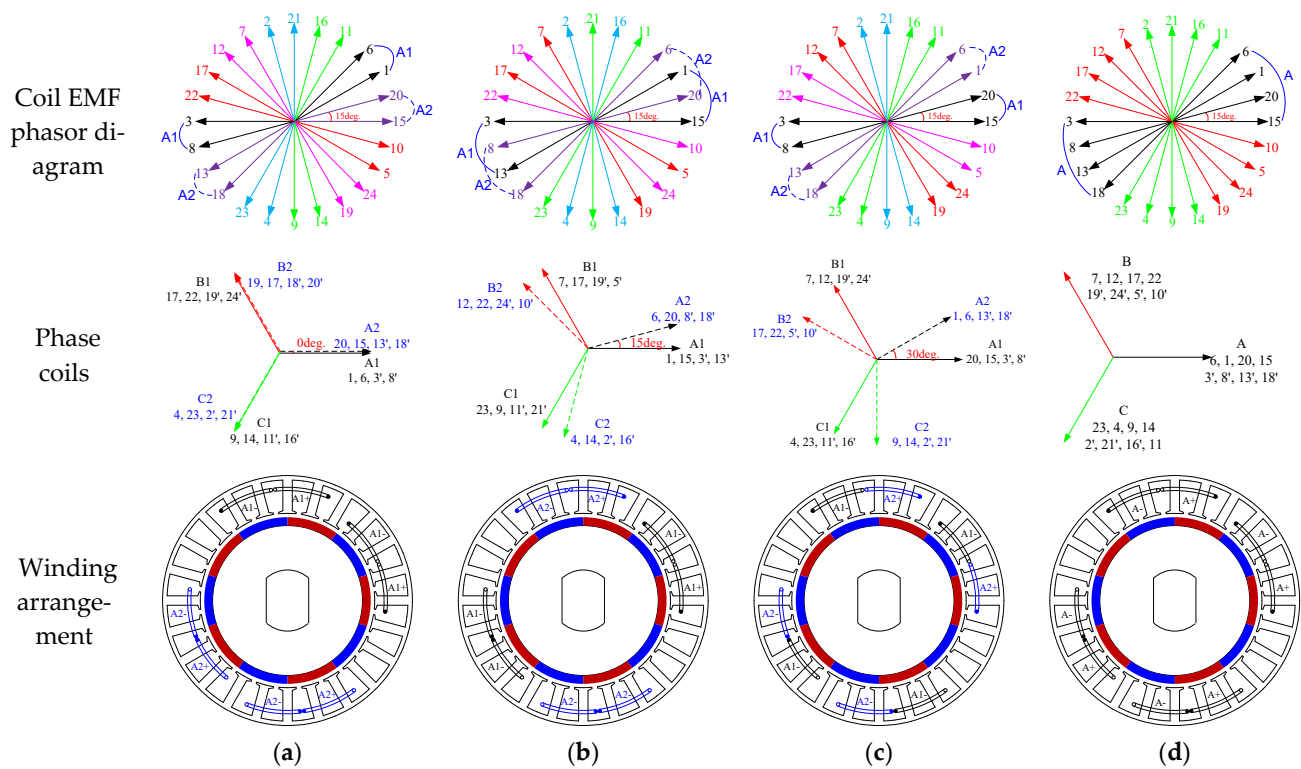


**Figure 7.** Currents and spectra of a typical DTP PMSM (24-slot/10-pole). Top: phase currents; bottom: spectra. (a) Phases, (b)  $\alpha\beta$  subspace, (c)  $z_1 z_2$  subspace.

Figure 6 shows the equivalent circuits in two subspaces and the definition of the axes. The value  $e_{\alpha\beta}$  represents the back-EMF mapped in the  $\alpha\beta$  subspace. It should be noted that the energy conversion occurs in the  $\alpha\beta$  subspace, and the electromagnetic torque is only relevant to the variables in this subspace. Unlike those in the single three-phase machine, the current harmonics mapped in  $z_1z_2$  subspace are limited by the resistance and leakage inductance, which are usually small. This causes serious current harmonics in this subspace, as the 5th and 7th values shown in Figure 7.

#### 4. Electromagnetic Performance Analysis under Healthy and Open-Circuit Conditions

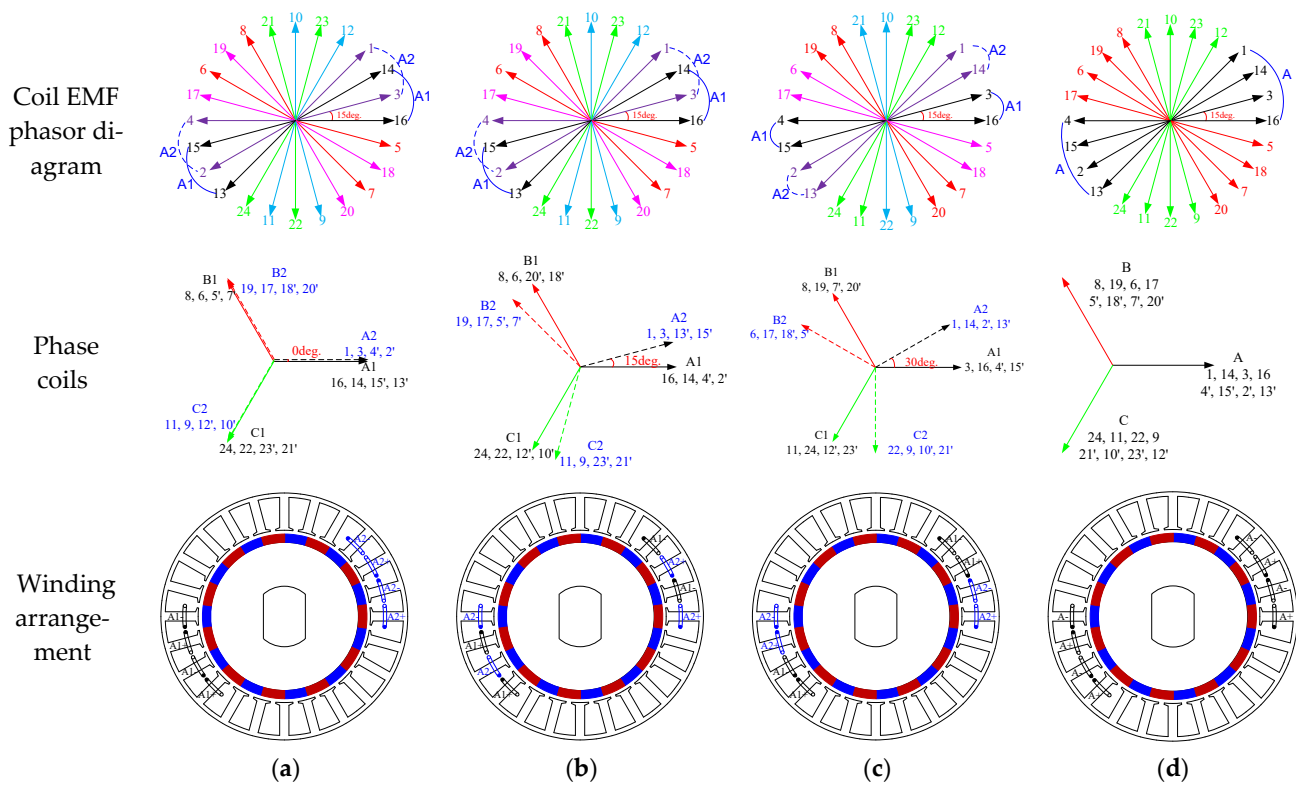
According to the analyses presented above, a 24 slot/10 pole PMSM and a 24 slot/22 pole PMSM can be equipped with DTP windings with  $0^\circ$ ,  $15^\circ$ , and  $30^\circ$  angle displacements, respectively [46,47]. The coil EMF phasors and the winding arrangements of the two machines with different winding configurations are shown in Figures 8 and 9. It should be mentioned that the coil pitch numbers in the two machines are 2 and 1 in order to obtain high winding factors, respectively. The winding connections of Phase A in the machines with different configurations are summarized in Table 10.



**Figure 8.** Two slot-pitch winding arrangements and EMF phasor diagrams for 24 slot/10 pole DTP PMSMs with different angle displacements [46]. (a) DTP,  $\beta = 0^\circ$ ; (b) DTP,  $\beta = 15^\circ$ ; (c) DTP,  $\beta = 30^\circ$ ; (d) single three-phase.

**Table 10.** Phase A coil connections in DTP PMSMs.

Machines	Angle Displacement, $\beta$	Coil Connection (A1)	Coil Connection (A2)
24 slot/10 pole 2 slot-pitch coils	$0^\circ$	1-3'-6-8'	13'-15-18'-20
	$15^\circ$	1-3'-13'-15	6-8'-18'-20
	$30^\circ$	3'-8'-15-20	1-6-13'-18'
24 slot/22 pole 1 slot-pitch coil	$0^\circ$	14-16-13'-15'	1-3-2'-4'
	$15^\circ$	14-16-2'-4'	1-3-13'-15'
	$30^\circ$	1-14-2'-13'	3-16-4'-15'



**Figure 9.** Single tooth–coil (1 slot–pitch winding) arrangements and EMF phasor diagrams for 24 slot/22 pole single and DTP PMSMs with different angle displacements [47]. (a) DTP,  $\beta = 0^\circ$ ; (b) DTP,  $\beta = 15^\circ$ ; (c) DTP,  $\beta = 30^\circ$ ; (d) single three–phase.

With the winding arrangements shown in Figures 8 and 9 and Table 10, the winding factors of the DTP PMSMs with different slot/pole number combinations, different angle displacements, and different coil pitch numbers are given in Table 11.

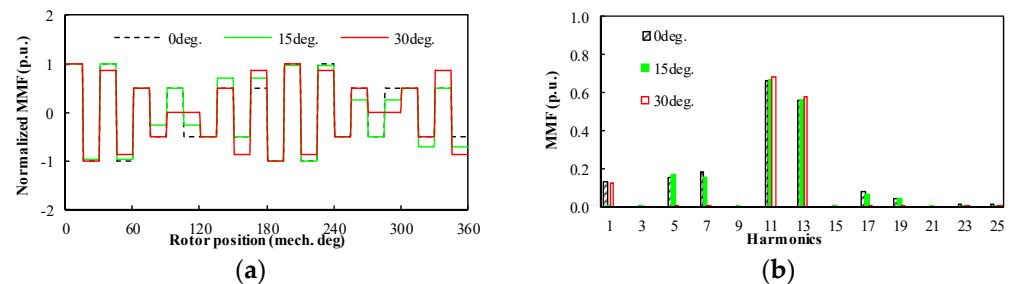
**Table 11.** Winding factors of DTP PMSMs with different winding configurations.

Angle Displacement, $\beta$	$0^\circ$	$15^\circ$	$30^\circ$
24-slot/10-pole, $y = 2$			
$K_d$	0.958	0.968	9.991
$K_p$	0.966	0.966	0.966
$K_w$	0.925	0.933	0.958
24-slot/22-pole, $y = 1$			
$K_d$	0.958	0.968	9.991
$K_p$	0.991	0.991	0.991
$K_w$	0.949	0.958	0.980

From the winding factors of the fundamental components shown in Table 11, it can be seen that 24 slot/22 pole machines feature higher winding factors than their 24 slot/10 pole counterparts. Since the higher winding factor suggests higher fundamental back-EMF components and average output torque, it is assumed that the 24 slot/22 pole DTP PMSM features the highest output torque performance. Furthermore, among the same machines with  $0^\circ$ ,  $15^\circ$ , and  $30^\circ$  angle displacements, the  $30^\circ$  machine features the highest winding factor and the  $15^\circ$  machine features a higher winding factor than the  $0^\circ$  machine.

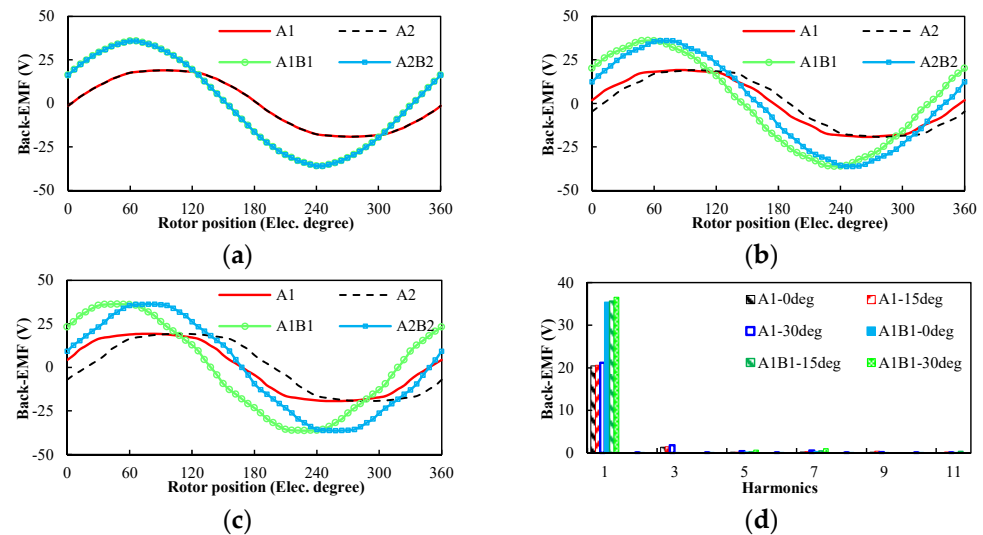
To demonstrate the analyses of the winding factors in this section and to show the electromagnetic performances of DTP PMSMs, the back-EMF and torque characteristics of 24-slot/22-pole DTP PMSMs with tooth-coil ( $y = 1$ ) and different angle displacements under different conditions are also presented. For the DTP PMSMs with  $0^\circ$ ,  $15^\circ$ , and

30° angle displacements under healthy conditions, the stator MMFs and spectra of each condition are shown in Figure 10.



**Figure 10.** Stator MMF distributions and the spectra for 24 slot/22 pole DTP PMSMs with different angle displacements under healthy conditions. (a) Stator MMF distributions. (b) Spectra of stator MMFs.

It can be seen that the amplitudes of the working harmonics (the 11th harmonics) are similar in the three machines, and the amplitudes of the different angle displacements correspond to their winding factors. Although the MMF distributions of the three angle displacements look similar, their harmonic contents are different. The  $(12k \pm 5)$ -th ( $k$  is an integer) harmonics, i.e., the 5th, 7th, 17th, and 19th harmonics, are eliminated in the 30° angle displacement, while the  $(24k \pm 1)$ -th ( $k$  is an integer) harmonics, i.e., the 1st, 23rd, and 25th harmonics for the 15° angle displacement are cancelled. The phase- and line-back-EMFs of the DTP PMSMs with these angle displacements can be obtained by using the finite element method; the values are presented in Figure 11a–c. The spectra of the phase- and line-back-EMFs are presented in Figure 11d.

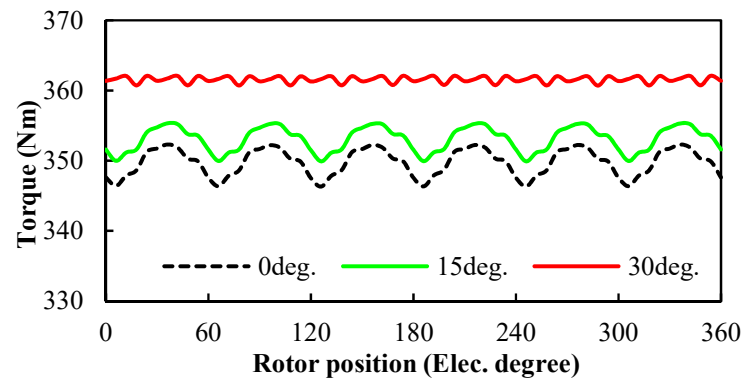


**Figure 11.** Phase- and line-back-EMFs and spectra for the 24-slot/22-pole DTP PMSMs with different angle displacements, 400 rpm. (a)  $\beta = 0^\circ$ ; (b)  $\beta = 15^\circ$ ; (c)  $\beta = 30^\circ$ ; (d) spectra.

As shown in Figure 11, the displacements between the phase- and line-back-EMFs of the two winding sets are 0°, 15°, and 30°, respectively, in the three machines. The fundamental amplitude in the 30° angle displacement is about 3.53% which is higher than that in the 0° counterpart, and 2.3% higher than that in the 15° counterpart, which is in agreement with their winding factors.

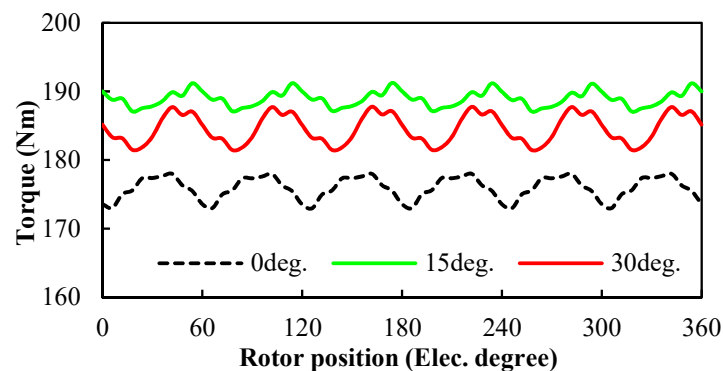


The electromagnetic torque performances of the machines with different angle displacements under healthy conditions are shown in Figure 12. The input current angle of each angle displacement is adjusted to maximize the output torque. It can be seen that the machine with  $30^\circ$  displacement produces the highest output torque, followed by the  $15^\circ$  machine and the  $0^\circ$  machine. Besides the advantages in average torque, the  $30^\circ$  angle displacement features the lowest torque ripple among the three angle displacements because of the cancellation of the 6th torque harmonics. The torque ripple of the  $15^\circ$  angle displacement is slightly lower than that of its  $0^\circ$  counterpart.



**Figure 12.** Electromagnetic torque performances of 24 slot/22 pole DTP PMSMs with different angle displacements under healthy condition.

Besides the healthy conditions, the three-phase open-circuit (OC) condition, in which one winding set is open-circuited and the other works continuously, is also considered. The electromagnetic torque performances of the machine with different angle displacements under OC conditions are shown in Figure 13. It can be seen that the  $15^\circ$  displacement features the highest torque output under these conditions instead of the  $30^\circ$  displacement under healthy conditions.



**Figure 13.** Electromagnetic torque performances of 24 slot/22 pole DTP PMSMs with different angle displacements under three-phase OC conditions.

It should also be mentioned that the average torques produced under OC conditions (Figure 13) are clearly lower than those produced under healthy conditions (Figure 12). To maintain the torque capability of the machine, the input currents need to be increased. The variations of average torque with input current amplitudes in the machines with different configurations under three-phase OC conditions are shown in Figure 14. It can be concluded that the  $15^\circ$  displacement offers the best over-rating capability under three-phase OC conditions, compared with its  $0^\circ$  and  $30^\circ$  counterparts. The superiority of the over-rating capability in the  $15^\circ$  displacement under three-phase OC conditions can be explained by its relatively low sub-harmonic distributions [47]. Furthermore, it is also

suggested that the 15° winding configuration features the lowest PM demagnetization risk among the three winding configurations, because the peak values of flux densities produced by the armature reaction are the lowest in the 15° winding configuration [47].

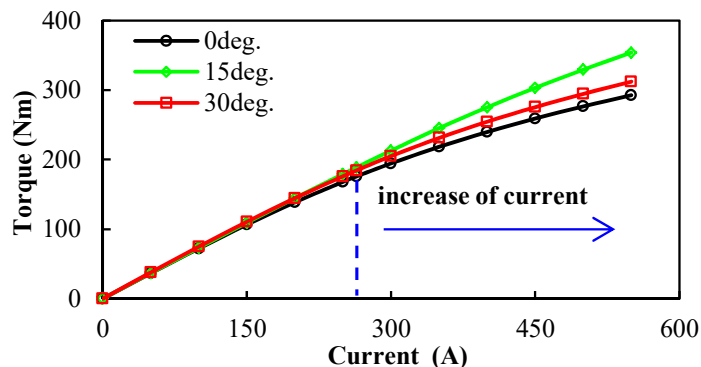


Figure 14. Average torque output with increased currents for 24 slot/22 pole DTP PMSMs with different angle displacements under three-phase OC conditions.

### 5. Control Methods

#### 5.1. Field Oriented Control (FOC)

The most common control method in DTP drives is the well-known field-oriented control (FOC, or vector control). It is comprised of inner current loops and an outer speed loop, as shown in Figure 15. The values  $\omega_r^*$ ,  $i_q^*$ ,  $i_d^*$ ,  $i_{z1}^*$ , and  $i_{z2}^*$  are the reference values for the speed and currents, respectively. It should be noted that  $i_q^*$  is the tracking maximum torque per ampere (MTPA) to operate. The values  $\omega_r$ ,  $i_q$ ,  $i_d$ ,  $i_{z1}$ ,  $i_{z2}$  are the measured values (feedback values) for the speed and currents, respectively. The values  $u_{d,q}$  are the outputs of the current proportional integral (PI) controllers, and then  $u_{\alpha,\beta}$  are obtained by transformation, as the input of the modulation strategy to generate the proper switching signals  $S_{ABC}$  and  $S_{XYZ}$ . The value  $\theta_s$  represents the electrical rotor angle. Unlike three-phase machines, the DTP machine suffers from large low-order current harmonics due to its inherent low impedance for the 5th and 7th harmonics, which may be caused by back-EMF distortion, inverter non-linearity, modulation strategies, and asymmetry [8,9]. Hence, the recent development of FOC mainly focuses on the current harmonic reduction for DTP machines.

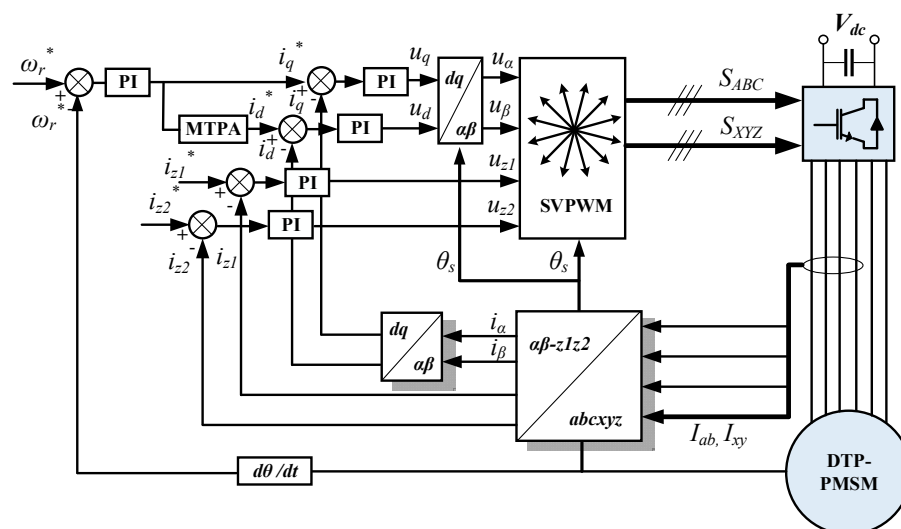
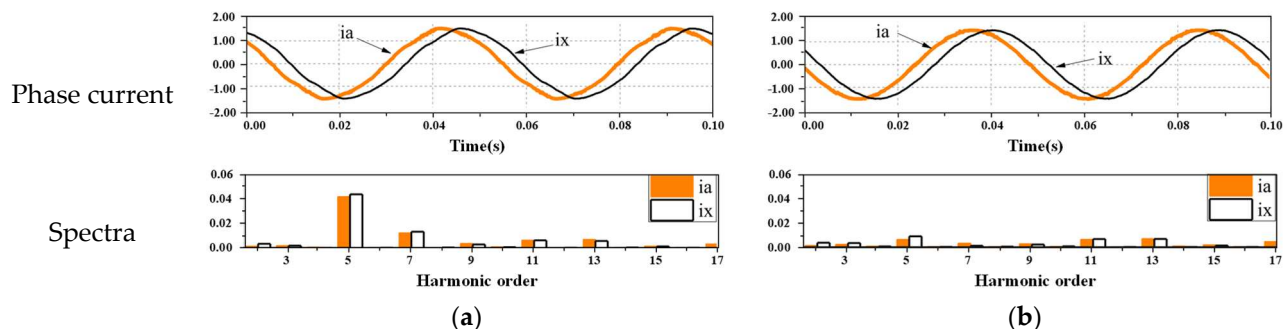


Figure 15. FOC diagram for DTP PMSMs.

One way to reduce current harmonics is the use of double synchronous reference frames current control, which is based on the two individual dq-axis modelling method and controls the two sets of windings separately. It has been introduced into DTP IMs [55,56] and PMSMs [54,57,58,68–78] and provides benefits such as its excellent steady-state performance, easy implementation in practical applications, and its ability to suppress the current unbalance resulting from asymmetries between the two sets of three-phase windings [54,57]. However, the two-individual current control may develop instability issues if a strong magnetic coupling between two sets exists, as concluded in [58,68]. Therefore, the VSD current control is proposed in FOC to overcome these drawbacks [68], as well as in  $0^\circ$  and  $60^\circ$  DTP topologies [79]. Because the PI regulator has the inherent drawbacks of the limited control capability to the AC components, synchronous frame PI controllers [69–71] and resonant controllers [68,72–74] are introduced in DTP drives as alternatives through which to suppress the 5th and 7th harmonic components (AC components). It is noted that the resonant (PIR) [72,73] or quasi-resonant (QPIR) [75] controller parallel with PI regulator (PIR) provides infinite gain at the resonant frequency and, therefore, the AC components (the 5th and 7th harmonic components) in the  $z_1$ – $z_2$  subspace can be suppressed effectively with a resonant controller. Moreover, other alternatives, such as the disturbance observer (DOB) [76], the extended state observer (ESO) [77] and the virtual impedance [78] are also extended to DTP PMSMs to obtain benefits in terms of performance and robustness. In particular, a multiple synchronous reference frame (MSRF) current harmonic regulation technique, proposed in [80,81] is able to decouple not only the 5th and 7th harmonics, but also the 11th and 13th harmonics in DTP PMSMs. This concept of the MSRF technique also features the potential to be extended to other multi three-phase machine systems.

Taking results in [68,78] as examples, it is clear from Figures 16a and 17a that the phase current suffers from large current harmonics, especially the 5th and 7th harmonics, when no compensation approaches are employed in the harmonic-related subspace. By utilizing resonant [68] and the virtual impedance [78] current regulators, the phase current harmonics can be reduced significantly, as shown in Figures 16b and 17b, where  $i_a$  and  $i_x$  are the stator currents in phases  $a$  and  $x$ , respectively.



**Figure 16.** Measured currents and spectra for PIR method [68]. Top: phase currents in phase  $a$  ( $i_a$ ) and  $x$  ( $i_x$ ); bottom: spectra. (a) without compensation and (b) with compensation.

Another relevant research activity is related to torque enhancement. In the DTP machines, injecting the low-order harmonics into the PM shaping and phase currents are both effective ways to increase the torque capability of the machines [82–84]. In [82] and [83], zero-sequence current components (the third current harmonics) injection is employed in DTP-IMs [82] and DTP-PMSMs [83], respectively, as shown in Figure 18. Figure 19 shows the finite element analysis (FEA) and experimental results with or without the third current harmonic injection. It is obvious that the torque improves significantly in both 12 slot/8 pole and 12 slot/10 pole machines, and the experimental results validate the torque enhancement as well. Furthermore, 5th and 7th current harmonics injection is investigated in [84]. According to the results of relevant research, the improvement of the overload torque due to the third-order current harmonic injection can be up to 15%. However, the improvement of the overload torque for the 5th and 7th harmonic injection is

only 7%, although it offers the benefits of its simple hardware structure and the lack of the extra requirement of current sensors, compared to the method of third current harmonic injection. The value  $I_m$  represents the amplitude of the phase current.

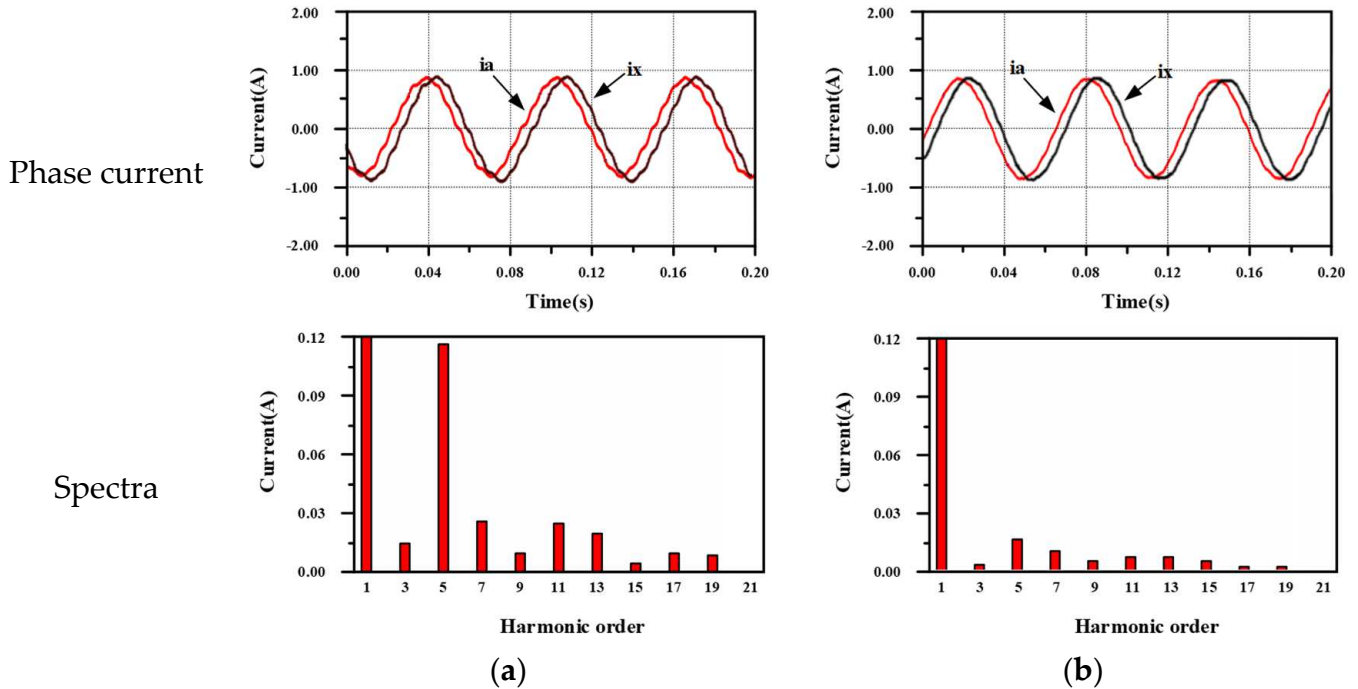


Figure 17. Measured currents and spectra for virtual impedance method [78]. Top: phase currents in phase a ( $i_a$ ) and x ( $i_x$ ); bottom: spectra. (a) without compensation and (b) with compensation.

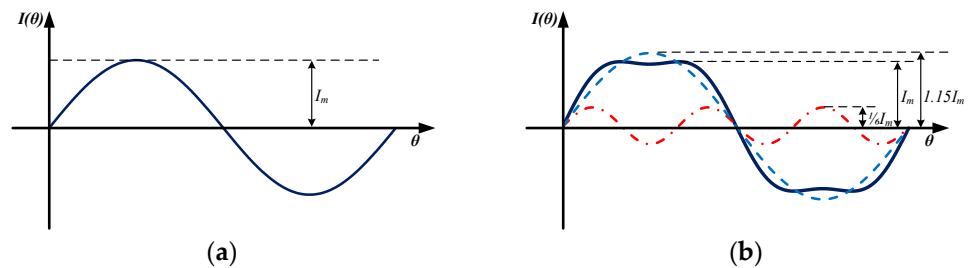


Figure 18. Current waveforms. (a) No harmonic injection current (Sine). (b) Third harmonics injection current (Sine + 3rd) [83].

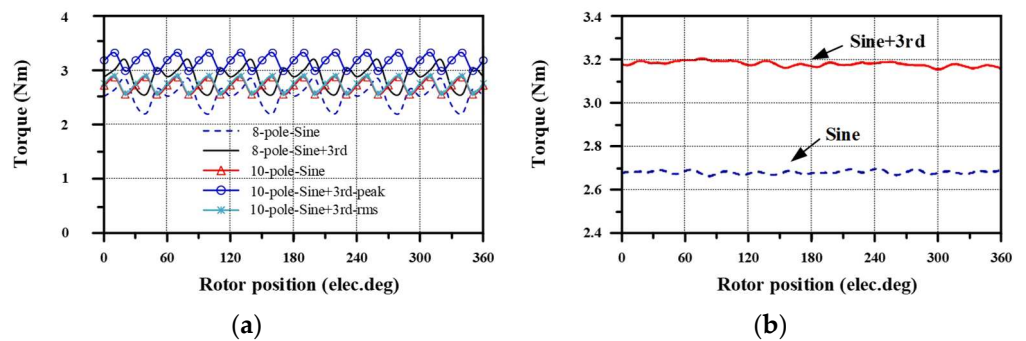


Figure 19. FEA and experimental results for third current harmonic injection [83]. (a) FEA results of the torque for 12 slot/10 pole and 12 slot/10 pole DTP-SPMSM. (b) Measured torque of a 12-slot/10-pole DTP-SPMSM.

### 5.2. Direct Torque Control (DTC)

Direct torque control (DTC) aims to control directly the stator flux and the torque by selecting the appropriate inverter state. DTCs can be classified into three categories: switching-table based DTC (ST-DTC) [85–95], the duty-ratio-based ST-DTC (D-DTC) [96,97] and space vector modulation DTC (SVM-DTC) [98,99].

The ST-DTC was firstly adapted to DTP machines in [85], which employs, when it only employed flux and torque hysteresis regulators and a look-up table to impose machine flux and torque, as shown in Figure 20. The  $\omega_r^*$ ,  $\Psi_s^*$ , and  $T_e^*$  are the reference values for the speed, stator flux, and torque, respectively. The values  $\omega_r$ ,  $\Psi_s$ , and  $T_e$  are the measured values (feedback values) for the speed, stator flux, and torque, respectively. The values  $I_{ab}$  and  $I_{xy}$  represent the measured currents in phases A, B, X, and Y. The value  $V_{dc}$  is the dc-link voltage. The values  $V_s$  and  $I_s$  represent the stator voltage and current after transformation. The method offers the benefits of fast response and dynamic performance, but suffers from large current harmonics, as concluded in [86–91]. The Redesign of the torque and flux regulators is investigated in [86], where it reduced current harmonics and torque ripples effectively, albeit with at the cost of complicating the control structure. In order to reduce current harmonics and maintain a simple structure, the reduction of current harmonics for ST-DTC has recently focused on the definition of switching table and virtual vectors (VVs) selection strategy, which was first investigated in [87]. By employing two groups of space VVs (i.e., virtual voltage vector) and setting the amplitude of the synthetic voltage vector to zero in harmonic-related subspaces [87,88], the stator current harmonics can be significantly reduced. The switching look-up table in [87] is shown in Figure 21 and Table 12. Further, the back-EMF harmonics are considered and selectively [90] and fully [91] compensated in an ST-DTC employing a virtual vector based on two or three groups of VVs, respectively. Additionally, the authors of [100] introduced an additional current loop to determine the optimal dwell times of applied voltage vectors; the current harmonics caused by back-EMF distortion were reduced as well. Furthermore, the reduction of torque ripple using virtual VVs, and the improvement of the performance by employing a non-linear observer are also analyzed in [92] and [93,94], respectively. For reducing the torque ripples, two virtual voltage vectors are synthesized and a five-level torque regulator is employed corresponding in [88]. In summary, the experimental results for conventional ST-DTCs and ST-DTCs proposed in [87,88] are summarized and compared in Figure 22. It is clear that the current harmonics are effectively compensated and torque ripples are reduced as well when virtual voltage vectors are employed, compared to conventional ST-DTC.

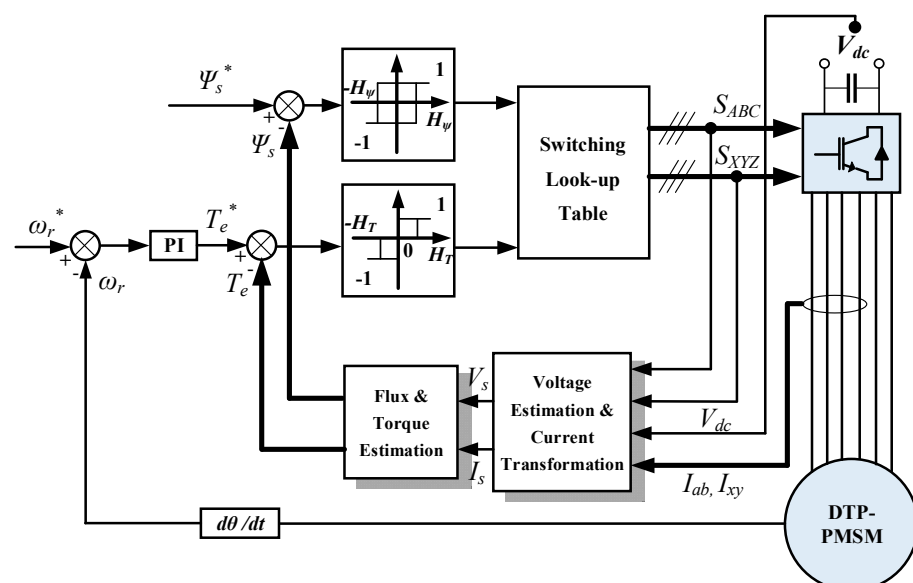


Figure 20. ST–DTC diagram for DTP machines.

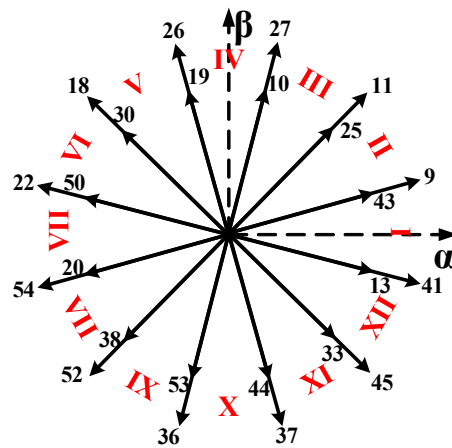


Figure 21. VVs and sections in [87].

Table 12. Switching table of virtual vector ST–DTC [87].

$\psi_s$	$T_e$	I	II	III	IV	V	VI
1	1	$V_{27}, V_{10}$	$V_{26}, V_{19}$	$V_{18}, V_{30}$	$V_{22}, V_{50}$	$V_{54}, V_{20}$	$V_{52}, V_{38}$
	0	$V_0, V_{63}$	$V_0, V_{63}$	$V_0, V_{63}$	$V_0, V_{63}$	$V_0, V_{63}$	$V_0, V_{63}$
	-1	$V_{37}, V_{44}$	$V_{45}, V_{33}$	$V_{41}, V_{13}$	$V_9, V_{43}$	$V_1, V_{25}$	$V_{27}, V_{10}$
-1	1	$V_{26}, V_{19}$	$V_{18}, V_{30}$	$V_{22}, V_{50}$	$V_{54}, V_{20}$	$V_{52}, V_{38}$	$V_{36}, V_{53}$
	0	$V_0, V_{63}$	$V_0, V_{63}$	$V_0, V_{63}$	$V_0, V_{63}$	$V_0, V_{63}$	$V_0, V_{63}$
	-1	$V_{36}, V_{53}$	$V_{37}, V_{44}$	$V_{45}, V_{33}$	$V_{41}, V_{13}$	$V_9, V_{43}$	$V_{11}, V_{25}$
$\psi_s$	$T_e$	VII	VIII	IX	X	XI	XII
1	1	$V_{36}, V_{53}$	$V_{37}, V_{44}$	$V_{45}, V_{33}$	$V_{41}, V_{13}$	$V_9, V_{43}$	$V_{11}, V_{25}$
	0	$V_0, V_{63}$	$V_0, V_{63}$	$V_0, V_{63}$	$V_0, V_{63}$	$V_0, V_{63}$	$V_0, V_{63}$
	-1	$V_{26}, V_{19}$	$V_{18}, V_{30}$	$V_{22}, V_{50}$	$V_{54}, V_{20}$	$V_{52}, V_{38}$	$V_{36}, V_{53}$
-1	1	$V_{37}, V_{44}$	$V_{45}, V_{33}$	$V_{41}, V_{13}$	$V_9, V_{43}$	$V_{11}, V_{25}$	$V_{27}, V_{10}$
	0	$V_0, V_{63}$	$V_0, V_{63}$	$V_0, V_{63}$	$V_0, V_{63}$	$V_0, V_{63}$	$V_0, V_{63}$
	-1	$V_{27}, V_{10}$	$V_{26}, V_{19}$	$V_{18}, V_{30}$	$V_{22}, V_{50}$	$V_{54}, V_{20}$	$V_{52}, V_{38}$

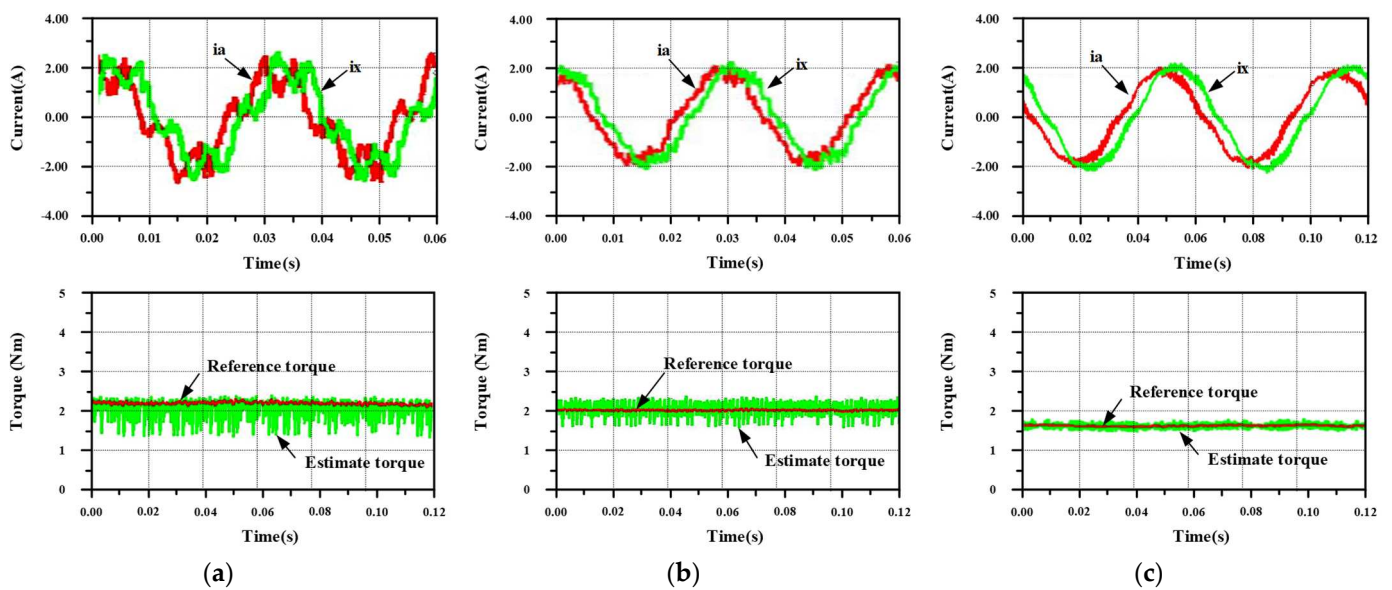
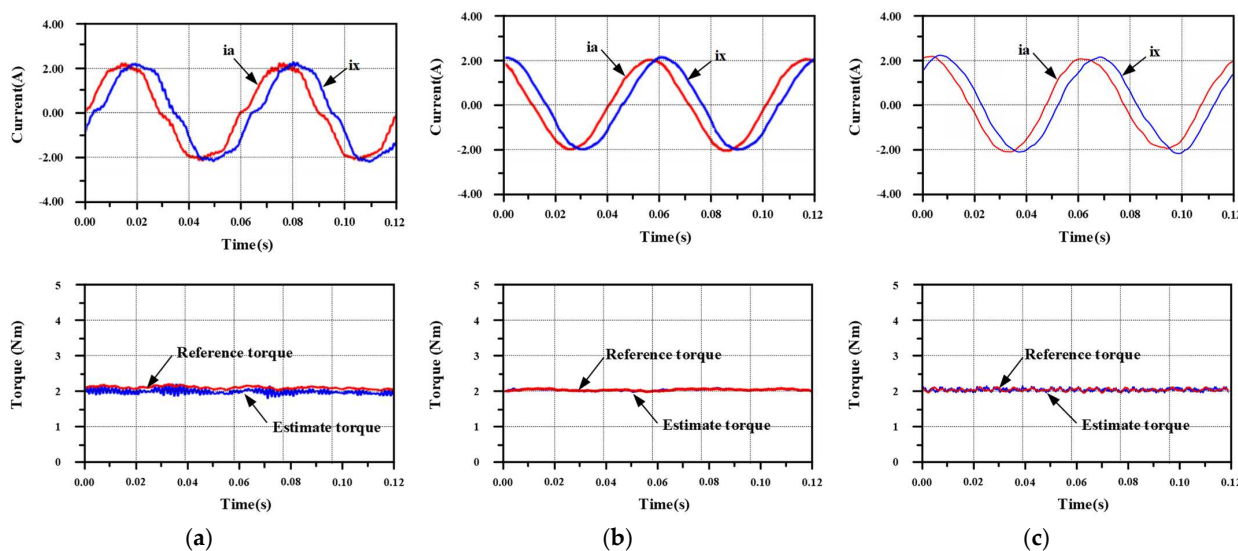


Figure 22. Experimental comparison for conventional ST–DTC, ST–DTC proposed in [87] and ST–DTC proposed in [88]. Top: phase currents in phases a ( $i_a$ ) and x ( $i_x$ ); bottom: torque. (a) Conventional ST–DTC. (b) ST–DTC proposed in [87]. (c) ST–DTC proposed in [88].

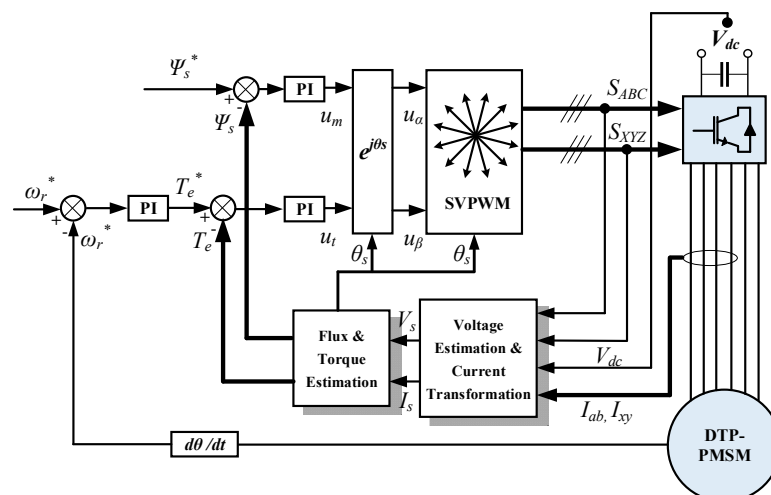
However, although virtual voltage vector injections are effective at reducing current harmonics and torque ripples, switching-table-based DTCs (ST-DTCs) still suffer from two inherent drawbacks:

- The look-up table in DTC leads to variable switching frequency, which is not suitable for high-power applications;
- The hysteresis regulator inevitably causes large torque and flux ripples in ST-DTC.

Hence, the duty-ratio-based ST-DTC (which divides one sampling period into two intervals and applies active vectors and zero vectors together) was adapted to DTP machines in [96] and obtained the reduction of torque ripples, but it still suffered from drawbacks, such as its variable switching frequency [97]. Therefore, SVM-DTC, presented in Figure 23, was adapted to DTP drives to deal with the torque and flux ripple as well as the variable switching frequency. It employs torque, flux PI controllers and space vector modulation to replace the hysteresis regulators and look-up table in ST-DTC, as shown in Figure 24. The values  $u_m$  and  $u_T$  are the outputs of the torque, flux PI controllers; after transformation,  $u_\alpha$  and  $u_\beta$  are obtained as the inputs of SVPWM to generate the switching signals  $S_{ABC}$  and  $S_{XYZ}$ . The value  $\theta_s$  represents the electrical rotor angle. In this way, the flux and torque ripples can be reduced significantly, and constant switching frequency can be achieved, but this method features the disadvantage of a deteriorating dynamic response, as analyzed in [96,97].



**Figure 23.** Measured results for duty–ratio–based DTC [96], PWM–based DTC [97], and SVM–DTC. Top: phase currents in phases a ( $i_a$ ) and x ( $i_x$ ); bottom: torque. (a) Duty–ratio–based DTC [96]. (b) PWM–based DTC [97]. (c) SVM–DTC.



**Figure 24.** SVM–DTC diagram for DTP machines.

### 5.3. Model Predictive Control (MPC)

Model predictive control (MPC) is based on a model of the real system, also called the “predictive model”, and is used to predict its future evolution. The prediction is carried out for possible switching states to determine which one minimizes a defined cost function. The basic MPC structure is shown in Figure 25. The values  $i_d^{t+1}, i_q^{t+1}$  are the predictive currents at instant  $t + 1$ , which are calculated by the measured currents  $i_d^t, i_q^t$  at instant  $t$ . Next, the proper switching signals  $S_{ABC}$  and  $S_{XYZ}$  are obtained by the cost function. According to the different cost functions, three different control constraints are included, namely the current predictive control (MPCC), the torque predictive control (MPTC), and the flux predictive control (MPFC).

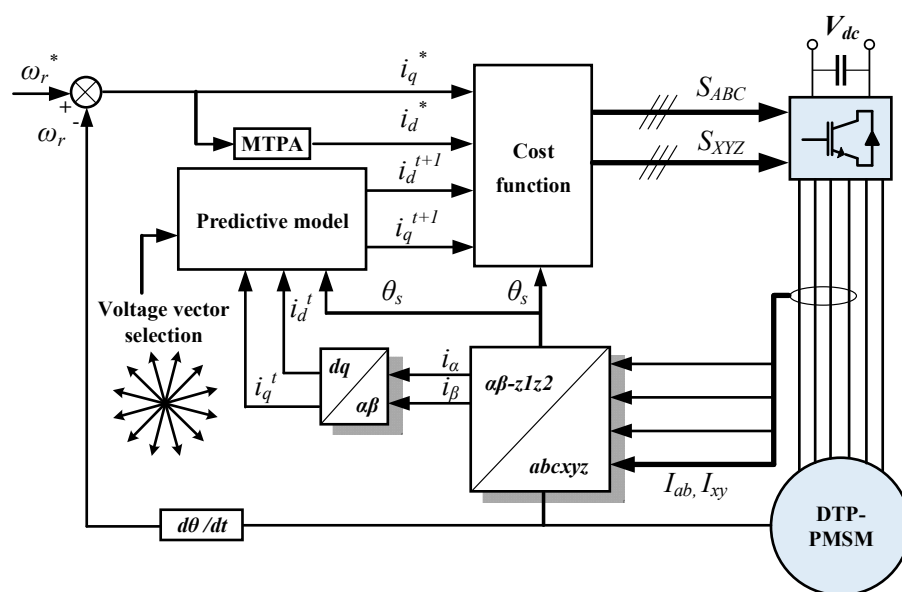


Figure 25. MPC diagram for DTP PMSMs.

The MPCC was firstly adapted to DTP drives in [101], where only the 12 outer vectors of the 64 VVs (the largest) are employed to reduce the computation burden. The cost function is expressed as:

$$g = \left| i_\alpha^* - i_\alpha^{t+1} \right| + \left| i_\beta^* - i_\beta^{t+1} \right| + \lambda \left( \left| i_{z1}^* - i_{z1}^{t+1} \right| + \left| i_{z2}^* - i_{z2}^{t+1} \right| \right). \tag{15}$$

where  $\lambda$  is a weighting factor between phase currents in the  $\alpha\beta$  and  $z_1z_2$  subspaces;  $i_\alpha^*, i_\beta^*, i_{z1}^*, i_{z2}^*$  are the current references in the  $\alpha\beta$  and  $z_1z_2$  subspaces, respectively; and  $i_\alpha^{t+1}, i_\beta^{t+1}, i_{z1}^{t+1}, i_{z2}^{t+1}$  are the predictive currents in the  $\alpha\beta$  and  $z_1z_2$  subspaces at instant  $t + 1$  calculated by the measured currents at instant  $t$ .

It is notable that the computation burden increases significantly for multiphase machines, while the VVs increase exponentially with the number of phases. Furthermore, MPCC methods with the cost function of minimizing current harmonics and reducing computation cost are investigated in [102] and [103], respectively. The selected voltage vector combined with a zero vector, namely, one-step modulation predictive current control (OSPC), or PWM-MPCC, is introduced in, where the current harmonics were suppressed further and the steady-state performance improved effectively. However, the active vectors in [102–104] are the same as those in [101], where only the largest vectors are employed. Although some improved techniques are utilized in [102–104], the system still suffers from current harmonics caused by uncontrolled harmonics-related components. Hence, a virtual VVs strategy synthesized by the largest and the second-largest actual vectors (synthesized by two groups of VVs) was introduced to MPCC for DTP machines, as described in [105]. Similar to the virtual vector approach in the DTC method, the virtual vectors ensure null



$z_1$ – $z_2$  voltages on average during the sampling period, thereby reducing the current harmonics. Moreover, two groups of virtual vectors (synthesized by three groups of VVs) aiming at harmonic currents reduction are introduced in [106], and the deadbeat current control method is also introduced to reduce the computing time with the increase of the number of employed VVs [106]. This technique for two groups of synthesized virtual vectors is further refined in [107,108], where a two-step procedure and a dual virtual vector are involved to compensate the harmonics caused by machine asymmetries, dead time effects, and back-EMF harmonics, respectively. Furthermore, some MPCC methods aiming at other optimal goals are also developed to reduce the current harmonics. For example, torque ripple reduction and DC-link voltage utilization increase are analyzed in [109,110]. Moreover, an autoregressive model with exogenous variables and a disturbance observer are employed to compensate for the effects of parameter mismatch errors and unmodelled dynamics in [111,112], respectively.

MPTC aims at minimizing the torque ripple and flux ripple, and the cost function can be expressed as:

$$g = \left| T_e^* - T_e^{t+1} \right| + \lambda \left| \psi_s^* - \psi_s^{t+1} \right|. \quad (16)$$

where  $\lambda$  is a weighting factor between torque and stator flux;  $T_e^*$  and  $\psi_s^*$  are the torque and stator flux references, respectively; and  $T_e^{t+1}$  and  $\psi_s^{t+1}$  are the predictive torque and stator flux at instant  $t+1$  calculated by measured torque and stator flux at instant  $t$ .

The viability of the MPTC is investigated in [113], where the virtual vector strategy is employed to reduce current harmonics in the MPTC. Similarly, the selected voltage vector combined with a zero vector is also introduced in [114] and [115] to reduce the torque ripple and flux ripple, and fixed switching frequency in MPTC, respectively. Further, a deadbeat-based MPTC is introduced in [116] to reduce both the harmonic currents and computation time simultaneously.

A MPFC for DTP machines was first evaluated in [117], and the cost function for MPFC is expressed as:

$$g = \left| T_e^* - T_e^{t+1} \right| + \lambda_1 \left| \psi_s^* - \psi_s^{t+1} \right| + \lambda \left( \left| \psi_{z1}^* - \psi_{z1}^{t+1} \right| + \left| \psi_{z2}^* - \psi_{z2}^{t+1} \right| \right). \quad (17)$$

where  $\lambda_1$  and  $\lambda_2$  are the weighting factors between torque and stator fluxes in the  $\alpha\beta$  and  $z_1z_2$  subspaces, respectively;  $\psi_{z1}^*$  and  $\psi_{z2}^*$  are the stator fluxes references in the  $z_1$  and  $z_2$  subspaces, respectively; and  $\psi_{z1}^{t+1}$  and  $\psi_{z2}^{t+1}$  are the predictive stator fluxes in the  $z_1z_2$  subspaces at instant  $t + 1$  calculated by measured torque and stator flux at instant  $t$ .

In this way, the current harmonics and the torque ripple reduce simultaneously. In summary, these three types of control strategies are compared and summarized in Table 13 with different characteristics.

**Table 13.** Control schemes for DTP PMSMs.

	FOC	DTC	MPC
Steady-state performance	High	Low	Normal
Dynamic performance	Slow	Fast	Fast
Switching frequency	Fixed	Variable	Variable
Implementation complexity	Normal	Simple	Complex
Parameter sensitivity	Normal	Normal	High
Sensorless	No	Yes	No
PWM modulator	Yes	No	No
Computation burden	Low	Low	High
Robustness	High	High	Low

## 6. PWM Techniques for FOC

### 6.1. Linear Region

As DTP machines are attracting interest for their use in high-power applications, various pulse width modulation (PWM) techniques have been developed. They can be classified into three main categories: carrier-based PWM (CPWM), zero-sequence injection-based PWM (ZSPWM), and space vector PWM (SVPWM). The CPWM method is implemented by comparing reference signals to carrier signals to determine the duty cycle for the inverter switches [118]. Particularly if the reference signals are sinusoidal, the CPWM is called sinusoidal PWM (SPWM), which is widely used in common three-phase machine drives.

One of the drawbacks of CPWM is the lack of control degrees with which to achieve a better performance [118–120]. Therefore, a phase-shift SPWM and a sawtooth carrier-based PWM were investigated in DTP machines to reduce common-mode voltage in [119,120], respectively, where phase angle shifts and the shape of carrier waves were modified to reduce the common-mode voltage. Details about the carrier shift technique in DTP machines can be found in Appendix A.

Another drawback of CPWM is its low DC bus voltage utilization. This can be improved by injecting zero-sequence components, namely ZSPWM. This method is implemented by injecting a zero-sequence component into the reference voltage in each three-phase set. A common zero-sequence signal is added to two sets of three-phase sinusoidal signals, designated as single-zero-sequence injection PWM (SZIPWM) [121,122]. Correspondingly, two different zero-sequence signals for the two sets of sinusoidal signals are employed, designated as double-zero-sequence injection PWM (DZIPWM) [56,123,124]. When double-zero-sequences are injected in DTP drives, DC bus utilization and current harmonics improve significantly compared with single-zero-sequence injection, as concluded in [56,123,124]. On the basis of this technique, the different magnitudes of the zero-sequence injection components are further investigated in symmetrical six-phase machines [125] to compensate for unbalanced loads. In [126], “trapezoidal-like” zero-sequence signals are injected to improve the performance in terms of current distortion and common-mode voltage reduction.

In multiphase inverters, the number of switching states increases in accordance with the phase number. For example, there are 64 switching states for DTP inverters. It would be more complicated to analyze and select proper switching states in DTP machines compared with three-phase machines. According to the VSD method in Section 3: Modelling, the space VVs can be transformed into two different subspaces: the  $\alpha\beta$  subspace and the  $z_1 - z_2$  subspace, as shown in Figure 26. It is notable that the groups of voltage vectors from largest to smallest magnitude in the  $\alpha\beta$  subspace are defined as  $L(D_1)$ ,  $ML(D_2)$ ,  $M(D_3)$ , and  $S(D_4)$ , and this  $\alpha\beta$  subspace magnitude-based definition has no physical meaning, as listed in Table 14.

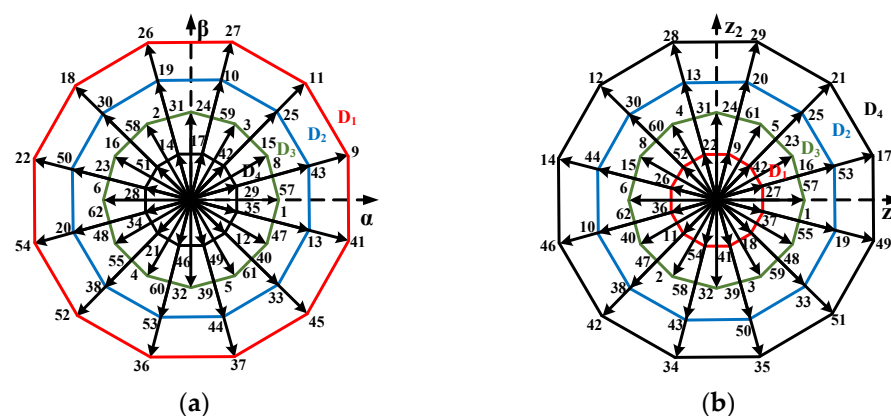


Figure 26. Space VVs for DTP inverters. (a)  $\alpha\beta$  subspace. (b)  $z_1z_2$  subspace.

**Table 14.** Magnitudes of voltage vector in different subspaces.

VVs Group	Magnitude	
	$\alpha\beta$ Subspace	$z_1z_2$ Subspace
L (D <sub>1</sub> )	$\frac{\sqrt{6}+\sqrt{2}}{6}U_{dc}$	$\frac{\sqrt{6}-\sqrt{2}}{6}U_{dc}$
ML (D <sub>2</sub> )	$\frac{\sqrt{2}}{3}U_{dc}$	$\frac{\sqrt{2}}{3}U_{dc}$
M (D <sub>3</sub> )	$\frac{1}{3}U_{dc}$	$\frac{1}{3}U_{dc}$
S (D <sub>4</sub> )	$\frac{\sqrt{6}-\sqrt{2}}{6}U_{dc}$	$\frac{\sqrt{6}+\sqrt{2}}{6}U_{dc}$

Where  $U_{dc}$  is the amplitude of the dc-link voltage.

The SVPWM based on the VSD method was first analyzed in DTP-IMs in [127], where the 12 largest vectors in the  $\alpha\beta$  subspace were utilized. However, this approach is incompetent and generates significant lower-order harmonics due to its lack of control over the components in the  $z_1z_2$  subspace. Hence, the utilization of 4 active VVs in the 2 largest vectors (4 L) to control the components in both subspaces is proposed in [62]. It is termed the 12 sector SVPWM strategy. Further, the SVPWM selected from 2 L + 2 ML [128], 3 L + 1 ML [129], 2 L + 1 ML + 1 M [130] are introduced, namely, the 24 sector SVPWM strategy. As stated in previous research, the 24 sector SVPWM method is easier to implement using DSP microcontrollers and results in less total harmonic distortion (THD) in the output waveforms of the converter, but it has a lower maximum modulation index due to the introduction of VVs with smaller amplitudes. Further, the concepts of discontinuous SVPWM [131], synchronized SVPWM [132], SVPWM using five active vectors [133] are investigated in DTP machines, and modulation restraints for SVPWM, i.e., the linear modulation range of  $z_1z_2$  subspace under an assured modulation index of the fundamental voltage, are investigated in [134], due to the existence of modulation coupling between the  $\alpha\beta$  subspace and the  $z_1z_2$  subspace.

These three types of PWM techniques are compared and summarized in Table 15. It is notable that the SVPWM strategies can be implemented by finding their CPWM equivalent, which is simpler to implement in the hardware. This requires finding the proper zero-sequence injection to the original sinusoidal reference signals, as concluded in [135,136].

**Table 15.** PWM techniques for DTP PMSMs.

	CPWM(SPWM)	ZIPWM	SVPWM
Maximum modulation index	1	1.154	1.154
Redundant switching states	No	No	Yes
Reduction of $z_1z_2$ currents	No	No	Yes
Implementation complexity	Simple	Simple	Complex

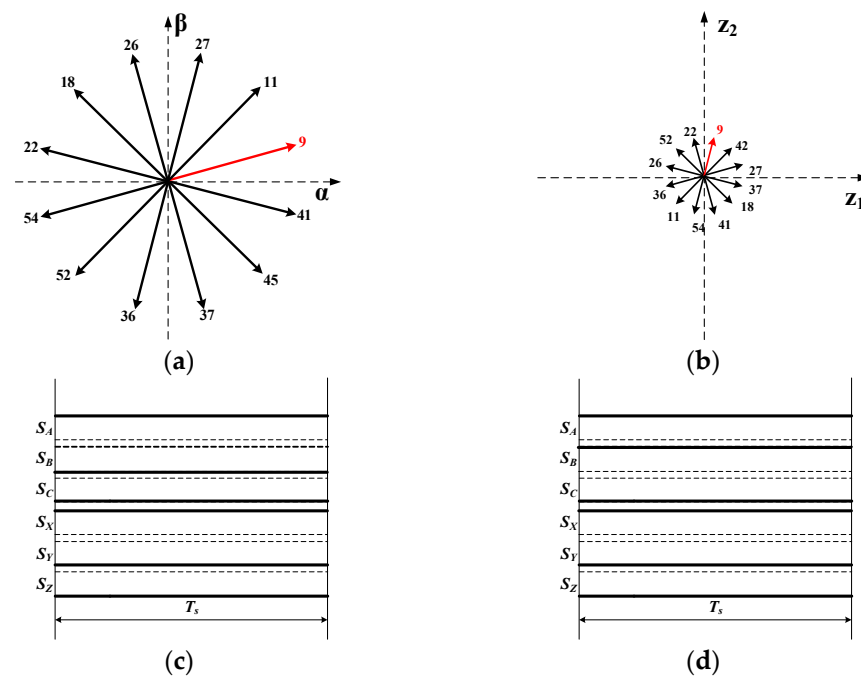
## 6.2. Overmodulation Region

In [137,138], an overmodulation (OVM) strategy is proposed on the basis of SVPWM in [62], where the desired voltage vector in the  $\alpha\beta$  subspace was synthesized using two adjacent active vectors. This resulted in large current harmonics in the  $z_1-z_2$  subspace. OVM strategies require a group of harmonics in line-neutral voltages to attain an increase in the modulation index, which inherently generates significant low-order harmonics in the  $z_1 - z_2$  subspace. To reduce harmonics in the OVM region, two different space-vector-based OVM (SVOVM) techniques are proposed in [139,140], which use four active VVs (2 L + 2 ML) and five active VVs (2 L + 1 M + 2 S), respectively. With these vectors, by formulating an optimization problem to achieve minimum root-mean-square (RMS) voltage in the  $z_1 - z_2$  subspace, the current harmonics can be reduced effectively in DTP drives. Further, an OVM technique modulated by two separately three-phase inverters (TINV-based OVM) rather than the six-phase inverter described in [139,140], is proposed in [141], where the computational cost is significantly reduced without the involving complex six-dimensional transformation discussed in previous studies.

## 7. PWM Techniques for ST-DTC

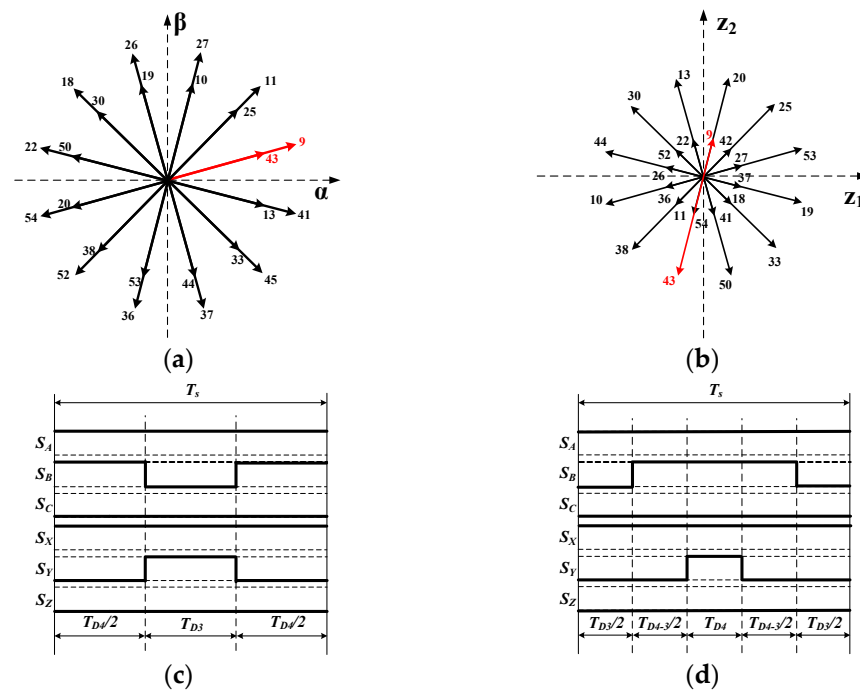
As mentioned above, for the FOC method, two adjacent vectors, or virtual vectors, are employed to synthesize all the VVs in one sector. However, in the ST-DTC method, only one voltage vector or virtual voltage vector is employed to achieve flux linkage and torque control, according to the output of the stator flux and torque hysteresis regulators and the prefixed switching table. Hence, PWM techniques for ST-DTC are totally different from the methods used in DTP drives described in Section 6.

In [85], the ST-DTC is analyzed for DTP machines. Firstly, the  $\alpha\beta$  subspace is divided into 12 sectors, and appropriate VVs are obtained through instantaneous control of the stator flux and torque. Subsequently, in order to decrease the computation burden and maximize the utilization of DC bus voltage, only the 12 largest VVs in the  $\alpha\beta$  subspace are employed (L), as shown in Figure 27. In this way, the method proposed in [85] (ST-DTC-L) is easy to implement, but it suffers from large stator current harmonics, since only the requirements of stator flux in the  $\alpha\beta$  subspace and torque are considered, and stator flux in the  $z_1 z_2$  subspace is uncontrollable.



**Figure 27.** PWM techniques in [85]. (a) Voltage vector selection strategies in  $\alpha\beta$  subspace. (b) Voltage vector selection strategies in  $z_1z_2$  subspace. (c) PWM switching sequences for V9. (d) PWM switching sequences for V11.

In order to control the components in the  $z_1z_2$  subspace and reduce current harmonics, the authors of [87] employed an ST-DTC method based on VVs in L and ML groups (ST-DTC-L + ML). Since the VVs in the L and ML groups have the same direction in the  $\alpha\beta$  subspace while the opposite direction in the  $z_1z_2$  subspace, the amplitude of the components in the  $z_1z_2$  subspace can be set to zero, as shown in Figure 28a,b; subsequently, the corresponding harmonic currents are decreased. Furthermore, in order to implement standard centralization PWM sequences, three adjacent vectors in the L group are employed to synthesize the virtual vectors, which are equivalent to the virtual vectors synthesized by the vectors in the L and ML groups. For example, the virtual vectors synthesized by V9-V11-V27 in the L groups are employed to replace the virtual vectors synthesized by V11-V25 to obtain standard PWM sequences, as shown in Figure 28c,d.



**Figure 28.** PWM techniques in [87]. (a) Voltage vector selection strategies in  $\alpha\beta$  subspace. (b) Voltage vector selection strategies in  $z_1z_2$  subspace. (c) PWM switching sequences for V11-V25. (d) PWM switching sequences for V9-V11-V27.

In [90,91], the 5th and 7th back-EMF harmonics are considered in DTP machines. Because the 5th and 7th back-EMF harmonics that possess phase shifts are unaligned with the VVs in the L and ML groups, the ST-DTC based on the VVs in the L and ML groups can only compensate for the selective order back-EMF harmonics, as concluded in [90]. Hence, in order to obtain composite vectors aligned with back-EMF harmonic components, the VVs in the M group are employed to combine with the VVs in the L and ML groups (STDTC-L + ML + M) in [91], due to their different directions with VVs in the L and ML groups, as shown in Figure 29a,b. In this way, the back-EMF harmonics can be fully compensated; consequently, the current harmonics caused by back-EMF distortion can be reduced. Further, proper PWM techniques with VVs selection from the L, ML, and M groups are proposed in [91] to obtain standard PWM sequences. For example, V59 is selected instead of V3 to combine with V10-V27 in order to generate standard PWM sequences, as shown in Figure 29c,d, where  $T_{D2}$ ,  $T_{D3}$ , and  $T_{D4}$  are the dwelling times for the applied voltage vectors.

The results of the use of different PWM techniques in ST-DTCs are summarized in Figure 30, from which it can be deduced that virtual vector synthesis by VVs in multiple groups are effective at reducing the current harmonics. However, from the perspective of dc bus voltage utilization, ST-DTC-L + ML and ST-DTC-L + ML + M are lower than ST-DTC-L, which is a clear disadvantage, as summarized in Table 16.

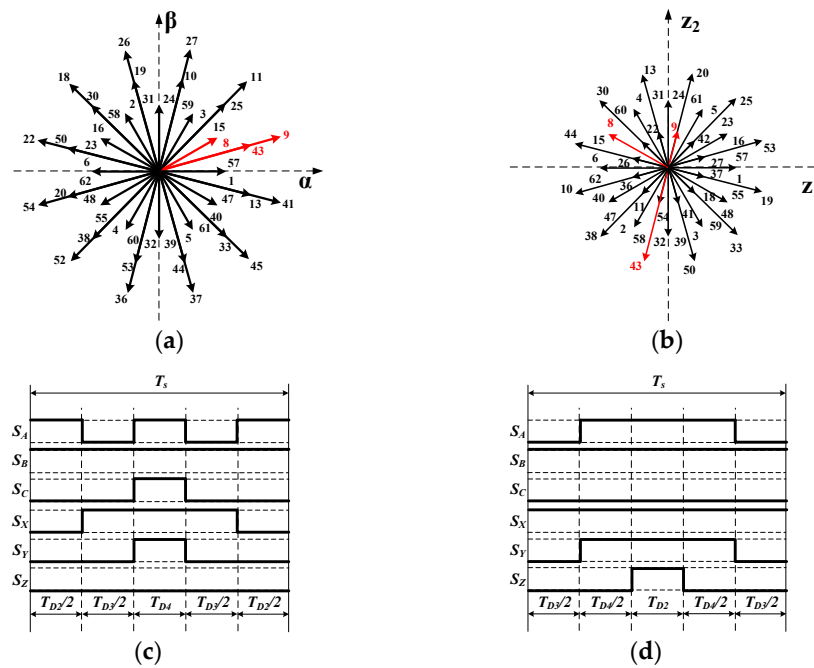


Figure 29. PWM techniques in [91]. (a) Voltage vector selection strategies in  $\alpha\beta$  subspace, (b) Voltage vector selection strategies in  $z_1z_2$  subspace, (c) PWM switching sequences for V3-V10-V27, (d) PWM switching sequences for V10-V27-V59.

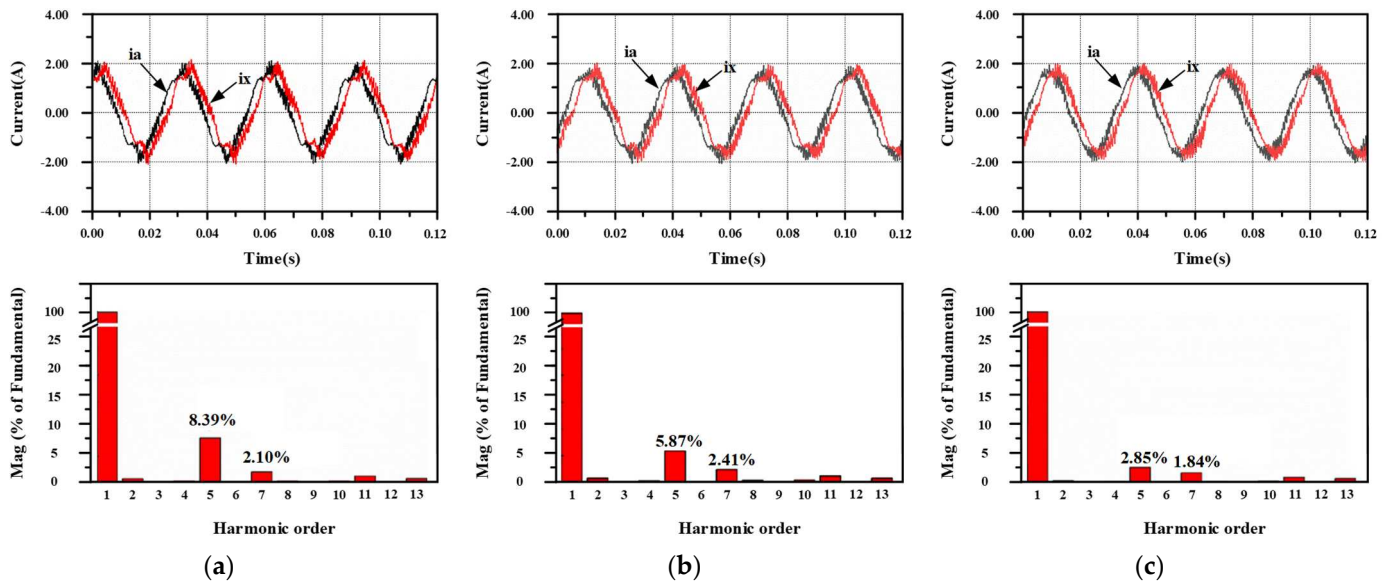


Figure 30. Experimental results. Top: phase currents in phases a ( $i_a$ ) and x ( $i_x$ ). Bottom: spectra. (a) ST-DTC-L [85]. (b) ST-DTC-L + ML [87]. (c) ST-DTC-L + ML + M [91].

Table 16. PWM techniques for ST-DTC in DTP machines.

	L	L + ML	L + ML + M
Maximum modulation index	1.12	1	0.894
Utilization of dc link voltage	$0.644U_{DC}$	$0.577U_{DC}$	$0.512U_{DC}$
Reduction of $z_1 - z_2$ currents	Worse	Normal	Good
Implementation complexity	Simple	Normal	Complex

## 8. Sensorless Control

Sensorless control aims to remove the rotor position sensor from the control system, and thus features advantages in PMSM drives in the form of cost reduction, system downsizing, and reliability enhancement [142]. The sensorless control of conventional three-phase PMSMs has been thoroughly studied so far, and the control approaches can be classified into two categories: model-based sensorless control and salient-effect-based sensorless control. The former usually utilizes the mathematical model of the machine to estimate, online, the back-EMF [143–148] and flux linkage [149–153] associated with the fundamental excitation, from which the rotor position can be further extracted. This kind of rotor position estimation is more applicable in high-speed regions but suffers from inaccuracy at low-speed and zero-speed conditions due to the model's uncertainty and inverter nonlinearity, as well as its low signal-to-noise ratio. The salient-effect-based control usually makes use of the salient effect by injecting high frequency (HF) signals to calculate the rotor position; hence, it is suitable for the low-speed and zero-speed range. With reference to the injected signals, the control approaches can be grouped as rotating [154–156] and pulsating [157] HF signal injection; pulsating HF signal injections can be further divided into pulsating sinusoidal and pulsating square-wave HF signal injections.

The sensorless control approaches mentioned above belong to the category of single-three-phase PMSM systems, and can be also extended to the MTP family. However, regarding MTP PMSMs, thanks to the additional degrees of freedom, many novel techniques of rotor position estimation have been proposed in recent years, which demonstrates the superiority of MTP PMSMs in the area of sensorless control. The author of [158] used an auxiliary resistor network to measure the third harmonic EMFs of two three-phase sets (Figure 31). According to the phase relationship between the fundamental and the third harmonic EMFs, the estimator in Figure 32 can be employed to calculate the rotor position (Figure 33).

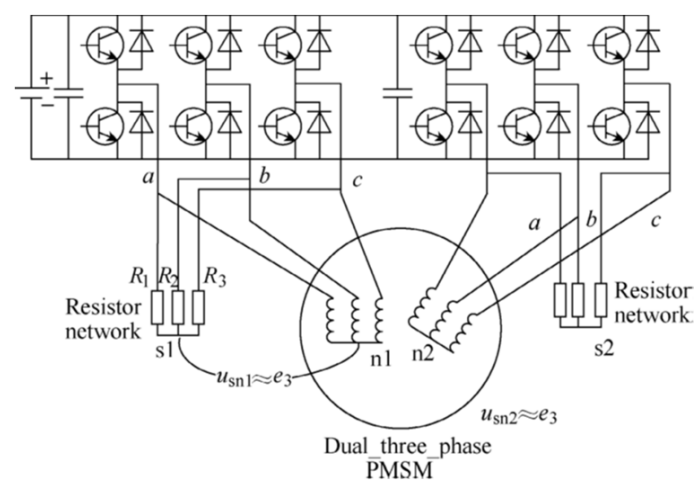


Figure 31. Measurement of the third harmonic EMFs using additional resistor network [158].

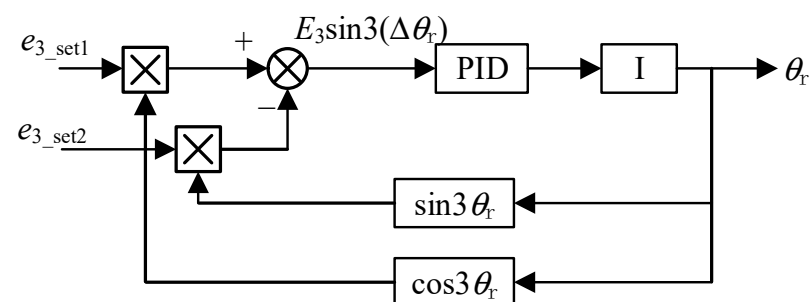


Figure 32. Rotor position estimator using third harmonic EMFs of two three-phase sets [158].

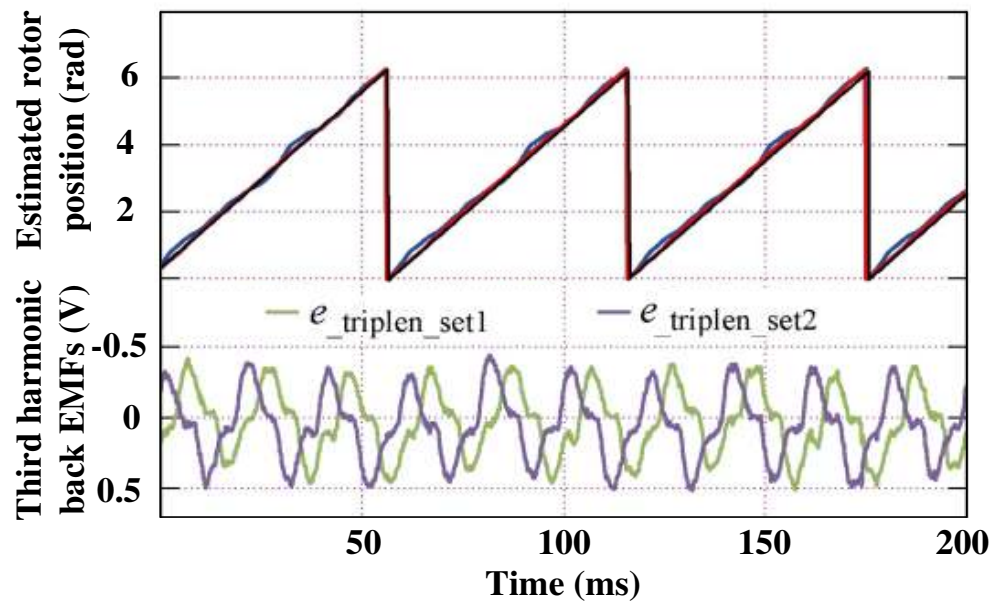


Figure 33. Measured third harmonic back-EMFs and estimated rotor position [158].

Unlike [158], the auxiliary resistor network is not required in [159,160]. The zero-sequence carrier voltage between the neutral points of two winding sets are measured after injecting HF carrier signals, and the rotor position can be derived from the measured voltage. The injected HF carrier signals can be classified into pulsating injection [159] and rotating injection [160], as shown in Table 17.

It is clear that after the pulsating and rotating HF signals are injected, the voltage difference between two isolated neutral points includes the zero-sequence carrier voltage  $u_{0sn1n2}$ , which is relevant to the rotor position and injected signals. Using the demodulation functions, the estimated errors can be calculated and then utilized to compensate for the estimated rotor position. There are clear biases and ripples in the estimated rotor position, which can be eliminated by optimizing the phase shift angle  $\varphi$  between the injection signals of two three-phase sets. Specifically, the optimal phase shift angles are  $\pi/2$  and  $2\pi/3$  for the pulsating injection and rotating injection, respectively. The overall control system is shown in Figure 34.

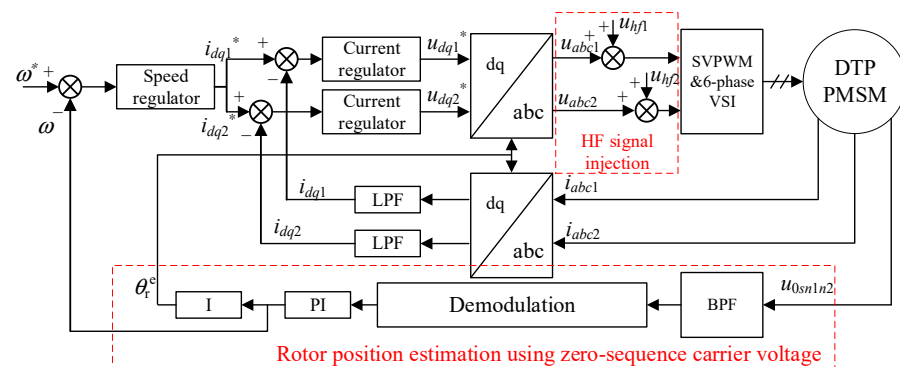


Figure 34. Overall sensorless control system using zero-sequence carrier voltage in DTP PM machine [159,160].



**Table 17.** Rotor position estimation using zero-sequence carrier voltage between two neutral points.

	Pulsating Injection [159]	Rotating Injection [160]
$u_{0sn1n2}$	$\frac{-\sqrt{2}U_c(L_0-M_0)(L_2-M_2)}{2L_0^2+2M_0^2-2M_2^2-4L_0M_0-2L_2M_2-L_2^2} \times$ $[\sin(\omega_c t + 2\theta_r + \theta_r^e - \frac{\pi}{4} - \frac{\varphi}{2})\sin(\frac{\pi}{4} + \frac{\varphi}{2}) + \sin(\omega_c t - 2\theta_r - \theta_r^e + \frac{\pi}{4} - \frac{\varphi}{2})\sin(-\frac{\pi}{4} + \frac{\varphi}{2})]$	$-\frac{2U_c \sum L_s \Delta L_s}{\sum L_s^2 - \Delta L_s^2} \sin(\omega_c t + 2\theta_r + \frac{5\pi}{6} - \frac{\varphi}{2})\sin(-\frac{5\pi}{6} + \frac{\varphi}{2}) +$ $\frac{2U_c \Delta L_s^2}{\sum L_s^2 - \Delta L_s^2} \sin(\omega_c t - 4\theta_r + \frac{2\pi}{6} - \frac{\varphi}{2})\sin(-\frac{2\pi}{6} + \frac{\varphi}{2})$
Optimal phase shift angle $\varphi$	$\varphi = \frac{\pi}{2}$	$\varphi = \frac{2\pi}{3}$
Demodulation	$LPF(u_{0sn1n2} * 4\sin(\omega_c t - 3\theta_r^e)) = \frac{-\sqrt{2}V_c(L_0-M_0)(L_2-M_2)}{2L_0^2+2M_0^2-2M_2^2-4L_0M_0-2L_2M_2-L_2^2} * \sin(2\Delta\theta)$	$LPF(u_{0sn1n2} * \cos(\omega_c t)) * \sin(2\theta_r^e) - LPF(u_{0sn1n2} * \sin(\omega_c t)) * \cos(2\theta_r^e) =$ $-\frac{2U_c \sum L_s \Delta L_s}{\sum L_s^2 - \Delta L_s^2} * \sin(2\Delta\theta)$
Test results without phase shift		
Test results with optimal phase shift		

Notes: The values  $\omega_c$  and  $U_c$  are the angular frequency and amplitude of injection signals, respectively. The value  $\theta_r$  is the real rotor position, and  $\theta_r^e$  is the estimated rotor position. The value  $\varphi$  is the phase shift angle between the injection signals of two sets. The value  $\Delta\theta$  is the estimation error. The values  $L$  and  $M$  denote the inductance and mutual inductance of machine. The values  $L_0$  and  $M_0$  denote the phase average inductance and mutual inductance. The values  $L_2$  and  $M_2$  denote the amplitudes of the phase second-order inductance and mutual inductance. The values  $\sum L_s$  and  $\Delta L_s$  are the average and differential synchronous inductances, respectively. The value  $u_{0sn1n2}$  is the voltage between two neutral points. The function  $LPF()$  means low pass filter function. The value Act\_pos means the actual rotor position. The values Est\_Pos\_V0n1n2 and Est\_Pos\_Vn1n2 mean the estimated rotor position. The value Est\_error means the estimation error.

In terms of the rotor position errors caused by the parameter uncertainty, [161] proposed a simple correction method to compensate the rotor position error for the DTP PM machine system, as shown in Figure 35.

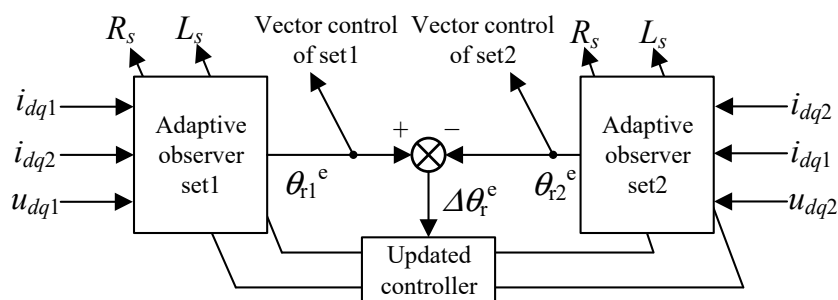


Figure 35. Rotor position correction using adaptive observers in the DTP PM machine system [161].

The outputs of two adaptive observers represent the two estimated rotor positions in two three-phase subsystems. However, due to the uncertain resistance and inductance, the two estimated positions are not identical, and the difference between the estimated rotor positions is relevant to the current distribution of the two three-phase sets, which indicates that currents with nonidentical amplitudes and phases in two sets amplify that difference. Accordingly, extra fundamental current is injected in [161] to achieve the rotor position correction. The rotor position difference  $\Delta\theta_r^e$  is then utilized to tune the machine resistance and inductance parameters in adaptive observers. The PI regulators are employed in the updated controller to guarantee that  $\Delta\theta_r^e$  can be eliminated, and the rotor position error correction is achieved simultaneously. Figure 36 shows the experimental results of rotor position error correction. The extra  $q$ -axis current of set 1 is injected at 1.5 s, and subsequently causes additional torque and transient pulsating in position errors, as shown in Figure 36a. As the updated controller works, the rotor position errors are reduced to zero at a steady-state. The extra current is removed from the system at 3.5 s, after which a short period of pulsating occurs; the error can subsequently remain at 0 degrees. Although the position errors are corrected, the injected current in one set causes additional torque and pulsating in the position estimation. To achieve a smoother correction, the extra currents are injected into both sets, as displayed in Figure 36b. The injected currents feature the same amplitude but the opposite polarity; thus, they cannot introduce any additional torque as the one-set injection does. Consequently, the rotor position errors can be smoothly regulated to 0 deg. in 0.25 s.

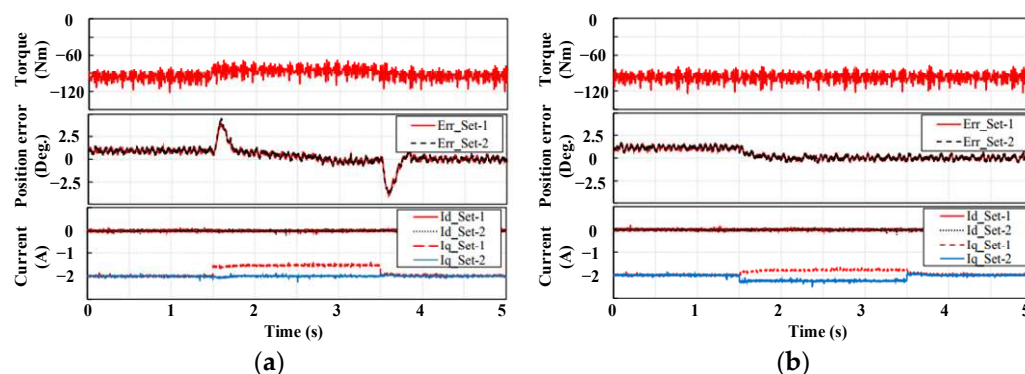


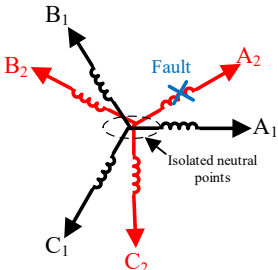
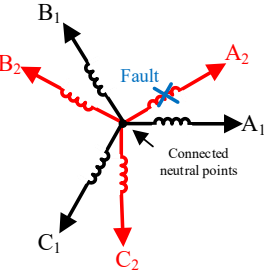
Figure 36. Experimental results of rotor position error correction. (a) One-set current injection. (b) Both set current injection [161].

## 9. Fault Tolerance Control

Fault tolerance is an important property, and makes MTP machines distinct from conventional three-phase machines. Fault tolerance control aims to utilize the additional degrees of freedom in MTP machine systems and keeps the machine continuously operating after one (or more) phase(s) develop faults. The fault usually occurs in the power switches and the machine windings, and faults in both the power switches and the machine windings cause short-circuit or open-circuit in MTP drives. Fault tolerance for short-circuit faults is only feasible in MTP machines with modular structures and winding arrangements [5,162–164]. In general, fault tolerance control for short-circuit faults involves the isolation of the faulty sets of three-phase windings, followed by the operation of the machine with the remaining sets of windings. Compared to the fault tolerance used for short-circuit faults, the most widely investigated cases in recent research have been post-fault control strategies for open-circuit faults. Most faults can be considered as open-circuit. The performances of post-fault control strategies against open-circuit faults are covered in [165–185].

The purpose of fault tolerance control is usually to generate a rotating flux field to drag the rotor using the residual healthy phases. The control strategies depend on the degrees of freedom of the machine. MTP machines can be grouped into two types, according to their connection of neutral points, namely isolated neutral points and connected neutral points, as shown in Table 18.

**Table 18.** Fault tolerant control methods of DTP PMSM.

Isolated Neutral Point Type	Connected Neutral Point Type
 <p><b>Fault tolerant control:</b></p> <ol style="list-style-type: none"> <li>1. Simply cut off the entire three-phase set with fault.</li> <li>2. Extended VSD control with negative sequence current injection.</li> </ol>	 <p><b>Optimal current control:</b></p> <ol style="list-style-type: none"> <li>1. Maximal average torque</li> <li>2. Minimal torque ripples</li> <li>3. Minimal copper loss</li> <li>4. Uniform distribution of copper loss</li> </ol> <p><b>Robust control:</b></p> <ol style="list-style-type: none"> <li>1. Fuzzy current control</li> <li>2. Robust speed control</li> </ol>

In terms of the isolated type, the most common approach is to cut off the three-phase set, in which the fault occurs, from the control system; the required torque can be equally distributed to the healthy sets. To take the DTP machine as an example, when phase  $A_2$  is faulty due to the isolated neutral point of the second set, the currents of phases  $B_2$  and  $C_2$  are identical, and can only generate a pulsating flux field, which leads to poor torque performance. Therefore, the second set can simply be abandoned, and the currents of the first set should be doubled to make up for the lost torque; in other words, the available torque and power are reduced to half of their previous rating. This case does not require the conversion of the control to the specifically designed postfault algorithm if each set is individually regulated, which is quite simple to implement and practical in industrial applications, such as railway traction [168,169] and ship propulsion [10–13]. Meanwhile, the disadvantage is clear. The healthy phases in the fault set, phases  $B_2$  and  $C_2$ , together with the corresponding switching devices, are not utilized, and the system utilization is not maximized.

To improve the system utilization of the machine with isolated neutral points, the current should be redistributed to the remaining healthy phases. The pulsating flux generated by the fault set can be decomposed into positive-sequence and negative-sequence rotating flux. The positive-sequence flux provides average torque while the negative-sequence flux generates the second-order torque ripple. The core purpose of this kind of fault tolerance control is to inject negative-sequence current into the healthy set and to counterbalance the negative-sequence flux; as a result, the average torque remains while the

torque ripple is eliminated. To implement this idea, a genetic algorithm is provided in [166] to optimize the stator currents, thereby maximizing the average torque or minimizing the torque ripple. Furthermore, the copper loss of faulty DT-PMSM with isolated neutral points is further reduced by minimizing the d-axis current of the healthy three-phase winding [178–180].

It is also possible to use modelling with open-circuit faults to achieve different control purposes. In particular, the VSD technique can decouple motor variables in several orthogonal subspaces, thereby controlling them independently [164,181–185]. Because the VSD technique can decompose the negative-sequence current in the z subspace, the control structure in [185] is greatly simplified, as shown in Figure 37. The values  $i_q^*$ ,  $i_d^*$ ,  $i_z^*$ ,  $v_q^*$ ,  $v_d^*$ ,  $v_{z1}^*$ ,  $v_{z2}^*$ ,  $v_{z3}^*$ ,  $v_{\alpha 2}^*$ ,  $v_{\beta 2}^*$ ,  $v_{\alpha}^*$ ,  $v_{\beta}^*$ ,  $v_{abc}^*$ ,  $v_x^*$ , and  $v_y^*$  are the reference values for the voltage and currents in different coordinate systems, respectively. The values  $i_{abc}$ ,  $i_x$ ,  $i_y$ ,  $i_{\alpha,\beta,z1,z2,z3}$  are the measured currents. The values  $V_{ffq-d}$  and  $V_{ffd-q}$  are the feedforward voltages to compensate for the d-q coupling. The values  $Duty_{abc}^*$  and  $Duty_{xyz}^*$  are the dwelling times for each switching signal.

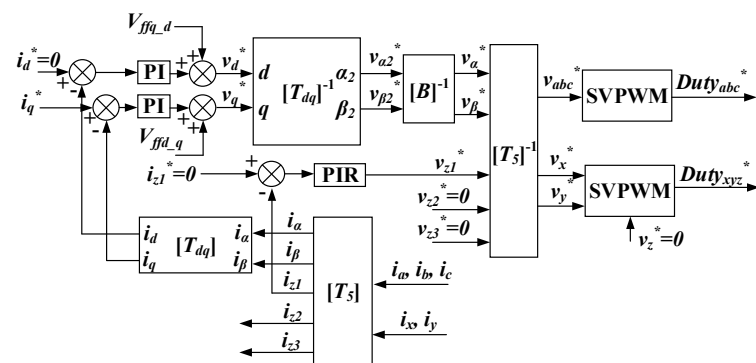


Figure 37. Fault tolerance control of DTP PMSM with one-phase open using VSD approach [185].

To eliminate the negative-sequence current, a PIR regulator is employed and the fundamental electrical frequency is utilized as the resonant frequency. Figure 38 provides the experimental results under healthy and faulty conditions.

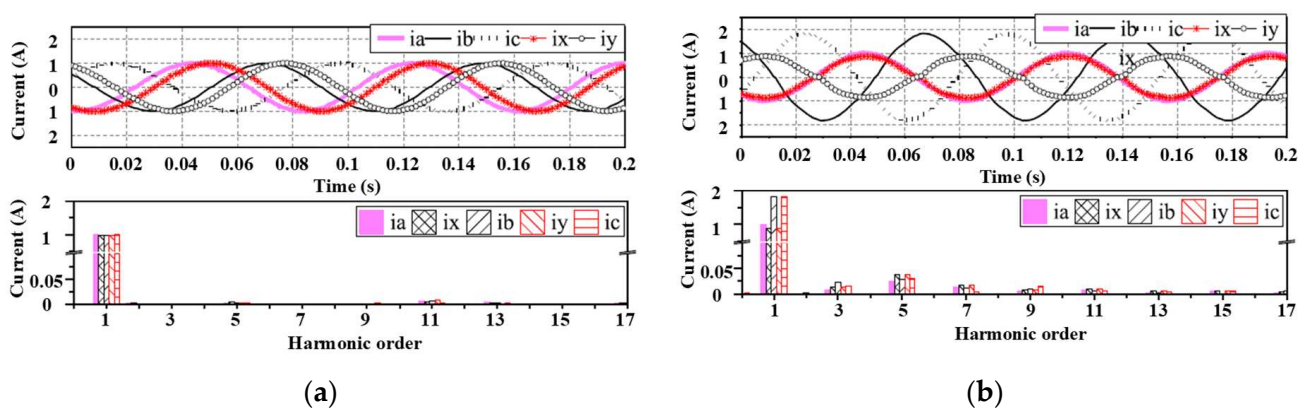


Figure 38. Measured currents and spectra (a) under healthy conditions and (b) under fault conditions [185].

The phase currents are balanced under healthy conditions, and there are few current harmonics according to the spectrum in Figure 38a. When it is converted to a faulty condition, it is clear that the two phase currents of the fault set are out of phase, and the currents of the healthy set become unbalanced, which is due to the injected negative-sequence current, as mentioned above. In addition, there are also clear odd current harmonics under faulty condition efficient suppression is lacking.

The type with connected neutral points features more degrees of freedom because all the healthy phases are available. In this case, the currents of phases  $B_2$  and  $C_2$  can be flexibly regulated to follow different references, which means they can generate the rotating flux field and thus provide average torque. However, the post-fault control algorithm is different from the normal algorithm used in the healthy case and should be specifically designed for this purpose; the issue becomes how to design the optimal current reference for each healthy phase. The optimization objectives include maximal average torque, minimal torque ripple, minimal copper loss, and uniform distribution of copper loss [170–176]. The current harmonics may be injected to boost the average torque and to reduce the torque ripple of DTP PMSM under open-fault conditions, as in [174]. To automatically track the condition of an MTPA operation, the injection-based MTPA control in three-phase machine drive is extended to the fault tolerance control of five-phase PMSM systems under single- and double-phase fault in [175]. It should be noted that these optimal current control approaches emphasize designing the current reference, and various current regulators, as studied in FOC, DTC, and MPC, and can be utilized to track the designed current references.

To avoid fault detection and algorithm switching between normal control and fault tolerance control, the robust control attracts the attention of researchers due to its good disturbance rejection capability. The loss of phases can be considered as a disturbance of machine parameter variation. If this disturbance can be easily rejected by the controller, the system can dynamically respond to the fault, and consequently the machine can still be operated without fault detection or algorithm transition. A robust speed regulator is used in [177] to provide average torque under both normal and post-fault conditions. Fuzzy logic is employed to design the current regulator of a nine-phase PMSM system in [186], as shown in Figure 39. The speed PI regulator determines the references, to which the fuzzy logic controller can achieve fundamental current tracking even before and after a fault occurs. This means that the amplitudes and phase angles of the currents in the healthy phases are automatically adjusted to provide the required torque and to cover the fault. In addition, PI regulators are used to suppress the current harmonics in the harmonic subspaces, such as the 3rd, 5th, and 7th. Furthermore, fault-tolerant controls in DTP machines fed by multi-level inverters are also investigated by considering both open-circuit switch faults and phase faults in [98,187–189], which provide greater reliability and fault capability.

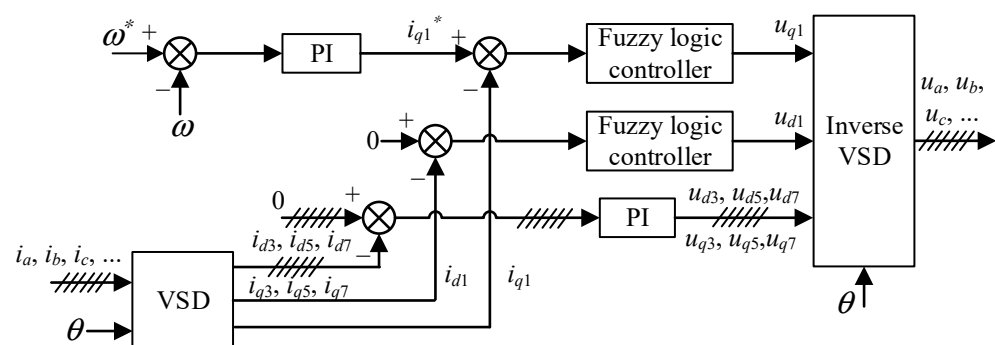


Figure 39. Fault tolerant control with fuzzy logic current regulator [186].

## 10. Conclusions and Future Work

### 10.1. Conclusions

Due to their excellent characteristics, such as their high torque/power capability, high efficiency, and low torque ripple, the low requirements of their DC link capacitors, their efficient power/torque-sharing capability, modular configuration, and high fault tolerance capability, multiphase (particularly MTP) PMSMs have been applied to ship propulsion, electric vehicles, wind power generation, and aerospace application. They

offer significant potential for even wider adoption in many high-power and high-fault-tolerance applications.

This paper presented a comprehensive overview of the advances in multiphase PMSMs' machine topologies, modelling methods, PWM techniques, field-oriented control, direct torque control, model predictive control, sensorless control, fault-tolerant control, and the newest control strategies for suppressing current harmonics and torque ripples, as well as carrier phase shift techniques. Many worked examples, presented with the measured results obtained at the University of Sheffield, were provided to illustrate the effectiveness of the developed machines and techniques, as well as their excellent performance. The emphasis was on DTP PMSMs and their control strategies, since the authors strongly believe they are most likely to be widely applied in many industries.

Firstly, the topologies of different DTP PMSMs were summarized according to their slot/pole number, angle displacement, and pitch number combinations. The feasibility of different winding configurations and the calculation of winding factors with different winding configurations were also provided in Section 2. The electromagnetic performance of DTP PMSMs was further introduced in Section 4, based on a 24 slot/22 pole machine considering different angle displacements. It is suggested that even for the dual three-phase PMSMs with the same slot/pole number and pitch number combinations, their performances are affected significantly by angle displacement. Next, aspects of MTP/DTP modelling methods were reviewed in Section 3, including multiple individual three-phase modelling with simple structure and implemental simplicity but with coupling in each set of three phase windings, and VSD modelling with decoupling results using decoupling transformation matrices. Subsequently, recent advances in control strategies, including FOC, DTC and MPC, were also covered in Section 5. Particularly, current harmonics reduction in DTP drives was on the main focus as it is a significant topic in the study of both FOC and DTC, since DTP machines suffer from large low-order current harmonics due to their inherent low impedance for the 5th and 7th harmonics. Besides, torque enhancement in FOC and torque ripple reduction in DTC have also received significant attention in recent years.

Moreover, PWM strategies for DTP were reviewed in Section 6, followed by some novel aspects of sensorless control, which are successfully adapted from the conventional three-phase sensorless methods. They include: back-EMF/ flux linkage-based methods, which offer simple implementation and accuracy in high-speed regions but also demonstrate inaccuracy under low- and zero-speed conditions due to the model's uncertainty and the inverter's nonlinearity; and the method of injecting high frequency (HF) signals, which is complicated but suitable for low-speed and zero-speed ranges. Finally, one of the most significant merits of MTP/DTP machines, their high fault tolerance capability, was surveyed through the fault-tolerant control discussions in Section 8. The modelling, optimal current references, and control methods in post-fault operation were studied, especially in open-circuit faulty conditions.

### 10.2. Future Work

Recent and future research activities include the development of modular MTP PMSMs [48–50], and high-phase MTP (such as 9, 12, and 15 phases) PMSMs for high fault tolerance applications [33,34,36], field modulation and magnetic gearing effects in MTP PMSMs [190], advanced control techniques for MTP (>DTP) PMSMs, novel parameter identifications, sensorless control, and fault tolerance control techniques.

**Author Contributions:** Conceptualization, Z.Z.; methodology and validation, S.W., B.S., L.Y., P.X. and Y.R.; formal analysis and investigation, Z.Z., S.W., B.S., L.Y., P.X. and Y.R.; resources, Z.Z.; writing—original draft preparation, Z.Z., S.W., B.S. and L.Y.; writing—review and editing, Z.Z., S.W., B.S. and L.Y.; supervision, Z.Z.; project administration, Z.Z.; funding acquisition, Z.Z. All authors have read and agreed to the published version of the manuscript.

**Funding:** This research was funded by the UK EPSRC Prosperity Partnership “A New Partnership in Offshore Wind” under Grant No. EP/R004900/1; Sheffield-Siemens Gamesa Renewable Energy Research Centre, Siemens Gamesa Renewable Energy Ltd., Sheffield, UK; GMCC & Welling Shanghai Research Centre, Midea Group, Shanghai, China; CRRC Zhuzhou Institute Co., Ltd., Zhuzhou, China; Dynex Semiconductor Ltd., Lincoln, UK; Zhuzhou CRRC Times Electric UK Innovation Center, Birmingham, UK; Protean Electric Ltd., Farnham, UK; IMRA Europe S. A. S. UK Research Center, Brighton, UK; Offshore Renewable Energy Catapult “Sheffield Power Train Research Hub” etc.

**Institutional Review Board Statement:** Not applicable.

**Informed Consent Statement:** Not applicable.

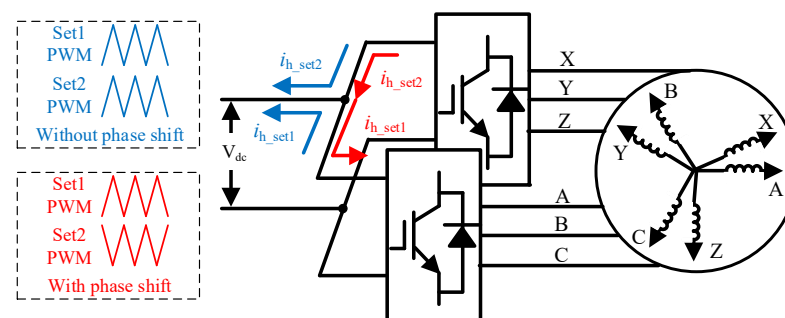
**Data Availability Statement:** Not applicable.

**Acknowledgments:** The authors acknowledge the contributions to this research field made by current and former PhD students at the University of Sheffield, including T.Y. Liu, J. Xu, Y.X. Li, L.R. Huang, Y.S. Hu, A. Almarhoon, and K.D. Hoang.

**Conflicts of Interest:** The authors declare no conflict of interest.

## Appendix A

The additional degrees of freedom also include the nonidentical PWM carriers. In the control system of MTP PMSMs, the drive topology with multiple individual three-phase converters provides the convenience and flexibility for various PWM carrier designs. Carrier phase-shift techniques, also known as the interleaving in Figure A1, is proposed to reduce the common-mode voltage [119,191], and are recently employed in this multi-converter case to reduce the current harmonics, torque ripples, vibration and acoustic noise, as well as the DC link pulsating currents [192–201]. The performance of the carrier phase-shift techniques is up to the machine winding structure, the converter topology, and the shifted angle of carriers.



**Figure A1.** Switching current harmonics of DTP PMSM driven by two paralleled three-phase inverters with and without PWM carrier phase shift.

For the DTP machine fed by two segment three-phase inverter, as studied in [192,193], the vibration and acoustic noise of switching frequency can be reduced to half after shifting  $\pi/2$  phase angle of the PWM carrier of the second set. The switching flux generated by the second set is shifted  $\pi$  in the airgap, and can counterbalance the one of the first set, which results in the reduction of switching torque ripples and vibration. Nevertheless, due to the cancellation of air gap flux, the equivalent impedance to the switching voltage harmonics is reduced simultaneously, and further switching current harmonics are increased considerably. By appropriate machine design to minimize the mutual inductance among sets [194], the switching current harmonics can be suppressed in the carrier phase shift operation.

A DTP PMSM with each phase fed by an H-bridge is studied in [195,196]. The phase axes of the first set are coincident with the ones of the second set. This winding design, combined with anti-phase shifting of carrier in the second set, determines the elimination of switching torque ripples, as shown in Figure A2. However, suffering from the same problem as [192], the coincident axes of two set means more magnetized couple, and the

equivalent impedance regarding switching voltage harmonics is greatly reduced by the anti-phase shifting of carrier. Consequently, the circulating current is serious, and [195,196] connect additionally coupled inductor between inverter and machine to limit the circulating current, which has the disadvantages of increasing system cost, volume, and complexity. The carrier phase shift is extended to a twelve-phase (quadruple-three-phase) PMSM, of which each phase is fed by an H-bridge single phase inverter [197]. A general and analytical framework as well as the mechanism of carrier phase shift are carried out based on the evaluation of radial electromagnetic forces on stator tooth faces near the airgap. To eliminate the torque ripple and vibration of multiple times the switching frequency ( $f_s, 2f_s, 3f_s, \dots$ ), [198] proposed a selective torque ripple elimination using carrier phase shift. The shifted phase can be selected from  $-\pi/2, \pi/2$ , and  $\pi$  in terms of different spatial phase displacement between two winding sets.

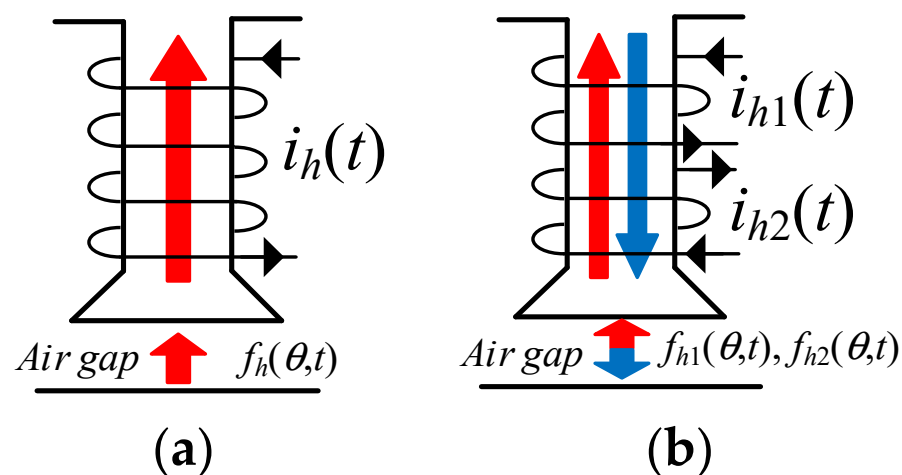


Figure A2. MMF generated by switching current harmonics. (a) Single three-phase. (b) DTP.

## References

1. Singh, G.K. Multi-phase induction machine drive research—A survey. *Electr. Power Syst. Res.* **2002**, *61*, 139–147. [\[CrossRef\]](#)
2. Jones, M.; Levi, E. A literature survey of state-of-the-art in multiphase AC drives. In Proceedings of the International Universities Power Engineering Conference (UPEC), Stafford, UK, 9–11 September 2002; pp. 505–510.
3. Bojoi, R.; Farina, F.; Profumo, F.; Tenconi, A. Dual-three phase induction machine drives control—A survey. *IEEE Trans. Ind. Appl.* **2006**, *126*, 420–429. [\[CrossRef\]](#)
4. Levi, E.; Bojoi, R.; Profumo, F.; Toloyat, H.A. Multiphase induction motor drives—A technology status review. *IET Electr. Power Appl.* **2007**, *1*, 489–516. [\[CrossRef\]](#)
5. Zhao, W.; Xu, L.; Liu, G. Overview of permanent-magnet fault-tolerant machines: Topology and design. *CES Trans. Electr. Mach. Syst.* **2018**, *2*, 51–63. [\[CrossRef\]](#)
6. Levi, E. Multiphase electric machines for variable-speed applications. *IEEE Trans. Ind. Electron.* **2008**, *55*, 1893–1909. [\[CrossRef\]](#)
7. Levi, E. Advances in converter control and innovative exploitation of additional degrees of freedom for multiphase machines. *IEEE Trans. Ind. Electron.* **2016**, *63*, 433–448. [\[CrossRef\]](#)
8. Liu, Z.; Li, Y.; Zheng, Z. A review of drive techniques for multiphase machines. *CES Trans. Electr. Mach. Syst.* **2018**, *2*, 243–251. [\[CrossRef\]](#)
9. Salem, A.; Narimani, M. A review on multiphase drives for automotive traction applications. *IEEE Trans. Transport. Electr.* **2019**, *5*, 1329–1348. [\[CrossRef\]](#)
10. Parsa, L.; Toliyat, H.A. Five-phase permanent magnet motor drives for ship propulsion applications. In Proceedings of the IEEE Electric Ship Technologies Symposium, Philadelphia, PA, USA, 27–27 July 2005; pp. 371–378.
11. Zahr, H.; Sculler, F.; Semail, E. Five-phase SPM machine with electronic pole changing effect for marine propulsion. In Proceedings of the Electrical Systems for Aircraft, Railway, Ship Propulsion and Road Vehicles & International Transportation Electrification Conference (ESARS-ITEC), Toulouse, France, 2–4 November 2016; pp. 1–6.
12. Qiao, M.; Jiang, C.; Zhu, Y.; Li, G. Research on design method and electromagnetic vibration of six-phase fractional-slot concentrated winding PM motor suitable for ship propulsion. *IEEE Access* **2016**, *4*, 8535–8543. [\[CrossRef\]](#)
13. Terrien, F.; Siala, S.; Noy, P. Multiphase induction motor sensorless control for electric ship propulsion. In Proceedings of the Power Electronics, Machines and Drives Conference (PEMD), Edinburgh, UK, 27–29 March 2004; pp. 556–561.



14. Pires, V.F.; Cordeiro, A.; Foito, D.; Silva, J.F. A three-phase onboard integrated battery charger for EVs with six-phase machine and nine switch converter. In Proceedings of the IEEE 13th International Conference on Compatibility, Power Electronics and Power Engineering (CPE-POWERENG), Sonderborg, Denmark, 23–25 April 2019; pp. 1–6.
15. Subotic, I.; Bodo, N.; Levi, E. An EV drive-train with integrated fast charging capability. *IEEE Trans. Power Electron.* **2016**, *31*, 1461–1471. [[CrossRef](#)]
16. Sousa, L.D.; Silvestre, B.; Bouchez, B. A combined multiphase electric drive and fast battery charger for electric vehicles. In Proceedings of the IEEE Vehicle Power and Propulsion Conference, Lille, France, 1–3 September 2010; pp. 1–6.
17. Subotic, I.; Bodo, N.; Levi, E.; Jones, M.; Levi, V. Isolated chargers for EVs incorporating six-phase machines. *IEEE Trans. Ind. Electron.* **2016**, *63*, 653–664. [[CrossRef](#)]
18. Bodo, N.; Levi, E.; Subotic, I.; Espina, J.; Empringham, L.; Johnson, C.M. Efficiency evaluation of fully integrated on-board EV battery chargers with nine-phase machines. *IEEE Trans. Energy Convers.* **2017**, *32*, 257–266. [[CrossRef](#)]
19. Che, H.S.; Levi, E.; Jones, M.; Duran, M.J.; Hew, W.P.; Rahim, N.A. Operation of a six-phase induction machine using series-connected machine-side converters. *IEEE Trans. Ind. Electron.* **2014**, *61*, 164–176. [[CrossRef](#)]
20. Gjerde, S.S.; Olsen, P.K.; Ljokelsoy, K.; Undeland, T.M. Control and fault handling in a modular series-connected converter for a transformerless 100 kV low-weight offshore wind turbine. *IEEE Trans. Ind. Appl.* **2014**, *50*, 1094–1105. [[CrossRef](#)]
21. Gonzalez-Prieto, I.; Duran, M.J.; Barrero, F.; Bermudez, M.; Guzman, H. Impact of post-fault flux adaptation on six-phase induction motor drives with parallel converters. *IEEE Trans. Power Electron.* **2014**, *32*, 515–528. [[CrossRef](#)]
22. Duran, M.J.; Gonzalez-Prieto, I.; Bermudez, M.; Barrero, F.; Guzman, H.; Arahall, M.R. Optimal fault-tolerant control of six-phase induction motor drives with parallel converters. *IEEE Trans. Ind. Electron.* **2016**, *63*, 629–640. [[CrossRef](#)]
23. Gonzalez-Prieto, I.; Duran, M.J.; Che, H.S.; Levi, E.; Barrero, F. Fault-tolerant operation of six-phase energy conversion systems with parallel machine-side converters. *IEEE Trans. Power Electron.* **2016**, *31*, 3068–3079. [[CrossRef](#)]
24. De Lillo, L.; Empringham, L.; Wheeler, P.W.; Khwan-On, S.; Grada, C.; Othman, M.N.; Huang, X. Multiphase power converter drive for fault-tolerant machine development in aerospace applications. *IEEE Trans. Ind. Electron.* **2010**, *57*, 575–583. [[CrossRef](#)]
25. Bojoi, R.; Cavagnino, A.; Tenconi, A.; Vaschetto, S. Control of shaft-line-embedded multiphase starter/generator for aero-engine. *IEEE Trans. Ind. Electron.* **2016**, *63*, 641–652. [[CrossRef](#)]
26. Thomas, A.S.; Zhu, Z.Q.; Owen, R.L.; Jewell, G.W.; Howe, D. Multiphase flux-switching permanent-magnet brushless machine for aerospace application. *IEEE Trans. Ind. Appl.* **2009**, *45*, 1971–1981. [[CrossRef](#)]
27. Barcaro, M.; Bianchi, N.; Magnussen, F. Analysis and tests of a dual three-phase 12-slot 10-pole permanent-magnet motor. *IEEE Trans. Ind. Appl.* **2010**, *46*, 2355–2362. [[CrossRef](#)]
28. Barcaro, M.; Bianchi, N.; Magnussen, F. Six-phase supply feasibility using a PM fractional-slot dual winding machine. *IEEE Trans. Ind. Appl.* **2011**, *47*, 2042–2050. [[CrossRef](#)]
29. Abdel-Khalik, A.S.; Ahmed, S.; Massoud, A.M. Low space harmonics cancelation in double-layer fractional slot winding using dual multiphase winding. *IEEE Trans. Magn.* **2015**, *51*, 1–10. [[CrossRef](#)]
30. Abdel-Khalik, A.S.; Ahmed, S.; Massoud, A.M. A six-phase 24-slot/10-pole permanent-magnet machine with low space harmonics for electric vehicle applications. *IEEE Trans. Magn.* **2016**, *52*, 1–10. [[CrossRef](#)]
31. Patel, V.I.; Wang, J.; Wang, W.; Chen, X. Analysis and design of 6-phase fractional slot per pole per phase permanent magnet machines with low space harmonics. In Proceedings of the International Electric Machines & Drives Conference (IEMDC), Chicago, IL, USA, 12–15 May 2013; pp. 386–393.
32. Patel, V.I.; Wang, J.; Wang, W.; Chen, X. Six-phase fractional-slot-per-pole-per-phase permanent-magnet machines with low space harmonics for electric vehicle application. *IEEE Trans. Ind. Appl.* **2014**, *50*, 2554–2563. [[CrossRef](#)]
33. Chen, X.; Wang, J.; Patel, V.I. A generic approach to reduction of magnetomotive force harmonics in permanent-magnet machines with concentrated multiple three-phase windings. *IEEE Trans. Magn.* **2014**, *50*, 1–4. [[CrossRef](#)]
34. Chen, X.; Wang, J.; Patel, V.I.; Lazari, P. A nine-phase 18-slot 14-pole interior permanent-magnet machine with low space harmonics for electric vehicle applications. *IEEE Trans. Energy Convers.* **2016**, *31*, 860–871. [[CrossRef](#)]
35. Onsal, M.; Demir, Y.; Aydin, M. A new nine-phase permanent magnet synchronous motor with consequent pole rotor for high-power traction applications. *IEEE Trans. Magn.* **2017**, *53*, 1–6. [[CrossRef](#)]
36. Shao, L.; Hua, W.; Dai, N.; Tong, M.; Cheng, M. Mathematical modeling of a 12-phase flux-switching permanent-magnet machine for wind power generation. *IEEE Trans. Ind. Electron.* **2016**, *63*, 504–516. [[CrossRef](#)]
37. Mecriw, B.C.; Jack, A.G.; Atkinson, D.J.; Green, S.R.; Atkinson, G.J.; King, A.; Green, B. Design and testing of a four-phase fault-tolerant permanent-magnet machine for an engine fuel pump. *IEEE Trans. Energy Convers.* **2004**, *19*, 671–678. [[CrossRef](#)]
38. Toliyat, H.A. Analysis and simulation of five-phase variable-speed induction motor drives under asymmetrical connections. *IEEE Trans. Power Electron.* **1998**, *13*, 748–756. [[CrossRef](#)]
39. Parsa, L.; Toliyat, H.A. Five-phase permanent-magnet motor drives. *IEEE Trans. Ind. Appl.* **2005**, *41*, 30–37. [[CrossRef](#)]
40. Sculler, F. Design of a 7-phase surface-mounted pm machine with tooth-concentrated winding. In Proceedings of the International Conference on Electrical Machines (ICEM), Alexandroupoli, Greece, 3–6 September 2018; pp. 2458–2464.
41. Sculler, F.; Becker, F.; Zahr, H.; Semail, E. Design of a bi-harmonic 7-phase pm machine with tooth-concentrated winding. *IEEE Trans. Energy Convers.* **2020**, *35*, 1567–1576. [[CrossRef](#)]
42. Abdelkhalik, A.; Masoud, M.; Williams, B.W. Eleven-phase induction machine: Steady-state analysis and performance evaluation with harmonic injection. *IET Elect. Power Appl.* **2010**, *4*, 670–685. [[CrossRef](#)]

43. Cheng, L.; Sui, Y.; Zheng, P.; Yin, Z.; Wang, C. Investigation of low space harmonic six-phase PMSM with FSCWs for electric vehicle applications. In Proceedings of the IEEE Transportation Electrification Conference and Expo, Asia-Pacific (ITEC Asia-Pacific), Harbin, China, 7–10 August 2017; pp. 1–5.
44. Cheng, L.; Sui, Y.; Zheng, P.; Yin, Z.; Wang, C. Influence of stator MMF harmonics on the utilization of reluctance torque in six-phase PMA-SynRM with FSCW. *Energies* **2018**, *11*, 108. [[CrossRef](#)]
45. Zhu, S.; Cox, T.; Xu, Z.; Gerada, C. A novel 24-slots/14-poles fractional-slot concentrated winding topology with low space harmonics for electrical machine. In Proceedings of the Power Electronics, Machines and Drives Conference (PEMD), Liverpool, UK, 17–19 April 2018.
46. Xu, P.L.; Feng, J.; Guo, S.; Feng, S.; Chu, W.Q.; Ren, Y.; Zhu, Z.Q. Analysis of dual three-phase permanent magnet synchronous machines with different angle displacements. *IEEE Trans. Ind. Electron.* **2018**, *65*, 1941–1954. [[CrossRef](#)]
47. Xu, P.L.; Zhu, Z.Q.; Shao, B.; Wang, S.S.; Feng, J.H.; Guo, S.Y.; Li, Y.F.; Feng, S.Z. Analysis of dual 3-phase fractional-slot non-overlapping winding pm synchronous machines with different angle displacements. In Proceedings of the IEEE Energy Conversion Congress and Exposition (ECCE 2019), Baltimore, MD, USA, 29 September–3 October 2019; pp. 5616–5623.
48. Li, Y.X.; Zhu, Z.Q.; Thomas, A.; Wu, Y.; Wu, X.M. Comparison of modular dual 3-phase PM machines with overlapping/non-overlapping windings. *IEEE Trans. Ind. Appl.* **2019**, *55*, 3566–3576. [[CrossRef](#)]
49. Li, Y.X.; Zhu, Z.Q.; Thomas, A.S.; Wu, Z.Y.; Wu, X.M. Novel modular fractional slot permanent magnet machines with redundant teeth. *IEEE Trans. Magn.* **2019**, *55*, 1–10. [[CrossRef](#)]
50. Li, Y.X.; Zhu, Z.Q.; Thomas, A.S. Generic slot and pole number combinations for novel modular permanent magnet dual 3-phase machines with redundant teeth. *IEEE Trans. Energy Convers.* **2020**, *35*, 1676–1687. [[CrossRef](#)]
51. Zheng, P.; Wu, F.; Lei, Y.; Sui, Y.; Yu, B. Investigation of a novel 24-slot/14-pole six-phase fault-tolerant modular permanent-magnet in-wheel motor for electric vehicles. *Energies* **2013**, *6*, 4980–5002. [[CrossRef](#)]
52. Abdel-Khalik, A.S.; Masoud, M.I.; Williams, B.W. Improved flux pattern with third harmonic injection for multiphase induction machines. *IEEE Trans. Power Electron.* **2012**, *27*, 1563–1578. [[CrossRef](#)]
53. Zhu, Z.Q.; Howe, D. Electrical machines and drives for electric, hybrid and fuel cell vehicles. *Proc. IEEE* **2007**, *95*, 746–765. [[CrossRef](#)]
54. Karttunen, J.; Kallio, S.; Peltoniemi, P.; Silventoinen, P.; Pyrhonen, O. Dual three-phase permanent magnet synchronous machine supplied by two independent voltage source inverters. In Proceedings of the International Symposium on Power Electronics, Electrical Drives, Automation and Motion, Sorrento, Italy, 20–22 June 2012; pp. 741–747.
55. Singh, G.K.; Nam, K.; Lim, S.K. A simple indirect field-oriented control scheme for multiphase induction machine. *IEEE Trans. Ind. Electron.* **2005**, *52*, 1177–1184. [[CrossRef](#)]
56. Bojoi, R.; Lazzari, M.; Profumo, F.; Tenconi, A. Digital field-oriented control for dual three-phase induction motor drives. *IEEE Trans. Ind. Appl.* **2003**, *39*, 752–760. [[CrossRef](#)]
57. He, Y.; Wang, Y.; Wu, J.; Feng, Y.; Liu, J. A simple current sharing scheme for dual three-phase permanent-magnet synchronous motor drives. In Proceedings of the Annual IEEE Conference on Applied Power Electronics Conference and Exposition (APEC), Palm Springs, CA, USA, 21–25 February 2010; pp. 1093–1096.
58. Hu, Y.; Zhu, Z.Q.; Odavic, M. Comparison of two-individual current control and vector space decomposition control for dual three-phase PMSM. *IEEE Trans. Ind. Appl.* **2017**, *53*, 4483–4492. [[CrossRef](#)]
59. Hu, S.; Liang, Z.; Zhang, W.; He, X. Research on the integration of hybrid energy storage system and dual three-phase PMSM drive in EV. *IEEE Trans. Ind. Electron.* **2018**, *65*, 6602–6611. [[CrossRef](#)]
60. Tassarolo, A.; Bortolozzi, M.; Contin, A. Modeling of split-phase machines in Park's coordinates. Part I: Theoretical foundations. In Proceedings of the IEEE Euro Conference, Zagreb, Croatia, 1–4 July 2013; pp. 1308–1313.
61. Tassarolo, A.; Bortolozzi, M.; Contin, A. Modeling of split-phase machines in Park's coordinates. Part II: Equivalent circuit representation. In Proceedings of the IEEE Euro Conference, Zagreb, Croatia, 1–4 July 2013; pp. 1314–1319.
62. Zhao, Y.; Lipo, T.A. Space vector PWM control of dual three-phase induction machine using vector space decomposition. *IEEE Trans. Ind. Appl.* **1995**, *31*, 1100–1109. [[CrossRef](#)]
63. Zabaleta, M.; Levi, E.; Jones, M. Modelling approaches for triple three-phase permanent magnet machines. In Proceedings of the International Conference on Electrical Machines (ICEM), Lausanne, Switzerland, 4–7 September 2016; pp. 466–472.
64. Zoric, I.; Jones, M.; Levi, E. Vector space decomposition algorithm for asymmetrical multiphase machines. In Proceedings of the International Symposium on Power Electronics, Novi Sad, Serbia, 19–21 October 2017; pp. 1–6.
65. Tani, A.; Serra, G.; Mengoni, M.; Zarri, L.; Rini, G.; Casadei, D. Dynamic stator current sharing in quadruple three-phase induction motor drives. In Proceedings of the 39th Annual Conference of the IEEE Industrial Electronics Society (IECON), Vienna, Austria, 10–13 November 2013; pp. 5173–5178.
66. Rockhill, A.; Lipo, T.A. A simplified model of a nine-phase synchronous machine using vector space decomposition. In Proceedings of the IEEE Power Electronics and Machines in Wind Applications (PEMWA), Lincoln, NE, USA, 24–26 June 2009; pp. 1–5.
67. Moinoddin, S.; Abu-Rub, H.; Iqbal, A.; Alammari, R. Modelling and implementation of SVPWM technique for a fifteen-phase voltage source inverter for sinusoidal output waveform. In Proceedings of the IEEE International Conference on Industrial Technology (ICIT), Seville, Spain, 17–19 March 2015; pp. 1075–1080.
68. Hu, Y.; Zhu, Z.Q.; Liu, K. Current control for dual three-phase permanent magnet synchronous motors accounting for current unbalance and harmonics. *IEEE J. Emerg. Sel. Topics Power Electron.* **2014**, *2*, 272–284.

69. Karttunen, J.; Kallio, S.; Peltoniemi, P.; Silventoinen, P.; Pyrhönen, O. Decoupled vector control scheme for dual three-phase permanent magnet synchronous machines. *IEEE Trans. Ind. Electron.* **2014**, *61*, 2185–2196. [[CrossRef](#)]
70. Karttunen, J.; Kallio, S.; Honkanen, J.; Peltoniemi, P.; Silventoinen, P. Partial current harmonic compensation in dual three-phase PMSMs considering the limited available voltage. *IEEE Trans. Ind. Electron.* **2017**, *64*, 1038–1048. [[CrossRef](#)]
71. Jones, M.; Vukosavic, S.N.; Dujic, D.; Levi, E. A synchronous current control scheme for multiphase induction motor drives. *IEEE Trans. Energy Convers.* **2009**, *24*, 860–868. [[CrossRef](#)]
72. Bojoi, R.; Levi, E.; Farina, F.; Tenconi, A.; Profumo, F. DTP induction motor drive with digital current control in the stationary reference frame. *Power Eng.* **2006**, *153*, 129–139.
73. Che, H.; Levi, E.; Jones, M.; Hew, W.; Rahim, N. Current control methods for an asymmetrical six-phase induction motor drive. *IEEE Trans. Power Electron.* **2014**, *29*, 407–417. [[CrossRef](#)]
74. Yepes, A.; Malvar, J.; Vidal, A.; Lopez, O.; Doval-Gandoy, J. Current harmonic compensation based on multi-resonant control in synchronous frames for symmetrical n-phase machines. *IEEE Trans. Ind. Electron.* **2014**, *29*, 407–417.
75. Ruan, Z.; Song, W.; Yan, Y. Current harmonic suppression for dual three-phase permanent magnet synchronous motor drives. *IEEE Access* **2019**, *7*, 143888–143898. [[CrossRef](#)]
76. Karttunen, J.; Kallio, S.; Peltoniemi, P.; Silventoinen, P. Current harmonic compensation in dual three-phase PMSMs using a disturbance observer. *IEEE Trans. Ind. Electron.* **2016**, *63*, 583–594. [[CrossRef](#)]
77. Xu, Y.; Zheng, B.; Wang, G.; Yan, H.; Zou, J. Current harmonic suppression in dual three-phase permanent magnet synchronous machine with extended state observer. *IEEE Trans. Power Electron.* **2020**, *35*, 12166–12180. [[CrossRef](#)]
78. Yan, L.C.; Zhu, Z.Q.; Qi, J.; Ren, Y.; Gan, C.; Brockway, S.; Hilton, C. Enhancement of disturbance rejection capability in dual three-phase PMSM system by using virtual impedance. *IEEE Trans. Ind. Appl.* **2021**, *57*, 4901–4912. [[CrossRef](#)]
79. Xu, J.; Odavic, M.; Zhu, Z.Q.; Wu, Z.Y.; Freire, N.M.A. A generalized decomposition model of dual three-phase permanent magnet synchronous machines considering asymmetric impedances and compensation capability. *IEEE Trans. Ind. Appl.* **2021**, *57*, 3763–3775. [[CrossRef](#)]
80. Yan, L.C.; Zhu, Z.Q.; Qi, J.; Ren, Y.; Gan, C.; Brockway, S.; Hilton, C. Multiple synchronous reference frame current harmonic regulation of dual three phase PMSM with enhanced dynamic performance and system stability. *IEEE Trans. Ind. Electron.* **2021**, in press. [[CrossRef](#)]
81. Yan, L.C.; Zhu, Z.Q.; Qi, J.; Ren, Y.; Gan, C.; Brockway, S.; Hilton, C. Suppression of major current harmonics for dual three phase PMSMs by virtual multi three phase systems. *IEEE Trans. Ind. Electron.* **2021**, in press. [[CrossRef](#)]
82. Lyra, R.O.C.; Lipo, T.A. Torque density improvement in a six-phase induction motor with third harmonic current injection. *IEEE Trans. Ind. Appl.* **2002**, *38*, 1351–1360. [[CrossRef](#)]
83. Wang, K.; Zhu, Z.Q.; Ren, Y.; Ombach, G. Torque improvement of dual three-phase permanent-magnet machine with third-harmonic current injection. *IEEE Trans. Ind. Electron.* **2015**, *62*, 6833–6844. [[CrossRef](#)]
84. Hu, Y.; Zhu, Z.Q.; Odavic, M. Torque capability enhancement of dual three-phase PMSM drive with fifth and seventh current harmonics injection. *IEEE Trans. Ind. Appl.* **2017**, *53*, 4526–4535. [[CrossRef](#)]
85. Bojoi, R.; Farina, F.; Griva, G.; Profumo, F.; Tenconi, A. Direct torque control for dual three-phase induction motor drives. *IEEE Trans. Ind. Appl.* **2005**, *41*, 1627–1636. [[CrossRef](#)]
86. Hatua, K.; Ranganathan, V. Direct torque control schemes for split-phase induction machine. *IEEE Trans. Ind. Appl.* **2005**, *41*, 1243–1254. [[CrossRef](#)]
87. Ren, Y.; Zhu, Z.Q. Enhancement of steady-state performance in direct torque controlled dual-three phase permanent magnet synchronous machine drives with modified switching table. *IEEE Trans. Ind. Electron.* **2015**, *62*, 3338–3350. [[CrossRef](#)]
88. Hoang, K.; Ren, Y.; Zhu, Z.Q.; Forster, M. Modified switching-table strategy for reduction of current harmonics in direct torque controlled dual-three-phase permanent magnet synchronous machine drives. *IET Elect. Power Appl.* **2015**, *9*, 10–19. [[CrossRef](#)]
89. Pandit, J.K.; Aware, M.V.; Nemade, R.; Tatte, Y. Simplified implementation of synthetic vectors for DTC of asymmetric six-phase induction motor drives. *IEEE Trans. Ind. Appl.* **2018**, *54*, 2306–2318. [[CrossRef](#)]
90. Shao, B.; Zhu, Z.Q.; Feng, J.; Guo, S.; Li, Y.; Liao, W. Compensation of selective current harmonics for switching-table-based direct torque control of dual three-phase PMSM drives. *IEEE Trans. Ind. Appl.* **2021**, *57*, 2505–2515. [[CrossRef](#)]
91. Shao, B.; Zhu, Z.Q.; Feng, J.; Guo, S.; Li, Y.; Feng, L.; Bo, S. Improved direct torque control method for dual-three-phase permanent-magnet synchronous machines with back-EMF harmonics. *IEEE Trans. Ind. Electron.* **2021**, *68*, 9319–9333. [[CrossRef](#)]
92. Ren, Y.; Zhu, Z.Q. Reduction of both harmonic current and torque ripple for dual three-phase permanent-magnet synchronous machine using modified switching-table-based direct torque control. *IEEE Trans. Ind. Electron.* **2015**, *62*, 6671–6683. [[CrossRef](#)]
93. Taheri, A.; Rahmati, A.; Kaboli, S. Efficiency improvement in DTC of six-phase induction machine by adaptive gradient descent of flux. *IEEE Trans. Power Electron.* **2012**, *27*, 1552–1562. [[CrossRef](#)]
94. Holakooie, M.H.; Ojaghi, M.; Taheri, A. Direct torque control of six-phase induction motor with a novel MRAS-based stator resistance estimator. *IEEE Trans. Power Electron.* **2012**, *27*, 1552–1562. [[CrossRef](#)]
95. Holakooie, M.H.; Ojaghi, M.; Taheri, A. Modified DTC of a six-phase induction motor with a second-order sliding-mode MRAS-based speed estimator. *IEEE Trans. Power Electron.* **2019**, *34*, 600–611. [[CrossRef](#)]
96. Ren, Y.; Zhu, Z.Q.; Green, J.E.; Li, Y.; Zhu, S.; Li, Z. Duty-ratio-based direct torque control for dual three-phase permanent magnet synchronous machine drives. *IEEE Energy Convers. Congr. Expo* **2018**, 3367–3374.
97. Ren, Y.; Zhu, Z.Q.; Green, J.E.; Li, Y.; Zhu, S.; Li, Z. Improved duty-ratio-based direct torque control for dual three-phase permanent magnet synchronous machine drives. *IEEE Trans. Ind. Appl.* **2019**, *55*, 5843–5853. [[CrossRef](#)]

98. Wang, X.; Wang, Z.; Cheng, M.; Hu, Y. Remedial strategies of T-NPC three-level asymmetric six-phase PMSM drives based on SVM-DTC. *IEEE Trans. Ind. Electron.* **2017**, *64*, 6841–6853. [[CrossRef](#)]
99. Wang, X.; Wang, Z.; Xu, Z. A hybrid direct torque control scheme for dual three-phase PMSM drives with improved operation performance. *IEEE Trans. Power Electron.* **2019**, *34*, 1622–1634. [[CrossRef](#)]
100. Xu, J.; Odavic, M.; Zhu, Z.Q.; Wu, Z.Y.; Freire, N. Switching-table-based direct torque control of dual three-phase PMSMs with closed-loop current harmonics compensation. *IEEE Trans. Power Electron.* **2021**, *36*, 10645–10659. [[CrossRef](#)]
101. Barrero, F.; Arahall, M.; Gregor, R.; Toral, S.; Duran, M. A proof of concept study of predictive current control for VSI-driven asymmetrical dual three-phase AC machines. *IEEE Trans. Ind. Electron.* **2009**, *56*, 1937–1954. [[CrossRef](#)]
102. Barrero, F.; Arahall, M.; Gregor, R.; Toral, S.; Duran, M. One-step modulation predictive current control method for the asymmetrical dual three-phase induction machine. *IEEE Trans. Ind. Electron.* **2009**, *56*, 1974–1983. [[CrossRef](#)]
103. Duran, M.; Prieto, J.; Barrero, F.; Toral, S. Predictive current control of dual three-phase drives using restrained search techniques. *IEEE Trans. Ind. Electron.* **2011**, *58*, 3253–3263. [[CrossRef](#)]
104. Barrero, F.; Prieto, J.; Levi, E.; Gregor, R.; Toral, S.; Duran, M.; Jones, M. An enhanced predictive current control method for asymmetrical six-phase motor drives. *IEEE Trans. Ind. Electron.* **2011**, *58*, 3242–3252. [[CrossRef](#)]
105. Gonzalez-Prieto, I.; Duran, M.J.; Aciego, J.J.; Martin, C.; Barrero, F. Model predictive control of six-phase induction motor drives using virtual VVs. *IEEE Trans. Ind. Electron.* **2018**, *65*, 27–37. [[CrossRef](#)]
106. Luo, Y.; Liu, C. Elimination of harmonic currents using a reference voltage vector based-model predictive control for a six-phase PMSM motor. *IEEE Trans. Power Electron.* **2019**, *34*, 6960–6972. [[CrossRef](#)]
107. Aciego, J.J.; González Prieto, I.; Duran, M.J. Model predictive control of six-phase induction motor drives using two virtual VVs. *IEEE J. Emerg. Sel. Topics Power Electron.* **2019**, *7*, 321–330. [[CrossRef](#)]
108. Goncalves, P.F.; Cruz, S.M.; Mendes, A.M. Bi-subspace predictive current control of six-phase PMSM drives based on virtual vectors with optimal amplitude. *IET Elect. Power Appl.* **2019**, *13*, 1672–1683. [[CrossRef](#)]
109. Gonçalves, P.F.C.; Cruz, S.M.A.; Mendes, A. Multistage predictive current control based on virtual vectors for the reduction of current harmonics in six-phase PMSMs. *IEEE Trans. Energy Convers.* **2021**, in press.
110. Aciego, J.J.; Gonzalez-Prieto, I.; Duran, M.J.; Bermudez, M.; Salas-Biedma, P. Model predictive control based on dynamic VVs for six-phase induction machines. *IEEE J. Emerg. Sel. Topics Power Electron.* **2021**, in press. [[CrossRef](#)]
111. Bermudez, M.; Arahall, M.R.; Duran, M.J.; Gonzalez-Prieto, I. Model predictive control of six-phase electric drives including ARX disturbance estimator. *IEEE Trans. Ind. Electron.* **2021**, *68*, 81–91. [[CrossRef](#)]
112. Gonçalves, P.F.C.; Cruz, S.M.A.; Mendes, A.M.S. Disturbance-observer-based predictive current control of six-phase PMSMs for the mitigation of steady-state errors and current harmonics. *IEEE Trans. Ind. Electron.* **2021**, in press.
113. Luo, Y.; Liu, C. A simplified model predictive control for a dual three-phase PMSM with reduced harmonic currents. *IEEE Trans. Ind. Electron.* **2018**, *65*, 9079–9089. [[CrossRef](#)]
114. Luo, Y.; Liu, C. Multi-vector-based model predictive torque control for a six-phase PMSM motor with fixed switching frequency. *IEEE Trans. Energy Convers.* **2019**, *34*, 1369–1379. [[CrossRef](#)]
115. Luo, Y.; Liu, C. Model predictive control for a six-phase PMSM with high robustness against weighting factor variation. *IEEE Trans. Ind. Appl.* **2019**, *55*, 2781–2791. [[CrossRef](#)]
116. Luo, Y.; Liu, C. Model predictive control for a six-phase PMSM motor with a reduced-dimension cost function. *IEEE Trans. Ind. Electron.* **2020**, *67*, 969–979. [[CrossRef](#)]
117. Luo, Y.; Liu, C. A flux constrained predictive control for a six-phase PMSM motor with lower complexity. *IEEE Trans. Ind. Electron.* **2019**, *66*, 5081–5093. [[CrossRef](#)]
118. Karugaba, S.; Ojo, O. A carrier-based PWM modulation technique for balanced and unbalanced reference voltages in multiphase voltage-source inverters. *IEEE Trans. Ind. Appl.* **2012**, *48*, 2102–2109. [[CrossRef](#)]
119. Liu, Z.; Zheng, Z.; Sudhoff, S.D.; Gu, C.; Li, Y. Reduction of common-mode voltage in multiphase two-level inverters using SPWM with phase shifted carriers. *IEEE Trans. Power Electron.* **2016**, *31*, 6631–6645. [[CrossRef](#)]
120. Liu, Z.; Zheng, Z.; Peng, Z.; Li, Y.; Hao, L. A sawtooth carrier-based PWM for asymmetrical six-phase inverters with improved common mode voltage performance. *IEEE Trans. Power Electron.* **2017**, *8*, 9444–9458. [[CrossRef](#)]
121. Rakesh, P.R.; Narayanan, G. Analysis of sine-triangle and zero-sequence injection modulation schemes for split-phase induction motor drive. *IET Power Electron.* **2016**, *9*, 344–355. [[CrossRef](#)]
122. Dujic, D.; Levi, E.; Jones, M. DC bus utilization in multiphase VSI supplied drives with a composite stator phase number. In Proceedings of the 2010 IEEE International Conference on Industrial Technology, Via del Mar, Chile, 14–17 March 2010; pp. 1495–1500.
123. Bojoi, R.; Tenconi, A.; Profumo, F.; Griva, G.; Martinello, D. Complete analysis and comparative study of digital modulation techniques for dual three-phase AC motor drives. *Conf. Rec. IEEE Power Electron. Spec. Conf.* **2002**, *2*, 851–857.
124. Prieto, J.; Levi, E.; Barrero, F.; Toral, S. Output current ripple analysis for asymmetrical six-phase drives using double zero-sequence injection PWM. In Proceedings of the IECON 37th Annual Conference of the IEEE Industrial Electronics Society, Melbourne, VIC, Australia, 7–10 November 2011; pp. 3692–3697.
125. Glose, D.; Kennel, R. Carrier-based pulse width modulation for symmetrical six-phase drives. *IEEE Trans. Power Electron.* **2015**, *30*, 6873–6882. [[CrossRef](#)]
126. Rakesh, P.R.; Narayanan, G. Investigation on zero-sequence signal injection for improved harmonic performance in split-phase induction motor drives. *IEEE Trans. Ind. Electron.* **2017**, *64*, 2732–2741. [[CrossRef](#)]

127. Gopakumar, K.; Ranganthan, V.; Bhat, S. Split-phase induction motor operation from PWM voltage source inverter. *IEEE Trans. Ind. Appl.* **1993**, *29*, 927–932. [[CrossRef](#)]
128. Prieto, J.; Riveros, J.A.; Bogado, B. Continuous and discontinuous SVPWM 2L+2M for asymmetrical dual three-phase drives. In Proceedings of the 2017 IEEE International Electric Machines and Drives Conference (IEMDC), Miami, FL, USA, 21–24 May 2017; pp. 1–6.
129. Marouani, K.; Baghli, L.; Hadiouche, D.; Kheloui, A.; Rezzoug, A. A new PWM strategy based on a 24-sector vector space decomposition for a six-phase VSI-fed dual stator induction motor. *IEEE Trans. Ind. Electron.* **2008**, *55*, 1910–1920. [[CrossRef](#)]
130. Suhel, S.M.; Maurya, R. Realization of 24-sector SVPWM with new switching pattern for six-phase induction motor drive. *IEEE Trans. Power Electron.* **2019**, *34*, 5079–5092. [[CrossRef](#)]
131. Hadiouche, D.; Baghli, L.; Rezzoug, A. Space-vector PWM techniques for dual three-phase AC machine: Analysis, performance evaluation, and DSP implementation. *IEEE Trans. Ind. Appl.* **2006**, *42*, 1112–1122. [[CrossRef](#)]
132. Wang, C.; Wang, K.; You, X. Research on synchronized SVPWM strategies under low switching frequency for six-phase VSI-Fed asymmetrical dual stator induction machine. *IEEE Trans. Ind. Electron.* **2016**, *63*, 6767–6776. [[CrossRef](#)]
133. Kun, W.; Xiaojie, Y.; Chenchen, W.; Minglei, Z. An equivalent dual three-phase SVPWM realization of the modified 24-sector SVPWM strategy for asymmetrical dual stator induction machine. In Proceedings of the 2016 IEEE Energy Conversion Congress and Exposition (ECCE), Milwaukee, WI, USA, 18–22 September 2016; pp. 1–7.
134. Xu, J.; Odavic, M.; Zhu, Z.Q.; Wu, Z.Y.; Freire, N.M.A. Modulation restraint analysis of space vector PWM for dual three-phase machines under vector space decomposition. *IEEE Trans. Power Electron.* **2021**, *36*, 14491–14507. [[CrossRef](#)]
135. Maheshwari, R.; Busquets-Monge, S.; Nicolas-Apruzzese, J. A novel approach to generate effective carrier-based pulse width modulation strategies for diode-clamped multilevel dc–ac converters. *IEEE Trans. Ind. Electron.* **2016**, *63*, 7243–7252. [[CrossRef](#)]
136. López, Ó.; Álvarez, J.; Yepes, A.G.; Baneira, F.; Pérez-Estévez, D.; Freijedo, F.D.; Doval-Gandoy, J. Carrier-based PWM equivalent to multilevel multiphase space vector PWM techniques. *IEEE Trans. Ind. Electron.* **2020**, *67*, 5220–5231. [[CrossRef](#)]
137. Zhu, Y.; Gu, W.; Lu, K.; Wu, Z. Vector control of asymmetric dual three-phase PMSM in full modulation range. *IEEE Access* **2020**, *8*, 104479–104493. [[CrossRef](#)]
138. Yazdani, D.; Ali Khajehoddin, S.; Bakhshai, A.; Joos, G. Full utilization of the inverter in split-phase drives by means of a dual three-phase space vector classification algorithm. *IEEE Trans. Ind. Electron.* **2009**, *56*, 120–129. [[CrossRef](#)]
139. Zhou, C.; Yang, G.; Su, J. PWM strategy with minimum harmonic distortion for dual three-phase permanent-magnet synchronous motor drives operating in the overmodulation region. *IEEE Trans. Power Electron.* **2016**, *31*, 1367–1380. [[CrossRef](#)]
140. Paul, S.; Basu, K. Overmodulation techniques of asymmetrical six-phase machine with optimum harmonic voltage injection. *IEEE Trans. Ind. Electron.* **2021**, *68*, 4679–4690. [[CrossRef](#)]
141. Paul, S.; Basu, K. A three-phase inverter based overmodulation strategy of asymmetrical six-phase induction machine. *IEEE Trans. Power Electron.* **2021**, *36*, 5802–5817. [[CrossRef](#)]
142. Wang, G.; Valla, M.; Solsona, J. Position sensorless permanent magnet synchronous machine drives—A review. *IEEE Trans. Ind. Electron.* **2020**, *67*, 5830–5842. [[CrossRef](#)]
143. Matsui, N. Sensorless PM brushless DC motor drives. *IEEE Trans. Ind. Electron.* **1996**, *43*, 300–308. [[CrossRef](#)]
144. Chen, Z.; Tomita, M.; Doki, S.; Okuma, S. An extended electromotive force model for sensorless control of interior permanent-magnet synchronous motors. *IEEE Trans. Ind. Electron.* **2003**, *50*, 288–295. [[CrossRef](#)]
145. Genduso, F.; Miceli, R.; Rando, C.; Galluzzo, G.R. Back EMF sensorless-control algorithm for high-dynamic performance PMSM. *IEEE Trans. Ind. Electron.* **2010**, *57*, 2092–2100. [[CrossRef](#)]
146. Morimoto, S.; Kawamoto, K.; Sanada, M.; Takeda, Y. Sensorless control strategy for salient-pole PMSM based on extended EMF in rotating reference frame. *IEEE Trans. Ind. Appl.* **2002**, *38*, 1054–1061. [[CrossRef](#)]
147. Liu, J.M.; Zhu, Z.Q. Improved sensorless control of permanent-magnet synchronous machine based on third-harmonic back EMF. *IEEE Trans. Ind. Appl.* **2014**, *50*, 1861–1870. [[CrossRef](#)]
148. Kim, J.; Jeong, I.; Nam, K.; Yang, J.; Hwang, T. Sensorless control of PMSM in a high-speed region considering iron loss. *IEEE Trans. Ind. Electron.* **2015**, *62*, 6151–6159. [[CrossRef](#)]
149. Boldea, I.; Paicu, M.C.; Andreescu, G. Active flux concept for motion-sensorless unified AC drives. *IEEE Trans. Power Electron.* **2008**, *23*, 2612–2618. [[CrossRef](#)]
150. Boldea, I.; Paicu, M.C.; Andreescu, G.D.; Blaabjerg, F. Active flux DTFC-SVM sensorless control of IPMSM. *IEEE Trans. Energy Convers* **2009**, *24*, 314–322. [[CrossRef](#)]
151. Liu, K.; Zhu, Z.Q.; Stone, D.A. Parameter estimation for condition monitoring of PMSM stator winding and rotor permanent magnets. *IEEE Trans. Ind. Electron.* **2013**, *60*, 5902–5913. [[CrossRef](#)]
152. Xie, G.; Lu, K.; Dwivedi, S.K.; Riber, R.J.; Wu, W. Permanent magnet flux online estimation based on zero-voltage vector injection method. *IEEE Trans. Power Electron.* **2015**, *30*, 6506–6509. [[CrossRef](#)]
153. Yoo, A.; Sul, S.K. Design of flux observer robust to interior permanent-magnet synchronous motor flux variation. *IEEE Trans. Ind. Appl.* **2009**, *45*, 1670–1677.
154. Kim, S.I.; Im, J.H.; Song, E.Y.; Kim, R.Y. A new rotor position estimation method of IPMSM using all-pass filter on high-frequency rotating voltage signal injection. *IEEE Trans. Ind. Electron.* **2016**, *63*, 6499–6509. [[CrossRef](#)]
155. Medjmadj, S.; Diallo, D.; Mostefai, M.; Delpha, C.; Arias, A. PMSM drive position estimation: Contribution to the high-frequency injection voltage selection issue. *IEEE Trans. Energy Convers* **2015**, *30*, 349–358. [[CrossRef](#)]

156. Basic, D.; Malrait, F.; Rouchon, P. Current controller for low frequency signal injection and rotor flux position tracking at low speeds. *IEEE Trans. Ind. Electron.* **2011**, *58*, 4010–4022. [[CrossRef](#)]
157. Bianchi, N.; Bolognani, S.; Jang, J.H.; Sul, S.K. Comparison of PM motor structures and sensorless control techniques for zero-speed rotor position detection. *IEEE Trans. Power Electron.* **2007**, *22*, 2466–2475. [[CrossRef](#)]
158. Liu, J.M.; Zhu, Z.Q. Rotor position estimation for single- and dual-three-phase permanent magnet synchronous machines based on third harmonic back-EMF under imbalanced situation. *Chin. J. Electr. Eng.* **2017**, *3*, 63–72.
159. Almarhoon, A.H.; Zhu, Z.Q.; Xu, P.L. Improved pulsating signal injection using zero-sequence carrier voltage for sensorless control of dual three-phase PMSM. *IEEE Trans. Energy Convers.* **2017**, *32*, 436–446. [[CrossRef](#)]
160. Almarhoon, A.H.; Zhu, Z.Q.; Xu, P.L. Improved rotor position estimation accuracy by rotating carrier signal injection utilizing zero-sequence carrier voltage for dual three-phase PMSM. *IEEE Trans. Ind. Electron.* **2017**, *64*, 4454–4462. [[CrossRef](#)]
161. Liu, T.; Zhu, Z.Q.; Wu, Z.Y.; Stone, D.; Foster, M. A simple sensorless position error correction method for dual three-phase permanent magnet synchronous machines. *IEEE Trans. Energy Convers.* **2021**, in press. [[CrossRef](#)]
162. Barcaro, M.; Bianchi, N.; Magnussen, F. Faulty operations of a PM fractional-slot machine with a dual three-phase winding. *IEEE Trans. Ind. Electron.* **2011**, *58*, 3825–3832. [[CrossRef](#)]
163. Alberti, L.; Bianchi, N. Experimental tests of dual three-phase induction motor under faulty operating condition. *IEEE Trans. Ind. Electron.* **2012**, *59*, 2041–2048. [[CrossRef](#)]
164. Jiang, X.; Huang, W.; Cao, R.; Hao, Z.; Jiang, W. Electric drive system of dual-winding fault-tolerant permanent-magnet motor for aerospace applications. *IEEE Trans. Ind. Electron.* **2015**, *62*, 7322–7330. [[CrossRef](#)]
165. Wang, Z.; Wang, X.; Wang, Y.; Chen, J.; Cheng, M. Fault tolerant control of multiphase multilevel motor drives—Technical review. *Chin. J. Electr. Eng.* **2017**, *3*, 76–86.
166. Feng, G.; Lai, C.; Li, W.; Tjong, J.; Kar, N.C. Open-phase fault modeling and optimized fault-tolerant control of dual three-phase permanent magnet synchronous machines. *IEEE Trans. Power Electron.* **2019**, *34*, 11116–11127. [[CrossRef](#)]
167. Cao, W.P.; Mecrow, B.C.; Atkinson, G.J.; Bennett, J.W.; Atkinson, D.J. Overview of electric motor technologies used for more electric aircraft (MEA). *IEEE Trans. Ind. Electron.* **2012**, *59*, 3523–3531.
168. Mantero, S.; De Paola, E.; Marina, G. An optimised control strategy for double star motors configuration in redundancy operation mode. In Proceedings of the European Power Electronics Conference, Lausanne, Switzerland, 7–9 September 1999.
169. Mantero, S.; Monti, A.; Spreafico, S. DC-bus voltage control for double star asynchronous fed drive under fault conditions. In Proceedings of the IEEE 2000 Power Electronics Specialist Conference, Galway, Ireland, 18–23 June 2000.
170. Yu, F.; Cheng, M.; Chau, K.T. Controllability and performance of a nine-phase FSPM motor under severe five open-phase fault conditions. *IEEE Trans. Energy Convers.* **2016**, *31*, 323–332. [[CrossRef](#)]
171. Locment, F.; Semail, E.; Kestelyn, X. Vectorial approach-based control of a seven-phase axial flux machine designed for fault operation. *IEEE Trans. Ind. Electron.* **2008**, *55*, 3682–3691. [[CrossRef](#)]
172. Tani, A.; Mengoni, M.; Zarri, L.; Serra, G.; Casadei, D. Control of multiphase induction motors with an odd number of phases under open-circuit phase faults. *IEEE Trans. Power Electron.* **2012**, *27*, 565–577. [[CrossRef](#)]
173. Sui, Y.; Zheng, P.; Yin, Z.; Wang, M.; Wang, C. Open-circuit fault-tolerant control of five-phase PM machine based on reconfiguring maximum round magnetomotive force. *IEEE Trans. Ind. Electron.* **2019**, *66*, 48–59. [[CrossRef](#)]
174. Feng, G.; Lai, C.; Li, W.; Han, Y.; Kar, N.C. Computation-efficient solution to open-phase fault tolerant control of dual three-phase interior PMSMs with maximized torque and minimized ripple. *IEEE Trans. Power Electron.* **2021**, *36*, 4488–4499. [[CrossRef](#)]
175. Chen, Q.; Gu, L.; Lin, Z.; Liu, G. Extension of space-vector-signal-injection-based MTPA control into SVPWM fault-tolerant operation for five-phase IPMSM. *IEEE Trans. Ind. Electron.* **2020**, *67*, 7321–7333. [[CrossRef](#)]
176. Wang, J.B.; Atallah, K.; Howe, D. Optimal torque control of fault-tolerant permanent magnet brushless machines. *IEEE Trans. Magn.* **2003**, *39*, 2962–2964. [[CrossRef](#)]
177. Guo, H.; Xu, J.; Chen, Y. Robust control of fault-tolerant permanent-magnet synchronous motor for aerospace application with guaranteed fault switch process. *IEEE Trans. Ind. Electron.* **2015**, *62*, 7309–7321. [[CrossRef](#)]
178. Shamsi-Nejad, M.; Nahid-Mobarakeh, B.; Pierfederici, S.; Meibody-Tabar, F. Fault tolerant and minimum loss control of double-star synchronous machines under open phase conditions. *IEEE Trans. Ind. Electron.* **2008**, *55*, 1956–1965. [[CrossRef](#)]
179. Wang, W.; Zhang, J.; Cheng, M.; Li, S. Fault-tolerant control of dual three-phase permanent-magnet synchronous machine drives under open-phase faults. *IEEE Trans. Power Electron.* **2017**, *32*, 2052–2063. [[CrossRef](#)]
180. Wang, X.; Wang, Z.; He, M.; Zhou, Q.; Liu, X.; Meng, X. Fault-tolerant control of dual three-phase PMSM drives with minimized copper loss. *IEEE Trans. Power Electron.* **2021**, *36*, 12938–12953. [[CrossRef](#)]
181. Che, H.S.; Duran, M.J.; Levi, E.; Jones, M.; Hew, W.P.; Rahim, N.A. Postfault operation of an asymmetrical six-phase induction machine with single and two isolated neutral points. *IEEE Trans. Power Electron.* **2014**, *29*, 5406–5416. [[CrossRef](#)]
182. Kianinezhad, R.; Nahid-Mobarakeh, B.; Baghli, L.; Betin, F.; Capolino, G.A. Modeling and control of six-phase symmetrical induction machine under fault condition due to open phases. *IEEE Trans. Ind. Electron.* **2008**, *55*, 1966–1977. [[CrossRef](#)]
183. Fnaiech, M.A.; Betin, F.; Capolino, G.A.; Fnaiech, F. Fuzzy logic and sliding-mode controls applied to six-phase induction machine with open phases. *IEEE Trans. Ind. Electron.* **2010**, *57*, 354–364. [[CrossRef](#)]
184. Hu, Y.; Feng, Y.; Li, X. Fault-tolerant hybrid current control of dual three-phase PMSM with one phase open. *IEEE J. Emerg. Sel. Topics Power Electron.* **2021**, in press. [[CrossRef](#)]

185. Hu, Y.; Zhu, Z.Q.; Wu, Z. Modelling and vector control of dual three-phase PMSM with one-phase open. *IET Electr. Power Appl.* **2021**, *15*, 847–860. [[CrossRef](#)]
186. Liu, Z.; Zheng, Z.; Li, Y. Enhancing fault-tolerant ability of a nine-phase induction motor drive system using fuzzy logic current controllers. *IEEE Trans. Energy Convers* **2017**, *32*, 759–769. [[CrossRef](#)]
187. Wang, X.; Wang, Z.; Xu, Z.; Cheng, M.; Wang, W.; Hu, Y. Comprehensive diagnosis and tolerance strategies for electrical faults and sensor faults in dual three-phase PMSM drives. *IEEE Trans. Power Electron.* **2019**, *34*, 6669–6684. [[CrossRef](#)]
188. Wang, Z.; Wang, X.; Cao, J.; Cheng, M.; Hu, Y. Direct torque control of T-NPC inverters-fed double-stator-winding PMSM drives with SVM. *IEEE Trans. Power Electron.* **2018**, *33*, 1541–1553. [[CrossRef](#)]
189. Wang, X.; Wang, Z.; Xu, Z.; He, J.; Zhao, W. Diagnosis and tolerance of common electrical faults in T-type three-level inverters fed dual three-phase PMSM drives. *IEEE Trans. Ind. Electron.* **2020**, *35*, 1753–1769. [[CrossRef](#)]
190. Liu, Y.; Zhu, Z.Q. Influence of gear ratio on the performance of fractional slot concentrated winding permanent magnet machines. *IEEE Trans. Ind. Electron.* **2019**, *66*, 7593–7602. [[CrossRef](#)]
191. Mao, X.; Jain, A.K.; Ayyanar, R. Hybrid interleaved space vector PWM for ripple reduction in modular converters. *IEEE. Trans. Power Electron.* **2011**, *26*, 1954–1967. [[CrossRef](#)]
192. Miyama, Y.; Hazeyama, M.; Hanioka, S.; Watanabe, N.; Daikoku, A.; Inoue, M. PWM carrier harmonic iron loss reduction technique of permanent-magnet motors for electric vehicles. *IEEE Trans. Ind. Appl.* **2016**, *52*, 2865–2871. [[CrossRef](#)]
193. Miyama, Y.; Ishizuka, M.; Kometani, H.; Akatsu, K. Vibration reduction by applying carrier phase-shift PWM on dual three-phase winding permanent magnet synchronous motor. *IEEE Trans. Ind. Appl.* **2018**, *54*, 5998–6004. [[CrossRef](#)]
194. Han, X.; Jiang, D.; Zou, T.; Qu, R.; Yang, K. Two-segment three-phase PMSM drive with carrier phase-shift PWM for torque ripple and vibration reduction. *IEEE. Trans. Power Electron.* **2019**, *34*, 588–599. [[CrossRef](#)]
195. Huang, Y.; Xu, Y.; Zhang, W.; Zou, J. PWM frequency noise cancellation in two-segment three-phase motor using parallel interleaved inverters. *IEEE. Trans. Power Electron.* **2019**, *34*, 2515–2525. [[CrossRef](#)]
196. Zhang, W.; Xu, Y.; Huang, H.; Zou, J. Vibration reduction for dual-branch three-phase permanent magnet synchronous motor with carrier phase-shift technique. *IEEE. Trans. Power Electron.* **2020**, *35*, 607–618. [[CrossRef](#)]
197. Ji, Z.; Cheng, S.; Lv, Y.; Wang, D.; Sun, W.; Li, X. The mechanism for suppressing high-frequency vibration of multiphase surface permanent magnet motors via PWM carrier phase shifting. *IEEE. Trans. Power Electron.* **2021**, in press. [[CrossRef](#)]
198. Wang, X.; Yan, H.; Sala, G.; Buticchi, G.; Gu, C.; Zhao, W.; Xu, L.; Zhang, H. Selective torque harmonic elimination for dual three-phase PMSMs based on PWM carrier phase shift. *IEEE. Trans. Power Electron.* **2020**, *35*, 13255–13269. [[CrossRef](#)]
199. Capella, G.J.; Pou, J.; Ceballos, S.; Konstantinou, G.; Zaragoza, J.; Agelidis, V.G. Enhanced phase-shifted PWM carrier disposition for interleaved voltage-source inverters. *IEEE. Trans. Power Electron.* **2015**, *30*, 1121–1125. [[CrossRef](#)]
200. Wang, X.; Sala, G.; Zhang, H.; Gu, C.; Buticchi, G.; Formentini, A.; Gerada, C.; Wheeler, P. Torque ripple reduction in sectorized multi three-phase machines based on PWM carrier phase shift. *IEEE Trans. Ind. Electron.* **2020**, *67*, 4315–4325. [[CrossRef](#)]
201. Reddy, B.P.; Keerthipati, S. Torque ripple minimization of PPMIM drives with phase-shifted carrier PWM. In Proceedings of the IECON 44th Annual Conference of the IEEE Industrial Electronics Society, Washington, DC, USA; 2018; pp. 725–730.